



저작자표시-비영리-변경금지 2.0 대한민국

이용자는 아래의 조건을 따르는 경우에 한하여 자유롭게

- 이 저작물을 복제, 배포, 전송, 전시, 공연 및 방송할 수 있습니다.

다음과 같은 조건을 따라야 합니다:



저작자표시. 귀하는 원저작자를 표시하여야 합니다.



비영리. 귀하는 이 저작물을 영리 목적으로 이용할 수 없습니다.



변경금지. 귀하는 이 저작물을 개작, 변형 또는 가공할 수 없습니다.

- 귀하는, 이 저작물의 재이용이나 배포의 경우, 이 저작물에 적용된 이용허락조건을 명확하게 나타내어야 합니다.
- 저작권자로부터 별도의 허가를 받으면 이러한 조건들은 적용되지 않습니다.

저작권법에 따른 이용자의 권리는 위의 내용에 의하여 영향을 받지 않습니다.

이것은 [이용허락규약\(Legal Code\)](#)을 이해하기 쉽게 요약한 것입니다.

[Disclaimer](#)

Dissertation for the Degree of Doctor of Philosophy

**Numerical study on performance analysis of a variable
camber hydrofoil used in a flapping tidal stream turbine**

Nguyen Le Dang Hai

Faculty of Applied Energy System

Major of Mechanical Engineering

GRADUATE SCHOOL

JEJU NATIONAL UNIVERSITY

February 2022

Numerical study on performance analysis of a variable camber hydrofoil used in a flapping tidal stream turbine

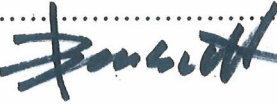
Nguyen Le Dang Hai
(Supervised by Professor Jin Hwan Ko)

A dissertation submitted in partial fulfillment of the requirements for
the degree of Doctor's in Mechanical Engineering

2022 02

The dissertation has been examined and approved.

.....
Prof. Bum-Suk Kim
Dissertation Director



.....
Faculty of Wind Energy Engineering
Jeju National University

.....
Prof. Ji Hyun Jeong
Dissertation Committee Member



.....
Faculty of Applied Energy System,
Jeju National University

.....
Prof. Jin Hwan Ko
Dissertation Committee Member & Supervisor



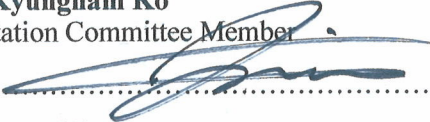
.....
Faculty of Applied Energy System,
Jeju National University

.....
Prof. Kyungnam Ko
Dissertation Committee Member



.....
Faculty of Wind Energy Engineering
Jeju National University

.....
Dr. Jihoon Kim
Dissertation Committee Member



.....
Korea Institute of Ocean Science and
Technology.

.....
2021.12.16

Date

Major of Mechanical Engineering
Faculty of Applied Energy System
GRADUATE SCHOOL
JEJU NATIONAL UNIVERSITY

Acknowledgements

Firstly, I would like to express my deepest gratitude to my advisor Professor Jin Hwan Ko, Professor of Mechanical Engineering, Jeju National University, for his enthusiastic guidance and constantly support in conducting my research on the way to pursue a Ph.D. in Mechanical Engineering. I will always remember Professor as the one advisor in my life who influenced me more than anyone. Besides that, I would like to send thankful to co-advisor Dr. Le Quang Tuyen for his remote CFD-related instruction as well as Hendra Adi Putra for his response. Moreover, I would like to thank all members of dissertation evaluation committee for their suggestions and comments during the thesis defense. My sincere appreciation also goes to Assoc. Prof. Le Hieu Giang for vision of the future.

Secondly, I appreciate the help and encouragement from all the members of Multidisciplinary and Interdisciplinary Mechanical Design (MIMD) lab: Dasom Jeong, Donggeon Kim, Euncheol Im and Hyun Min Shim.

Thirdly, I am indebted to my beloved wife La Thi Cam Tu along with two adorable daughters Nguyen Ngoc Nhu and Nguyen Ngoc Han. Their childhood memories have past day by day without dad's love. Needless to say, I am hugely grateful to my parents Nguyen Van Rach and Le Thi Nhan as well as my parents-in-law La Tan Phung and Nguyen Thi Banh. Without them, it was tough to chase my dream.

Finally, I would like to thank the scholarships from Brain Korea 21 (BK 21) and all the sponsors of the projects. Beside that, I would like to send thank to Dr. Truong Quang Tri, Dr. Nguyen Tri Nguyen, Dr. Phan Cong Binh, Dr. Do Van Hien and others whom helped or gave precious advices since the first day I had intention to study abroad.

Dissemination

Journal Publications

1. **Nguyen Le Dang Hai**, Hoon Cheol Park, Jin Hwan Ko. Dynamic response estimation for a variable camber NACA0012 hydrofoil of a flapping-type tidal stream turbine, *Journal of Marine Science and Technology* Volume 26, Issue 1, March 2021.
2. Jaebum Kim, O Soon Kwon, **Nguyen Le Dang Hai** and Jin Hwan Ko. Study on the Design of an Underwater Chain Trencher via a Genetic Algorithm, *Journal of Marine Science and Engineering* Volume 7, Issue 12, December 2019.

Conference Publications

1. **Nguyen Le Dang Hai**, Jaebum Kim, O Soon Kwon and Jin Hwan Ko. Study on the Design of Underwater Chain Trencher, 2019 Spring Conference on Drive and Control, KSFC, June 2019.
2. Jin Hwan Ko, **Nguyen Le Dang Hai**, and Jihoon Kim. Introduction of Studies on a Flapping Hydrofoil Tidal Stream Turbine in Korea, November 2019.
3. **Hai Nguyen Le Dang**, Jin Hwan Ko, Dasom Jeoung. Numerical study on Performance Analysis of a Variable Camber Hydrofoil used in a Flapping hydrofoil turbine, AFORE-014, November 2021.

Table of Contents

Acknowledgements	i
Dissemination.....	ii
Table of Contents	iii
List of Figures	v
List of Tables	viii
Nomenclature	ix
Abstract (Hangul).....	xi
Chapter 1 Introduction	1
1.1 Overview of tidal stream turbine	1
1.2 Overview of flapping hydrofoil turbine (FHT).....	3
1.3 Previous researches on performance analysis.....	7
1.4 Morphology of hydrofoil used in FHT	9
1.5 Scope and outline of this dissertation	13
Chapter 2 Flapping tidal stream turbine	15
2.1 Three features inspired by a marine creature	15
2.2 Sub conclusion.....	22
Chapter 3 Response and power analysis	23
3.1 Variable camber mechanism.....	23
3.2 Hydrodynamics prediction of a cambered hydrofoil	27
3.2.1 XFOIL as predicting tool	27
3.2.2 Hydrodynamics of cambered hydrofoil.....	32
3.3 Dynamic model as an estimating tool.....	35
3.3.1 Dynamic model validation	37
3.4 Response analysis	38
3.4.1 Response of scenario 1	39
3.4.2 Response of scenario 2.....	42
3.5 Power analysis	43
3.5.1 Power of scenario 1	43
3.5.2 Power of scenario 2.....	53
3.6 Sub conclusion.....	60
Chapter 4 Parametric study on power performance	62

4.1 Computational Fluid Dynamics tool.....	62
4.1.1 Validation of the in-house code	66
4.2 Performance analysis	70
4.2.1 Kinematics of right-swing configuration	70
4.2.2 Forces and flow characteristics	71
4.3 Parametric analysis	75
4.3.1 Isocontour map of camber variation for first half of a cycle, $t/T = 0 \sim 0.5$	81
4.3.2 Isocontour map of camber variation for second half of a cycle, $t/T = 0.5 \sim 1$	83
4.3.3 Isocontour map of camber variation for full cycle, $t/T = 0 \sim 1$	85
4.4 Sub conclusion.....	86
Chapter 5 Conclusion and further work	88
5.1 Conclusion	88
5.2 Further work	89
References.....	91

List of Figures

Figure 1 Common tidal stream turbines [5]	2
Figure 2 Working range of FHT (left) and Rotary type (right).....	3
Figure 3 McKinney and DeLaurier's wingmill experiment model [7].....	4
Figure 4 Trajectory of Left-swing, Plunge-pitch, Right-swing configurations (From left to right)	4
Figure 5 Stingray in preparation [15].....	6
Figure 6 Brown University's 2 kW [16].....	6
Figure 7 Common Cross section hydrofoil of FHT	9
Figure 8 NACA00XX series	10
Figure 9 Profile of NACA0015 and NACA0012 hydrofoil	10
Figure 10 Device in Liu et al. [59].....	11
Figure 11 Flexible flapping hydrofoil from Tuyen et al. [34].....	12
Figure 12 Outline of this dissertation.....	14
Figure 13 Scallop (left) [63] and numerical work of scalloped mimicked FHT (right) [33]	15
Figure 14 Manta Rays (left) [64] and experimental work of Manta-Ray mimicked FHT (right) [41].....	16
Figure 15 Sea turtle [65, 66].....	16
Figure 16 Swimming Trajectory of Sea turtle [67]	17
Figure 17 The operating regimes of a flapping foil, as well as the corresponding angle of attack and force directions throughout the flapping cycle [68].....	18
Figure 18 Artificial turtle model with four legs	19
Figure 19 Power transmission of the artificial turtle model.....	19
Figure 20 Bones and kinematics in a sea turtle flipper [69].....	20
Figure 21 Turtle forelimb with camber shape [72] and camber definition [67].....	21
Figure 22 Bilateral Symmetry [73] of a sea turtle.....	22
Figure 23 Camber-making mechanism inside NACA0012 hydrofoil [75]	24
Figure 24 Angle relation of variable camber hydrofoil.....	25
Figure 25 Flapping motion with a variable camber hydrofoil during pitch variation in one period	26
Figure 26 C_p and streamline plot of camber hydrofoil at $Re = 80,000$, $N_{cr} = 9$ in XFOIL [39].	28
Figure 27 Lift coefficients of NACA0012 [39] at $Re = 4 \times 10^4$ and $Re = 10^5$	29
Figure 28 Drag coefficients of NACA0012 [39] at $Re = 4 \times 10^4$ and $Re = 10^5$	29
Figure 29 Comparison of the lift coefficients for NACA0012 [39] at $Re = 8 \times 10^4$	30

Figure 30 Comparison of the drag coefficients for NACA0012 [39] at $Re = 8 \times 10^4$	31
Figure 31 Lift coefficients of NACA0012 [39] at $Re = 16 \times 10^4$	31
Figure 32 Drag coefficients of NACA0012 [39] at $Re = 16 \times 10^4$	32
Figure 33 Lift coefficients versus AoA at $Re = 80,000$	32
Figure 34 Lift coefficients for a cambered hydrofoil [39] at $Re = 80,000$	33
Figure 35 Drag coefficients for a cambered hydrofoil [39] at $Re = 80,000$	33
Figure 36 Lift coefficients for a cambered hydrofoil [39] at $Re = 160,000$	34
Figure 37 Drag coefficients for a cambered hydrofoil [39] at $Re = 160,000$	35
Figure 38 Free - body diagram of turbine [38].....	36
Figure 39 Effective AoA of a variable camber hydrofoil for the A1, A2, B1 and B2 cases. 39	
Figure 40 Responses of scenario 1 [39]	41
Figure 41 Responses of scenario 2.....	42
Figure 42 The wing span b and the vertical height d of the hydrofoil	43
Figure 43 Moment at the flap 1 and flap 2.....	45
Figure 44 Pitching moment of symmetric and variable camber hydrofoils	46
Figure 45 Input power of symmetric and variable camber hydrofoils	47
Figure 46 Hydrodynamic moment of symmetric and variable camber ones.....	49
Figure 47 Flapping speed of symmetric and variable camber hydrofoils.	50
Figure 48 Hydrodynamic power values of (a) symmetric and (b) variable camber hydrofoils. The table (c) contains the average hydrodynamic power values.....	51
Figure 49 Extracted power values of the (a) symmetric and (b) variable camber ones; the table (c) contains the corresponding average values.....	52
Figure 50 Pitching moment of symmetric and variable camber hydrofoil.....	54
Figure 51 Input power values of the (a) symmetric and (b) variable camber hydrofoils	55
Figure 52 Hydrodynamic moment of the (a) symmetric and (b) variable camber hydrofoils	57
Figure 53 Flapping speed of the (a) symmetric and (b) variable camber hydrofoils	57
Figure 54 Hydrodynamic power values of the (a) symmetric and (b) variable camber hydrofoils; the table (c) contains the corresponding average values.....	58
Figure 55 Extracted power values of the symmetric and variable camber hydrofoils; the table (c) contains the corresponding average values.....	59
Figure 56 CFD process.....	62
Figure 57 Chimera mesh with symmetric NACA0012 by 463×105	64
Figure 58 Profiles of symmetric (camber 0%), camber 21% (Top right) and camber 39% (Bottom right)	65

Figure 59 Heave motion amplitude $H_0 = c = 0.24$ m, Pitch amplitude $\theta = 75^\circ$ of NACA0015, $f^* = 0.15$ at Reynolds number 500,000.	66
Figure 60 Graph of Lift, Drag force for full 5 cycles reduced frequency $f^* = 0.14$, pitch angle $\theta = 75^\circ$ (Left) Comparison Lift, drag 5 th cycle with Kinsey data (Right)	67
Figure 61 NACA0015 with $H_0/c = 1.5$, maximum pitch angle $\theta = 85^\circ$, $f^* = 0.16$ at Reynolds number 500,000.	68
Figure 62 Benchmark Kinsey (Top) Coefficient comparison: Instantaneous vertical force C_y , normalized heaving velocity V_y , pitching contribution to the power C_{pq} , and total power coefficient C_p (Bottom) flow pattern comparison (vorticity fields at $t/T \frac{1}{4} 0.25$ and 0.45 (blue: CW vorticity, red: CCW vorticity)	69
Figure 63 NACA0012 Trajectory x_p (centerline) of right swing configuration.	70
Figure 64 C_L curves and Velocity of camber 0%, camber 21% and camber 39%.	72
Figure 65 C_D curves and velocity of camber 0%, camber 21% and camber 39%	72
Figure 66 C_M curves and velocity of camber 0%, camber 21% and camber 39%	72
Figure 67 Pressure contour of ($f^* = 0.1$, $\theta = 60^\circ$) at $t/T = 0.0, 0.2, 0.4, 0.6$ and 0.8	74
Figure 68 Vortex contour of ($f^* = 0.1$, $\theta = 60^\circ$) at $t/T = 0.0, 0.2, 0.4, 0.6$ and 0.8 (blue: clockwise vortex; red: counterclockwise vortex).....	75
Figure 69 Power graphs of ($f^* = 0.1$, $\theta = 60^\circ$)	80
Figure 70 Power efficiency maps of camber 0%, camber 21% and camber 39% for first half of cycle.....	81
Figure 71 Power efficiency maps of camber 0%, camber 21%, and camber 39% for second half of a cycle.....	83
Figure 72 Power efficiency maps of camber 0%, camber 21% and camber 39% for full cycle	85

List of Tables

Table 1 Technical Specifications of Hydrofoil and Flapping Arm [75].....	24
Table 2 Positive Deflection Angles and Camber as the result of the Pitch angle [75].....	26
Table 3 Measured Responses of the Prototype with Symmetric Hydrofoil [38].....	37
Table 4 Available Power Values for the Symmetric and Cambered Hydrofoils.....	44
Table 5 Total Negative Areas and the Corresponding Average Input Power Values (Actual time in the period is used in computing the area; T of A2 is 4.329 sec. and T of B2 is 2.5 sec.)	48
Table 6 System efficiency rates.....	53
Table 7 Available Power Values for the Symmetric and Cambered Hydrofoils.....	54
Table 8 Total Negative Areas and the Corresponding Average Input Power Values	56
Table 9 System efficiency rates.....	60
Table 10 Parameter for 16 cases of parametric study.....	77
Table 11 Key point in a cycle.....	86

Nomenclature

c	Chord length of the hydrofoil, m.
b	Span of the hydrofoil, m.
x_p	Pitching axis location from the leading edge, c
ψ	Flapping angle, °
$\dot{\psi}$	Angular speed of the flapping arm, rad·s ⁻¹
$\ddot{\psi}$	Angular acceleration of the flapping arm, rad·s ⁻¹
θ	Pitch angle, °
h	Camber height, m.
l	Flapping arm length, m
m	Mass of flapping arm and or hydrofoil, kg
W	Relative flow velocity, m·s ⁻¹
V_∞	Far field inflow velocity, m·s ⁻¹
I	Mass moment of inertia of the hydrofoil including flapping arm around the flapping axis, kg·m ²
I_g	Equivalent mass moment of inertia of the gearbox about the driving gear axis, kg·m ²
γ	Deflection angle of the flow, °
ρ	Density of water, kg·m ⁻³
C_L	Lift coefficient of the hydrofoil
L	Lift force

C_D	Drag coefficient of the hydrofoil
D	Drag force
C_M	Moment coefficient of the hydrofoil
$M_{c/4}$	Pitching moment at pitch axis, N·m
V_f	Induced or deflected flow velocity, $m \cdot s^{-1}$
S	Projected surface area of the hydrofoil m^2
C	Damping coefficient of the transmission system, $N \cdot m \cdot s$
τ	Measure holding torque, N·m
Re	Reynolds number
f	Frequency
f^*	Reduced frequency
M_{f_1}	Moment at flap pivot 1
M_{f_2}	Moment at flap pivot 2
sec	Second

Abstract (Hangul)

이번 연구에서는 유체의 운동에너지를 활용하기 위해 거북이를 모방한 플래핑 수중익 터빈의 개념 설계를 소개합니다. 상세설계 단계 전에 가변 캠버를 사용하여 단일 플래핑 터빈 시뮬레이션을 진행했습니다. 시뮬레이션에서 가변 캠버 수중익은 복잡성이 약간 증가함에도 불구하고 플래핑 수중익 터빈의 출력 성능을 향상시키는 우수한 결과를 보여줍니다. 자체 개발된 전산 유체역학 프로그램을 활용한 실제 발전에 근접한 조건 하의 매개변수 연구에서는, 수중익의 캠버가 증가하여도 고정 캠버의 경우 효율이 증가하지 않는 경향이 있음을 보여줍니다. 따라서 가변 캠버는 플래핑 수중익 터빈의 효율 향상 측면에서 꼭 필요한 방법임을 확인할 수 있었습니다.

Chapter 1 Introduction

1.1 Overview of tidal stream turbine

Nowadays, climate change causes wide spread damage around the world. Hence, renewable energy raises a huge interesting in research effort in the recent years. Renewable energy, often known as eco-clean energy, is derived from natural sources or processes that are renewed on a regular basis. The Sun and wind, for instance, continue to shine and blow despite the fact that their availability is dependent on time and weather [1]. Renewable energy goals are part of government-mandated programs that force electricity retailers to source particular proportions of total electricity sales from renewable energy sources over a set period. The goal of these programs is to encourage renewable energy while also reducing reliance on fossil fuels [2]. Currently, usage of energy from river and ocean streams is considerably increasing. The energy capability of water streams is much greater than humanity needs, even in the far future [3].

Numerous technologies have been employed for harnessing electricity from tidal streams, and these can generally be categorized as some principal types: horizontal axis turbines (HAT) in subfigure (1), vertical axis turbine (VAT) in subfigure (2), Venturi effect devices in subfigure (3), tidal kites in subfigure (4) and flapping hydrofoil turbine (FHT) in subfigure (5) [4] in **Fig. 1**. HAT, VAT and Venturi effect devices utilize kinetics of the flow to turn the twisted blades. In contrast, FHT moves the hydrofoil up and down. Compare to HAT, which has the similar axis position, Venturi effect devices with duct could increase the water velocity pass through and decrease the pressure to drive the turbine [4]. Special type, a tidal kite turbine is an underwater kite device that uses the tidal stream to convert tidal energy into electricity. The water stream provides a hydrodynamic lift force on a kite's wing, propelling it forward [4].

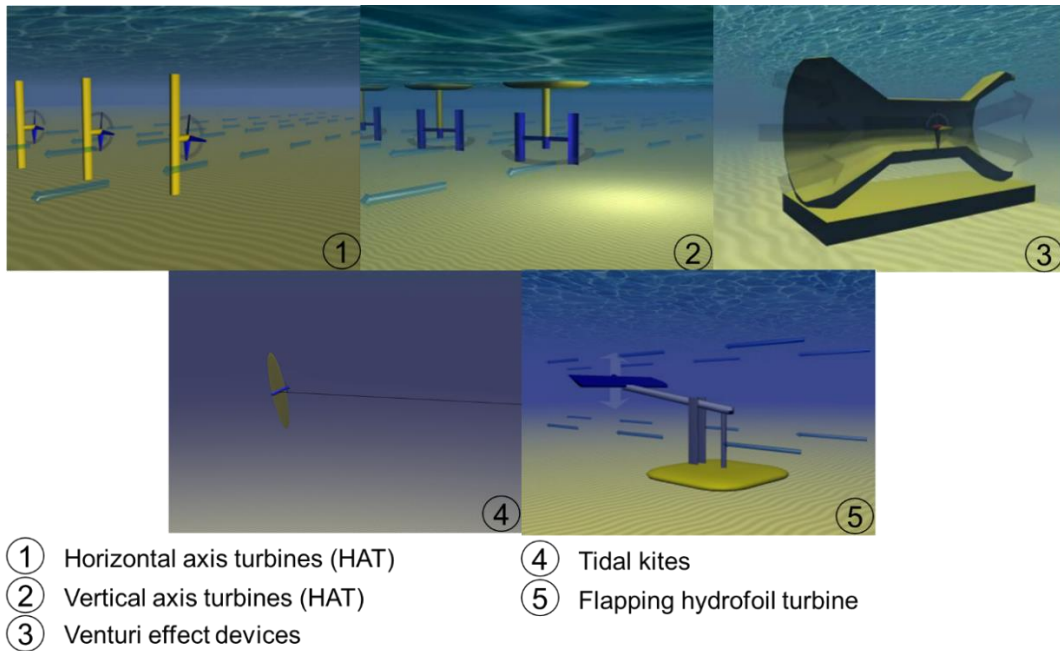


Figure 1 Common tidal stream turbines [5]

The regular rotary-type turbines base on the incoming flow of water remaining smoothly attached to the wings for high efficiency. In contrast, the flapping ones utilize oscillating rectangular lifting surfaces. There is no doubt that these kind of turbines could perform in shallow water due to its rectangular extraction plane. In order to obtain more power extraction, the technical issue could be solved simply via extending the span of the hydrofoil **Fig. 2** (left). In contrast, rotary turbine needs a deeper place due to extending the radius of its blades **Fig. 2** (right). In addition, fabricating the twisted hydrofoils of rotary type demands the advance technology [4]. Furthermore, the flapping hydrofoil turbine has advantage of free noise pollution. Besides that, these turbines could minimize the threat to the habitats of water creatures due to relatively low tip speed as compared to rotary turbines [6].

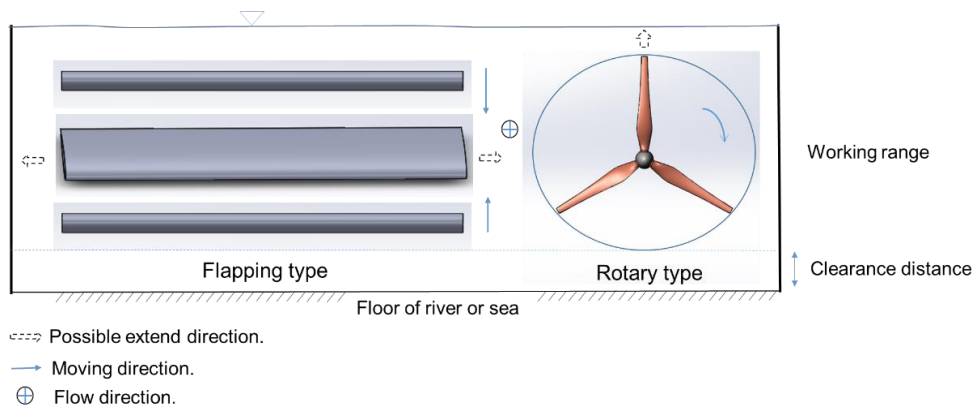


Figure 2 Working range of FHT (left) and Rotary type (right)

Aforementioned, the benefits of the flapping hydrofoil turbine has really drawn a great our interest among the common tidal turbines. Next section will focus on the flapping hydrofoil turbine.

1.2 Overview of flapping hydrofoil turbine (FHT)

To the best knowledge, known as the first report about the novel turbine for wind power, McKinney and DeLaurier made an effort to develop the oscillating-foil turbines named as “Wingmill” [7] in **Fig. 3** to extract wind energy. The phase between vertical translation and pitching was prescribed. The design could be feasible for harnessing energy from the running water. In the last year of twenty century, Jones et al. [8] investigated an oscillating-wing generator of wingmill by numerical schemes via a panel code as well as experimental approach. The result of this study predicted higher efficiency than the study of McKinney and DeLaurier.

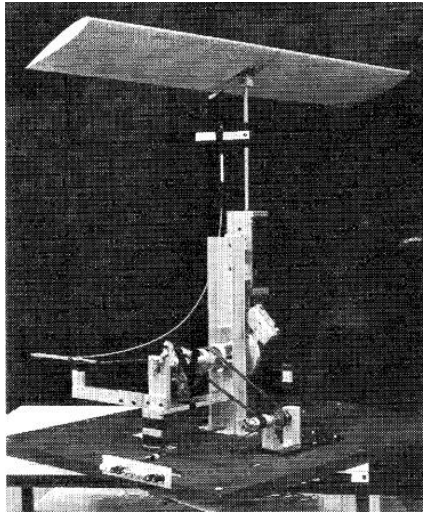


Figure 3 McKinney and DeLaurier's wingmill experiment model [7]

Currently, several different configurations are applicable for a flapping hydrofoil turbine such as the plunge-pitch, right-swing and left-swing types attached with various hydrofoils. The difference in their trajectories are described in **Fig. 4**. For plunge – pitch type, these motions could be sinusoidal, non-sinusoidal or mixture of both [9]. The proportional statistics [10] show that the studies about the flapping, purely pitch and purely heave contribute about 55%, 28% and 19%, respectively. The hydrofoil motion could generate electric power due to the lift and moment created by the incoming flow either side of the wing [4].

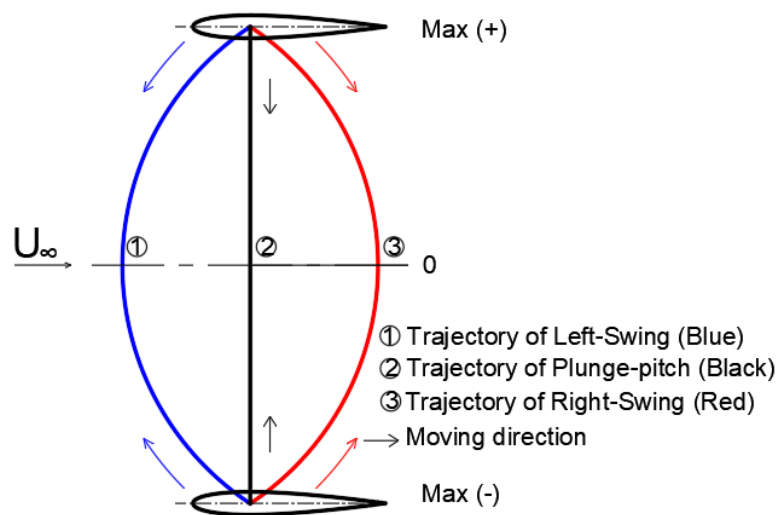


Figure 4 Trajectory of Left-swing, Plunge-pitch, Right-swing configurations (From left to right)

The studies followed McKinney and DeLaurier came in various levels such as lab-scale prototype with single, tandem, and multiple foils. Multi-level and multi-phase researches for the specific flapping hydrofoil turbines have been carried out. HAO research project tested a 2 kW turbine prototype with a tandem configuration [11]; in the field test, the turbine is mounted on the pontoon boat. When the overall losses in the mechanical system are taken into consideration, the results show optimal performance at reduced frequency of about 0.11, at which condition the measured power extraction efficiency exceeds 40%. This first prototype's hydrodynamic efficiency exceeds expectations with 40% and is likewise to the highest results achieved with current rotor blade turbines. Another experiment in the tandem configuration was conducted by Xu et al. [12] in circulation water tunnel. According to experimental data, the highest hydrodynamic efficiency of single hydrofoil is 25.2% at Strouhal number of 0.235. Sitorus et al. [13] designed a lab-scale flapping-type turbine and tested in the facility at the Korea Institute of Ocean Science and Technology (KIOST). Also, the non-linear dynamic model was validated by a series of experiments along with computational fluid dynamics (CFD) simulations. Inspired by the dolphin, Kim et al. [14] tested a mirror-type dual configuration prototype in the towing tank facility in Korea. A high load and a high input arm angle were found to be advantageous while varying factors through a parametric analysis. Furthermore, in terms of power extraction, the optimal reduced frequency was discovered to be 0.125.

As a pre-commercial level, an international-known multi-phase project named Stingray by The Engineering Business Ltd [15] was launched with the mission designing and building 150 kW generator and testing in real tidal stream. The model withheld the single arm by the rigid system and fixed in the seabed. Project "Marine Hydrokinetic Energy Harvesting Using Cyber-Physical system" [16] owns two generators, each has tandem hydrofoils put in a low cost tugboat. The tandem foils were able to attain the 2 kW design power rating.

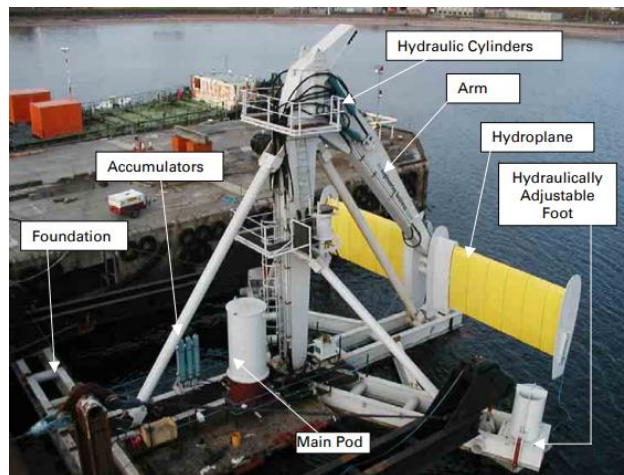


Figure 5 Stingray in preparation [15]

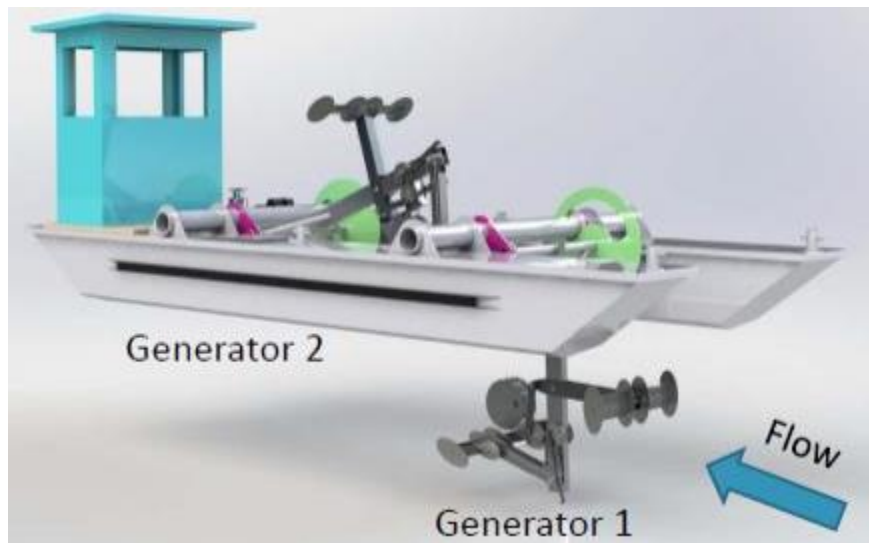


Figure 6 Brown University's 2 kW [16]

According to classification based on the degree of freedom (DOF), there are several types such as fully passive, semi-passive and fully constrained motions. A flapping hydrofoil turbine with the motion undergone by the hydrofoil can be categorized with five principle motion parameters, the trajectory and the amplitude of the plunge, the motion shape and the amplitude in pitch, the heaving frequency, the pitching frequency and the phase between the plunge and the pitch motion. Each of the motion can be free or can be constrained depending on the specific design of the turbine. Thus, if all the motion parameters are constrained, we

called a fully-constrained turbine [17]. Aforementioned lab-scale prototype [13] used semi-passive activation mode. The hydrodynamic forces act on the hydrofoil with prescribed pitching motion drove the flapping arm. More recently, Duarte et al. [18] designed and tested a reduced scale prototype of fully passive flapping foil turbine in channel with Reynolds number 60,000. The results show that when the pitching axis is located at one thirds of the chord length, turbine achieved the best performance.

1.3 Previous researches on performance analysis

The influences of the kinematic parameters on the power extraction performance have been studied for many years. There are mainly 4 parameters: Reynolds number, reduced frequency, amplitude of pitch or heave, and three dimensional effect [10].

The first one, Reynolds number (Re), which determines the flow state, has been investigated in a wide range of values for the flapping foil, ranging from 10^2 to 10^7 . One research from Ashraf et al. [19] found that the increment of Re lead to increase of both thrust coefficient and propulsive with Re number from 20 to 200,000. Zhu [20] found that the increment of Reynolds number could enhance energy harvesting efficiency.

Flow structure changes apparently when the reduced frequency as the second one varies. In the analysis of flapping foil propulsion and power extraction, the reduced frequency is a critical parameter. The amount of energy that the flapping foil can extract from the free stream is determined by the reduce frequency [10]. When other parameters are fixed, propulsive efficiency grows monotonically with reduced frequency at first, then gradually falls with its higher values [21, 22]. Wu et al. [23] claim that energy extraction efficiency monotonically drops with the reduced frequency increased.

The overall effects of the amplitude of pitching or heaving on the flow structures are similar with those of the reduced frequency [10]. The experimental method [24] was used to investigate the transitions in the wake of a pitching foil with different amplitude and frequency

combination and obtained aforementioned transition process of the flow structure. The impact of pitching and heaving amplitudes on power extraction performance is sophisticated, and no general rule so far [10]. Jone [25] claimed that the angle of attack induced by heaving motion must be smaller than the pitch angle in order to reach the power extraction state.

The shape at the hydrofoil ends significantly affect the hydrodynamic characteristics of an oscillating foil related to the three dimensional effect as the last parameter.

Researchers have employed numerous tool for numerical and experimental approaches. Numerical research for the flapping system could be mainly conducted with Computation Fluid Dynamics (CFD) by using commercial software such as Ansys Fluent [26, 27, 28, 29], Ansys CFX [30], STAR-CCM+ [17]; free software such as OpenFOAM [31, 32] and in-house code such as Kflow [33, 34, 35]. Although there are differences among software, most of CFD software likely share the similar govern equations such as Navier-stoke equations.

CFD is a common use tool for research related to fluid. Chimera method [36, 37] has been develop for moving body problems. However, simulations with CFD consume huge time especially with 3D simulations. In addition, some CFD are really pricey, and not available. Moreover, some require run in Linux operation system. Another numerical approach utilized Matlab to deal with the problem instead of using these CFD software listed above, named as Non CFD method. Tri et al. [38] recently introduced dynamic model to forecast the explicit response of a symmetric hydrofoil flapping harvester. As consecutive research of it, Hai et al. [39] utilized the nonlinear model to anticipate the dynamic response of two-flap camber hydrofoil in the flapping turbine.

As a costly way by using advanced facilities along with pricey measurement tools but reality, groups of researcher in wealthy country have adopted experiment approaches in their study. The scale of experiment could be varied upon water channel [38, 40], towing tank [14], in-situ experiment [41] and test sites [11]. Besides that, visualization & velocity measurement

tools are particle image velocimetry (PIV) [42, 43, 44], digital particle image velocimetry (DPIV) [45, 46] and dye flow visualization [47].

1.4 Morphology of hydrofoil used in FHT

FHTs share the same profile with the wind turbine. Most of studies used common standard symmetric hydrofoil in their research [17, 31]. Some researchers are interested in the geometric parameter of the hydrofoil such as flat plate, ellipse. These parameters comprise of the boundary of the hydrofoil, the chord length c , span length. The cross section of hydrofoil comes in many shapes such as NACA00XX series airfoil, rectangular [48], and ellipse [45] in **Fig. 7**. About NACA airfoil, symmetric NACA four digits series in **Fig. 8** have become the favorite choice such as NACA0012, NACA0015 [49], NACA0018 [50] and NACA0020 [51]. These airfoil databases could be obtained in [52]. Another type of used hydrofoil is SD7003 [53].

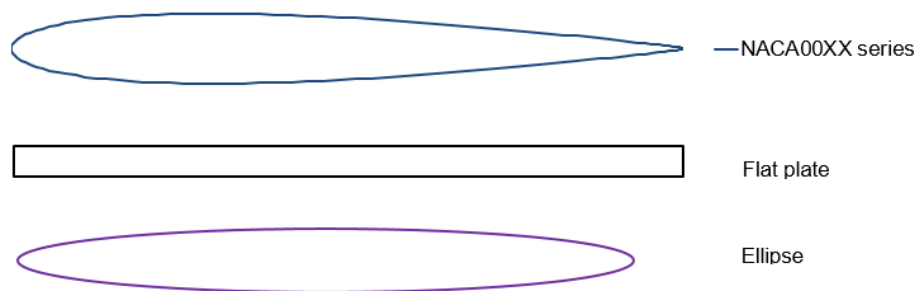


Figure 7 Common Cross section hydrofoil of FHT

National Advisory Committee for Aerodynamics

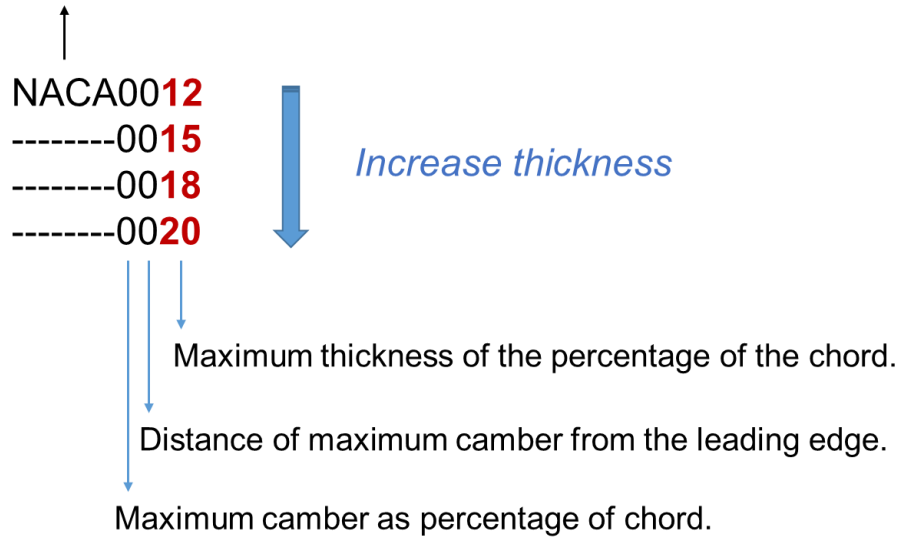


Figure 8 NACA00XX series

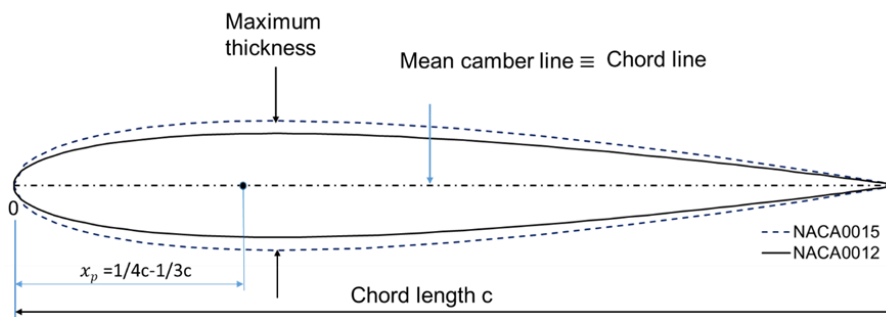


Figure 9 Profile of NACA0015 and NACA0012 hydrofoil

As shown in **Fig. 9**, NACA0012 has smaller maximum thickness compare to NACA0015. Thus, it owns a slender shape and less resistance.

Some studies have been conducted in order to examine the impact of foil thickness on the power generation efficiency [6]. Lindsey [54] used a panel method to show that the foil thickness had an effect if the flow stayed linked to the airfoil. A thinner foil is known to improve the performance.

As the modification of the symmetric hydrofoil, some researches use symmetric hydrofoil attached with flat plate or flexible flat plate [55]. Liu et al. [56] used NACA0015

and a tail hinged using a torsion spring. The results of their study show that a flapping foil generator can improve the efficiency by using a flexible tail with appropriate natural frequency in the optimal range of reduced frequency f^* between 0.12 and 0.18. Kumar [57] used a NACA0015 hydrofoil attached to an elastic plate in order to estimate the thrust forces generated by the flapping foil.

The most complexed hydrofoil was introduced is the flexible hydrofoil. The concept “flexible” here means the shape of airfoil smoothly deformed along with time. In order to examine the impacts of flexible deformation on aerodynamic performance, flexible deformation is formulated span-wise and chord-wise independently [58]. Therefore, these specific airfoils require a system of mechanisms inside the airfoil to control the airfoil shape. Moreover, additional power is an inevitable on demand. By boosting the peaks of lift force during a flapping cycle and regulating the phase shift between force and velocity to a favorable trend, the flexible structure of a wing can improve power efficiency. Furthermore, wing flexibility has a greater impact on efficiency at a low nominal effective angle of attack (AoA) [59]. The study deformed the airfoil from the leading to the trailing edge.

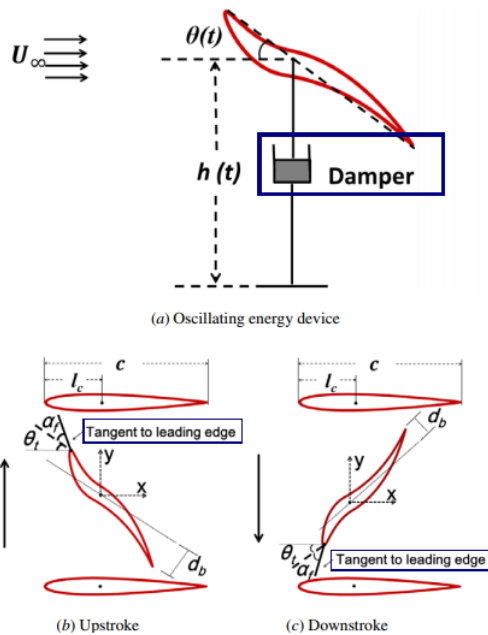


Figure 10 Device in Liu et al. [59]

Authors evaluated the flapping wing's aerodynamic performance with various chord flexures [60]. In 2015, the numerical investigation about the effect of hydrofoil flexibility on the power extraction in 2D and 3D carried out by Tuyen et al. [34] in **Fig. 11** shown that the chord-wise flexibility plays an important role in the improvement of 30% and 50% power extraction with 20% chord-wise flexure under 2D and 3D simulation, respectively. The airfoil only deformed the rear near the trailing edge.

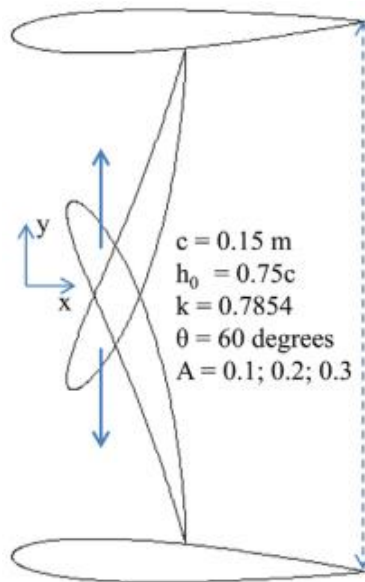


Figure 11 Flexible flapping hydrofoil from Tuyen et al. [34]

A few previous researches studied the effect of camber on flapping foil such as Hoke et al. simulated in fully laminar, with a Reynolds number 1,100 for power extraction cases [61]. The airfoil shape is formed by deforming the camber line via a circular arc centered at the mid-span, with the magnitude of the circular arc deformation sinusoidal during time variation. The results showed that the efficiency of the systems can be increased by deforming the airfoil shape. Ashraf et al. [62] studied the effect of Reynolds number, thickness and camber on flapping airfoil propulsion. Recently, a review paper [10] showed that the research about 2D symmetric foil take an account nearly 70% and that about 2D flexible foil is only approximately 10%.

1.5 Scope and outline of this dissertation

The outline of this thesis is as follow:

Chapter 1: Overview about previous studies and outline of this thesis.

Chapter 2: Targeted creature in this study, sea turtle is expected to swim by simultaneous four legs locomotion. The conceptual design mimicking a turtle has four equal legs, right swing configuration and works as flapping hydrofoil turbine. As the concept stage, the hydrofoil used have considered carefully. Almost studies have focused on the performance analysis of symmetric hydrofoil [6, 10]. There are still unveiled many things about the performance of the camber hydrofoil.

Chapter 3: Variable foot shape, kinematics and interaction are believed to have positive effect on swimming performance in sea turtles. However, in this study, these features are adopted to improve power extracting performance. As the concept proofing stage of the study, the turtle-mimicking design and function of components are described and explained. Then the response and power estimation of the symmetric hydrofoil and the variable camber one are compared. At first, XFOIL software is proven reliable tool before using as tool to compute the hydrodynamics of the symmetric hydrofoil and the proposed camber one. Secondly, the response of two scenarios I and II are obtained by using the modified Dynamic model (Matlab). Thirdly, the power analysis of a symmetric and two-flap camber are explored using a pre-developed dynamic model. To provide further detail about the contribution of variable camber shape to the total efficiency at Reynold number 80,000 and 160,000, the computation by Matlab are compared with the data from experiment.

Chapter 4: The different approach for FHT is carried out with in-house CFD solver (Kflow) at a variable Reynolds number for power extraction. Three shapes of airfoil are used in right – swing tidal turbine. The shape gradually increase from zero percent camber to 39 percent camber. The force and power graphs are plotted by using MS Excel. Matlab codes are

used to compute power and power efficiency map. As the result will be utilized for the turtle-mimicking FHT project, with different shapes of airfoil (symmetric, camber) to provide insight on the response and power of turbine.

Chapter 5: the main outcomes are summarized as follow:

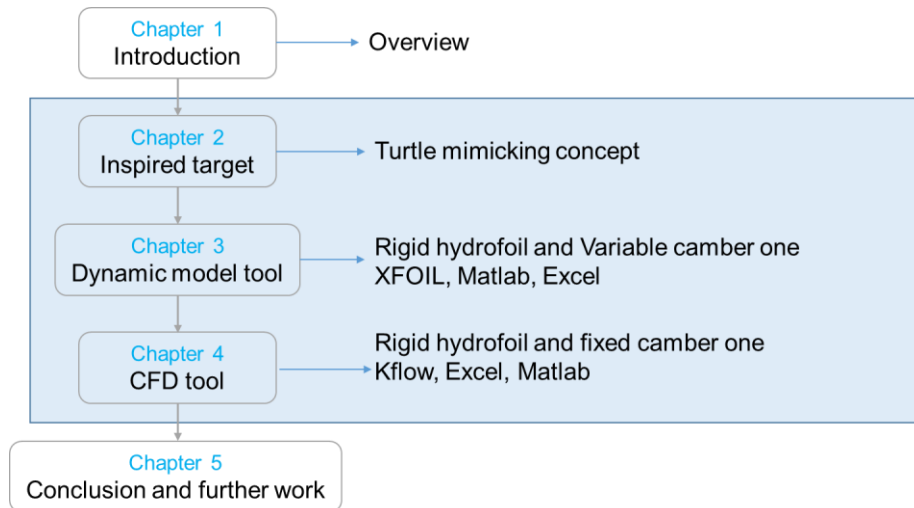


Figure 12 Outline of this dissertation

Chapter 2 Flapping tidal stream turbine

2.1 Three features inspired by a marine creature

Ocean creatures have inspired scientists and researchers by ability of moving in water. A cosmopolitan family of bivalves, scallops with convex, very corrugated and quite thin shells are able to swiftly swim quite short distances, could potential effect on a power generation ability of a flapping-type tidal stream generator – contribution by Tuyen et al. [33]. Another generator inspired by flexible pectoral fins of Manta-Ray [41] was believed to increase by an average of 22% for front flapper and 38% for rear one in the experimental conditions at KIOST in Korea in 2017. A family of ocean mammal, their tail fins own the major source of propulsion, which follow a swing sinusoidal motion symmetrical to the longitudinal body axis, existed in the research [14]. The authors believed they could obtain realistic, fascinating flow characteristics from both analyses, including the benefit of the swing motion and the beneficial wake effect, as well as the operating parameters for the dual configuration with a close distance's for optimal power performance.



Figure 13 Scallop (left) [63] and numerical work of scalloped mimicked FHT (right) [33]



Figure 14 Manta Rays (left) [64] and experimental work of Manta-Ray mimicked FHT (right) [41]

In nature, many aquatic creatures have locomotion appendages that work in a similar way to flapping wings. Sea turtles own the long flippers instead of the webbed feet of their freshwater counterparts to help them efficiently power their bodies through water. The shells of aquatic turtles have hydrodynamic shapes which play an important role in minimize the drag while swimming. Among the many species of saltwater turtles, sea turtle are selected for this and further studies.

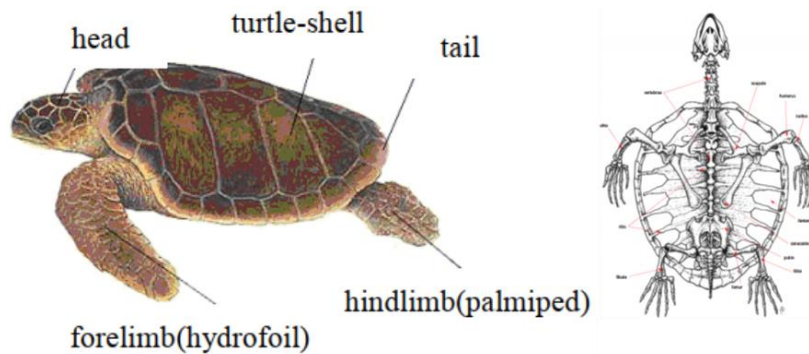


Figure 15 Sea turtle [65, 66]

In the sea, a turtle can swim quite quickly. This trait motivates us to create biological inspired turtle.

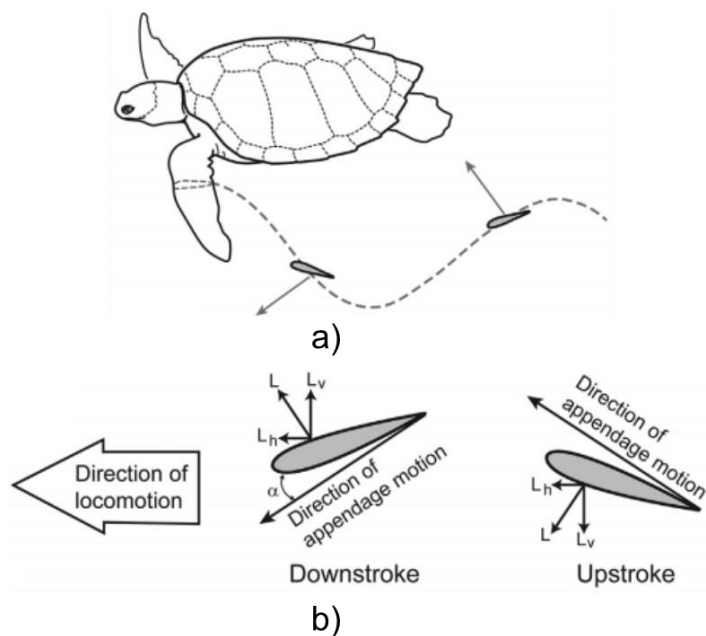


Figure 16 Swimming Trajectory of Sea turtle [67]

Fig. 16 show the “dashed line” trajectory of front flipper of a sea turtle while swimming. The contour of a cross section depicts the orientation of the hydrofoil at two points during the down stroke and upstroke, with arrows indicating the instantaneous lift at each point [67].

The procedure is nicely shown by the front flippers of a sea turtle. A turtle flaps its flippers up and down, with the down stroke having a positive angle of attack and the upstroke having a negative angle of attack. Both the upstroke and down stroke have a forward component in both halves of the stroke and vertical components that cancel each other out on each stroke half. These symmetrical hydrofoil appendages generate lift purely through angle of attack [67].

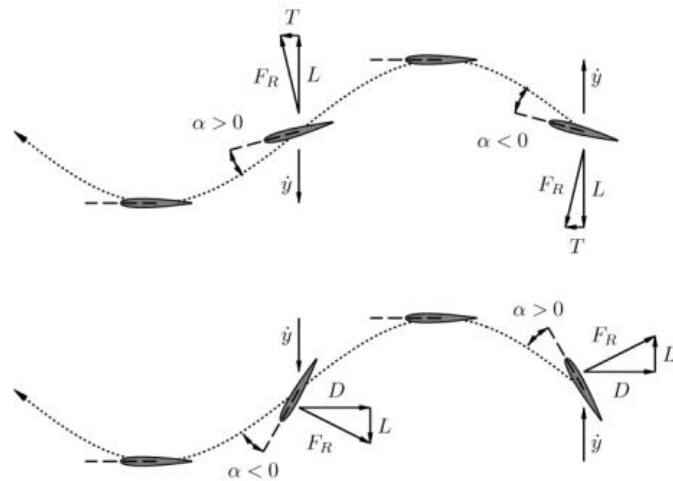


Figure 17 The operating regimes of a flapping foil, as well as the corresponding angle of attack and force directions throughout the flapping cycle [68]

In **Fig. 17**, propulsion mode is located at the top. At the bottom, there's a power generation mode [68]. Whether the foil provides thrust or power is determined on the phase of the angle of attack relative to the plunge motion. It's only natural to investigate the impact of the angle of attack trajectory (i.e. time history) on the power generation problem [68].

Previous researchers employed single hydrofoil or dual hydrofoils in their studies. However, with the ambitious to produce more power, we introduced the model mimicking turtle which has 4 single hydrofoils. The turtle, one of quadruped has four flippers for swimming, which are implemented in a mechanical system here. **Fig. 18**. Shows the concept of the system with four equal legs, which is the **first feature** simply taken from the turtle.

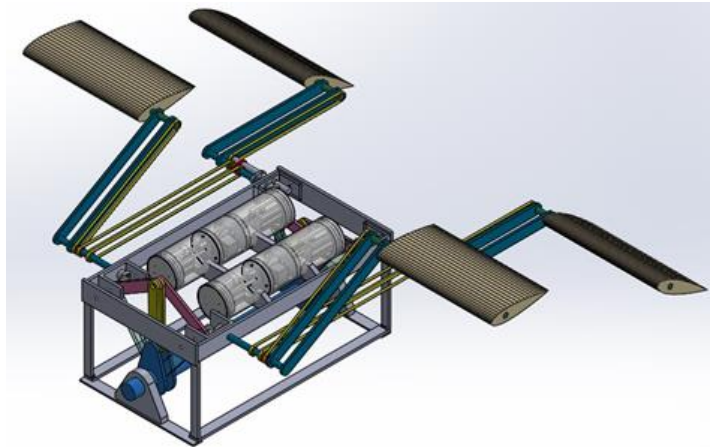


Figure 18 Artificial turtle model with four legs

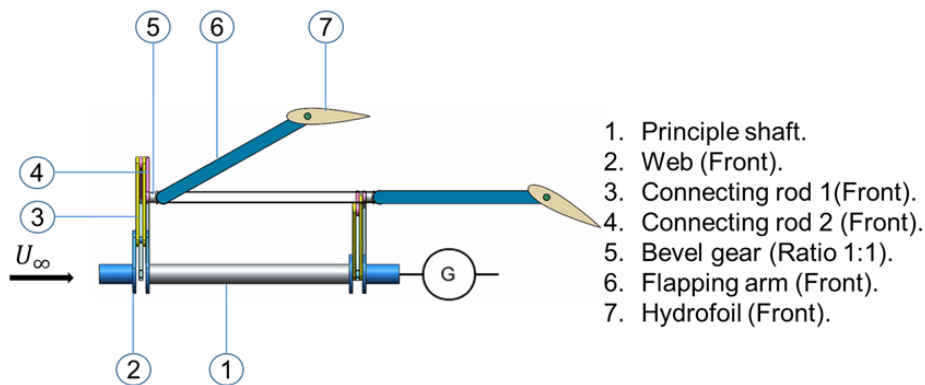


Figure 19 Power transmission of the artificial turtle model

The early stage of the design, the artificial turtle supposed to own four equal flippers or arms. The entire system comprises of the principle shaft (1) which functions like the crankshaft of the internal combustion engine. That means the crankshaft converts the forces generated by the connecting rod of four legs into the single continuous rotary motion. Hence, the main shaft (1) was made from round section. One end attached with one pair of webs (2) which links with two front flippers. Another pair of webs located near the other end connects with the two hind flippers. Another end of the shaft is the output engaged with the generator. The strong point of this design is that the motion of four hydrofoils are synchronized into the rotation of the single main shaft for transmitting that power to the generator. As expected producing phase 90° between the front legs and the hind legs, dual pair of webs are arranged 90° in the main

shaft. To prescribe pitch motion of front hydrofoil, the synchronous belt with toothed surface transmits rotary motion from swing axis of the rear hydrofoil. For prescribing the pitch motion of the rear hydrofoil, the process reverses. That is coupling of front swing and rear pitching motions and vice versa; thus, the system is categorized into fully passive system, of which motions are fully derived from flow energy.

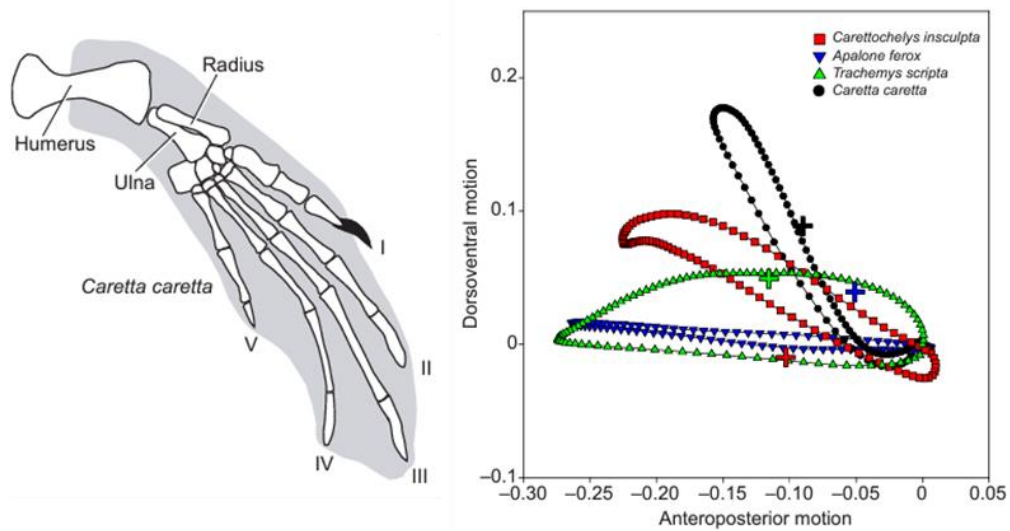


Figure 20 Bones and kinematics in a sea turtle flipper [69]

The front flipper of sea turtle (*Caretta caretta*), which is close to is in multi-joint bone structure with five fingers like human hand and it is located at rear position of its Humerus, Ulna, and Radius bones. Due to the position, anteroposterior motion of the front flipper is composed of only posterior motion as shown in **Fig. 20**, which is close to trajectory of right swing of in **Fig. 4**. Thus, the right swing trajectory as the **second feature** is taken here and is implemented in the mimicked system of **Fig. 19**.

In this study, the response (or behavior), and power of a single flipper (hydrofoil) of the turtle will be analyzed in terms of its morphology [70].

Through this dissertation, two airfoil NACA0015, NACA0012 and its variation are used. NACA airfoil has been used as modeling flipper of sea animal [71]. Also, it is known that

flippers of some turtle species have the camber shape, which is the **third feature** inspired from them. Chu [72] studied the principle of turtle motion. The author designed the bio-mechanism and tested in the transparent glass water tank. Especially, some forms high camber in their flipper and they can change their camber thanks to the multiple-joint bone structure during swimming. The “variable camber hydrofoil” is inspired from the turtle and will be investigated in terms of performance factors for FHT such as response, and power.

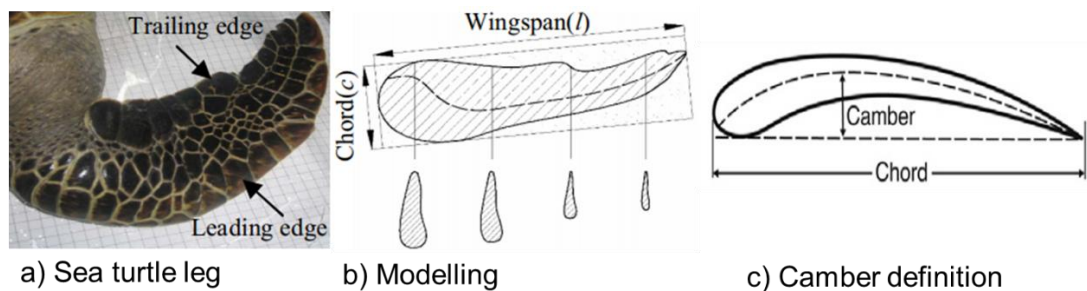


Figure 21 Turtle forelimb with camber shape [72] and camber definition [67]

The camber amplitude is defined as follows

$$\text{Camber} = \frac{h}{c} \times 100, \quad (2.1)$$

where h stands for the camber height, and c stands for chord length. The turtle are bilaterally symmetric. Hence, the force and moment calculation could be done for one side. Once turtle swims in the sea, its flippers play an important role in pushing the turtle forward. However in our project, the mimicking turtle is stationary, only water flow pass the prototype. A single flipper works as a single flapping turbine. In other words, one airfoil represents one flipper.

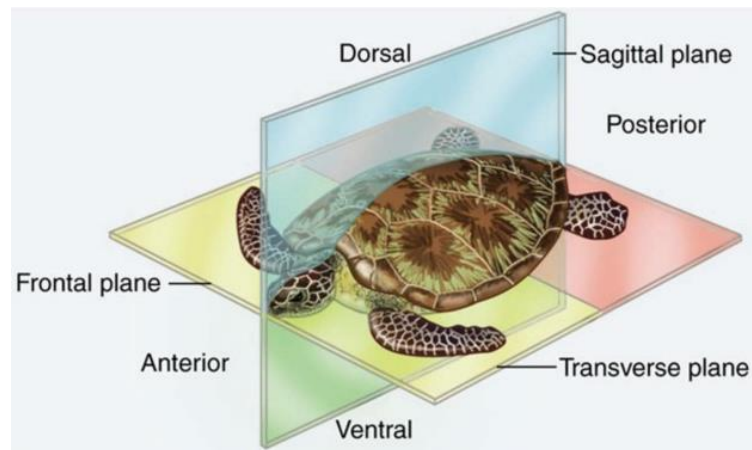


Figure 22 Bilateral Symmetry [73] of a sea turtle

In this study, an asymmetric hydrofoil, named as cambered hydrofoil with right swing trajectory in FHT is adopted. The symmetric airfoil is known as the zero camber airfoil while camber here could be categorized as fixed camber and variable cambers. In the fixed camber, the outer surface of airfoils do not vary along time variation. In contrast, the variable camber, the profile of airfoil changes along time variation.

2.2 Sub conclusion

In this section, the conceptual flapping hydrofoil turbine model mimicking a turtle with four legs was inspired from the sea turtle.

Chapter 3 Response and power analysis

3.1 Variable camber mechanism

Morphological effect on the energy harvesting for the flapping hydro turbine is interesting question that needs an answer. In order to obtain the high lift in the upstroke as well as the downstroke, variable camber mechanism with two-flap hydrofoil [74, 75] is adopted. The name of variable camber hydrofoil is used due to its ability to change the shape during flapping motion. The lift peak of camber is expect to be higher than symmetric case. The hollow space inside the hydrofoil is designed to contain the mechanisms such as several pairs of gears, transmission pulleys and belts. Airfoil receives additional power at the input shaft which is next to the pitch axis center. Two pair of gears play a role in transmitting the motion. The gear N_1 engages arc gear N_A (1:2). Simultaneously, pair of arc gear beside N_1 through timing belt move the mechanism near the trailing edge. Pair N_2N_B has the ratio 1:1. The amplitudes of the pitch angle and the desired camber decide the gear ratios. The ratio 1:1 and 1:2 was appropriate for small hydrofoil or small space inside.

Fig. 23a) presents the structure of the variable camber hydrofoil. **Fig. 23b)** shows how the hydrofoil deforms when pitch angle increases.

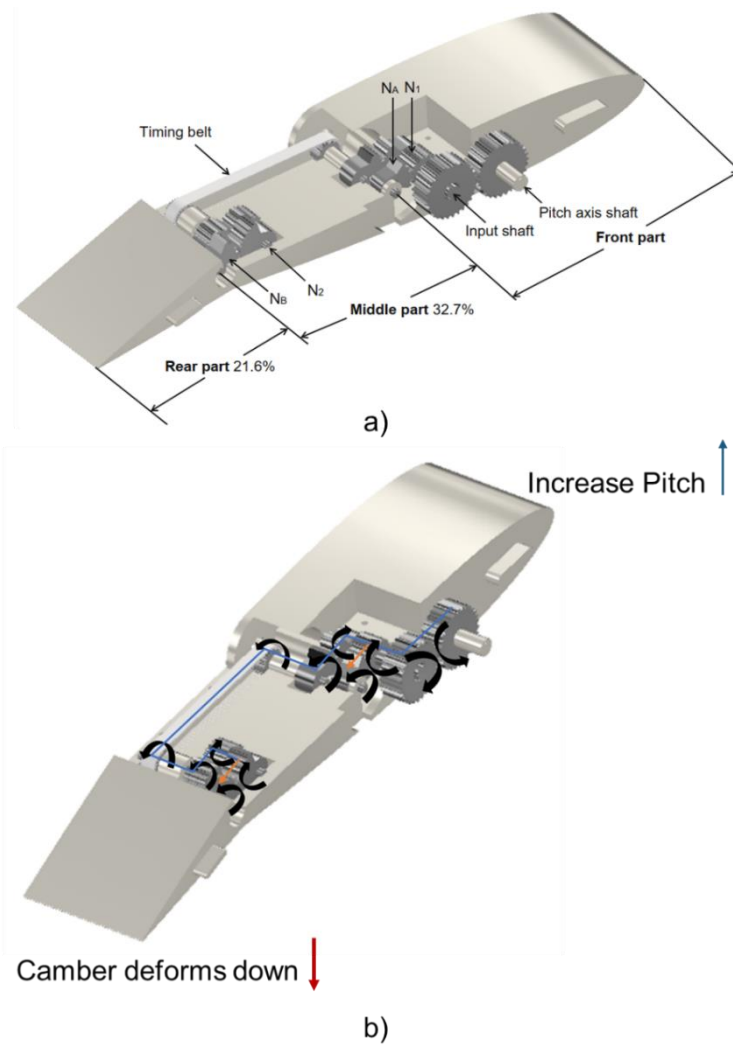


Figure 23 Camber-making mechanism inside NACA0012 hydrofoil [75]

Table 1 Technical Specifications of Hydrofoil and Flapping Arm [75]

Hydrofoil	NACA0012
Chord length (c)	0.15 m
Length of Middle part (camber)	$32.7\%c$
Length of Rear part (camber)	$21.6\%c$
Span (b)	0.29 m
Pitching axis	$0.25c$
Max. flapping angle range (ψ_{max})	$\pm 70^\circ$
Flapping arm length (l)	0.15 m

Table 1 presents some principle parameters of the first targeted system. Profiles of symmetric and camber hydrofoil are based on NACA0012 airfoil. One end of flapping arm 0.15 m is attached with pitching axis which are located at 0.25c. The total length is about 0.15 m; 32.7% and 21.6% are for the middle and the rear portion, respectively.

The input pitch angle θ of this camber type [75, 39] is calculated as follows:

$$\theta_1 = \theta \left(\frac{N_1}{N_A} \right) = 0.5\theta, \quad (3.1)$$

$$\theta_B = \theta \left(\frac{N_1}{N_A} \right) \left(\frac{N_2}{N_B} \right) = 0.5\theta, \quad (3.2)$$

$$\theta_2 = \theta \left(\frac{N_1}{N_A} + \frac{N_1 N_2}{N_A N_B} \right) = \theta. \quad (3.3)$$

A sinusoidal function with a maximum amplitude (θ_{max}) of 14° is used as the input pitch angle function:

$$\theta = \theta_{max} \sin(2\pi f), \quad (3.4)$$

where f is the pitching frequency.

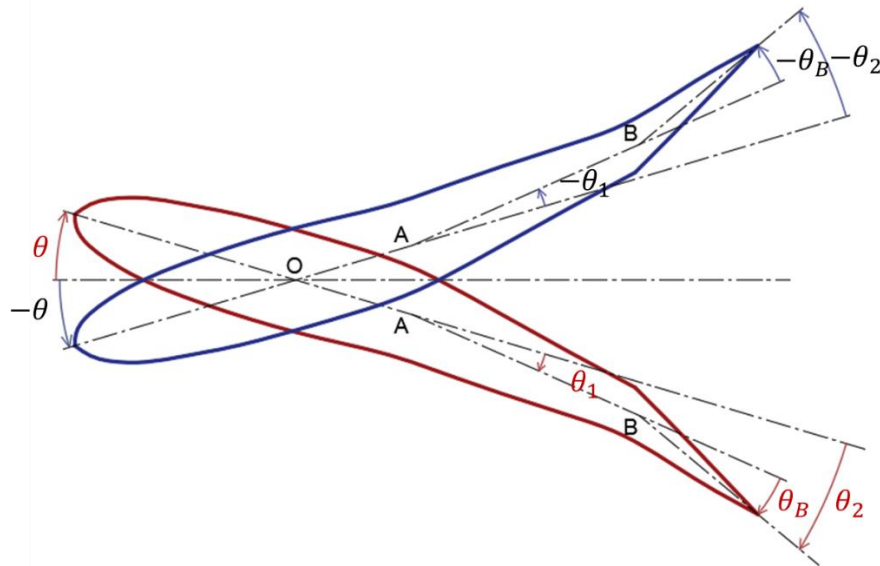


Figure 24 Angle relation of variable camber hydrofoil

The instantaneous shape of airfoil is based on the instantaneous input value of pitch θ : $0^\circ, 2^\circ, 6^\circ, 10^\circ, 14^\circ$ are the maximum value of θ_2 respectively. Once the hydrofoil receives

positive pitch θ ; the equation (3.1), (3.2) and (3.3) have all positive signs. The original symmetric shape gradually deform downward (red color). In contrast, the hydrofoil receives negative pitch $-\theta$; the equation (3.1), (3.2) and (3.3) have all negative signs. The symmetric shape deforms upward (blue color). Due to existence of the arc gears along with small ratio, the pitch angle amplitude was limited with the maximum 14 degrees.

Table 2 Positive Deflection Angles and Camber as the result of the Pitch angle [75]

θ (°)	θ_1 (°)	θ_2 (°)	Camber (%)
0	0	0	0
2	1	2	7
6	3	6	21
10	5	10	30
14	7	14	39

In **Table 2**, column 1 and column 4 have the relationship expressed in **Eq. 2.1**. Once pitch = 0, based on the equation 1 the airfoil has zero camber. Likewise at the highest pitch, the airfoil reaches 40% percent amplitude of camber.

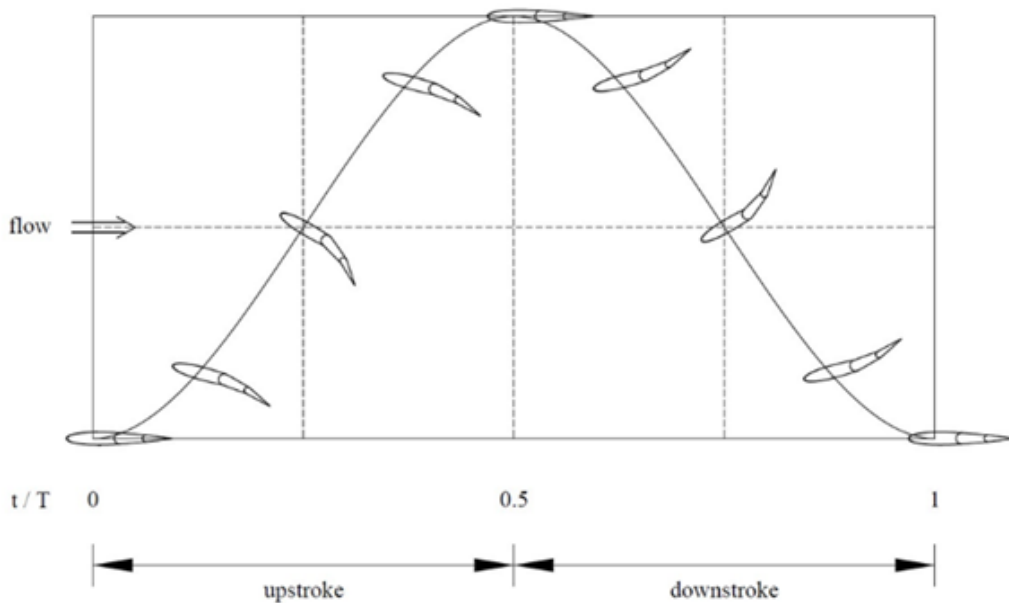


Figure 25 Flapping motion with a variable camber hydrofoil during pitch variation in one period

Fig. 25 depicts in a single cycle, the movement of the hydrofoil along with the development of camber. The pitch angle is 0 and the hydrofoil has a symmetrical shape at time step, $t/T = 0$. A positive camber is generated by turning sections near the trailing edge in the downward direction when $0 < t/T < 0.5$ as the pitch angle rises. The airfoil returns to its original symmetric shape at the top of the upstroke. In contrast, during the down stroke, the hydrofoil deforms in the opposite direction but a positive camber is formed as well. It is obvious that there is no flap formation at the starting or at the middle and ending times of the cycle. At time steps $t/T = 0.25$ and 0.75 , the hydrofoil reaches its maximum positive camber, which causes high lift during both strokes to maximize power extraction.

3.2 Hydrodynamics prediction of a cambered hydrofoil

3.2.1 XFOIL as predicting tool

XFOIL is best known for analysis and a design system ability for Low Reynolds Number Airfoils, was developed by Professor Mark Drela in Massachusetts Institute of Technology (MIT) in 1986. It combines the speed and accuracy of high - order panel methods with fully-coupled viscous/inviscid interaction [76]. XFOIL was picked in this section due to its ability to provide quite accurate results. The strong point is that it could give outcomes much more rapidly than the CFD (Computational Fluid Dynamics) tool, moreover it is a free software [77]. Before using XFOIL program in this research, hydrodynamic characteristics (C_L , C_D , C_M) NACA0012 airfoil obtained by XFOIL are compared to data of other researchers.

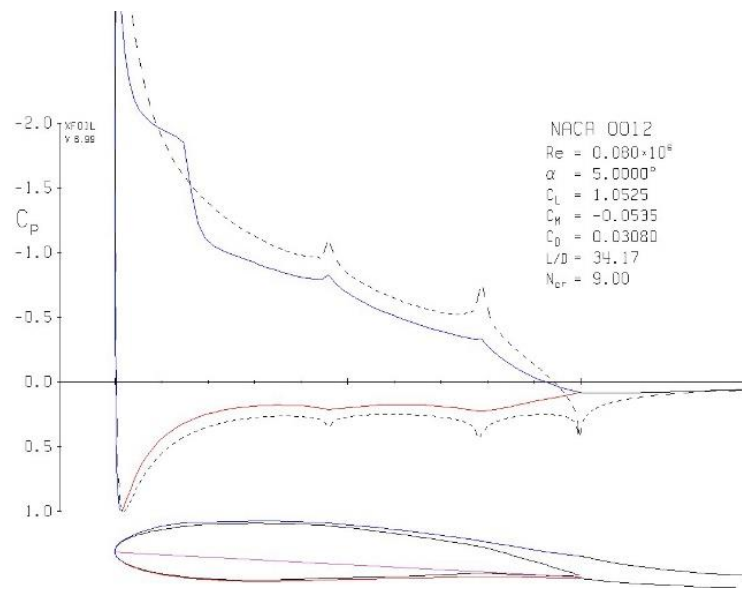


Figure 26 C_p and streamline plot of camber hydrofoil at $Re = 80,000$, $N_{cr} = 9$ in XFOIL [39].

In **Fig. 26**, the hydrodynamic coefficient (C_L , C_D and C_M) computed by XFOIL were shown with specific $N_{cr} = 9$ (average wind channel). The light blue curve represents the pressures over the upper surface, while the red curve represents the pressures over the lower surface. Lift is generated due to on the lower surface and negative pressure on the upper surface.

1) Validation at two Reynolds numbers of 40,000 and 100,000

The selected Reynolds number for the first target system use in current research is 80,000 and 160,000. Thus, the first Reynold number 40,000 which is half than interested 80,000 and the second one is 100,000 which is nearly in middle of the 160,000. In this section, the simulation data by XFOIL are compared with the experimental data. Ohtake [78] conducted the experiments in closed tunnel.

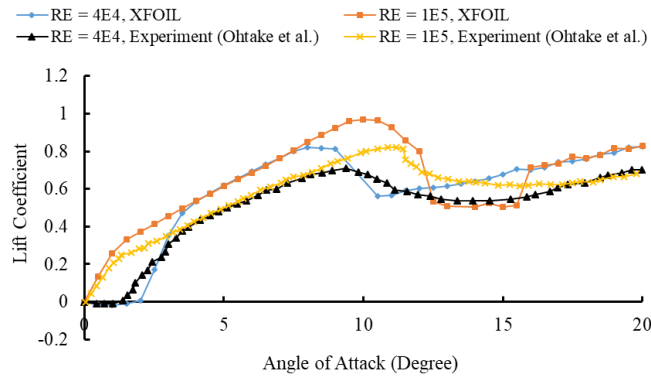


Figure 27 Lift coefficients of NACA0012 [39] at $Re = 4 \times 10^4$ and $Re = 10^5$

Lift coefficients data of 4 digit airfoil NACA0012 from XFOIL are compared with lift coefficients taken in wind tunnel at two quite low Reynolds number 4×10^4 and 10^5 . The output from XFOIL at 4×10^4 shows a similar trend with experimental data. The lift coefficients rises to about 9 degrees, shows a stall at the angle and then increases again to 20° . With $Re = 10^5$, consequently, the coefficient of lift is bigger and the stall is delayed over 10° in experiment data as well as XFOIL.

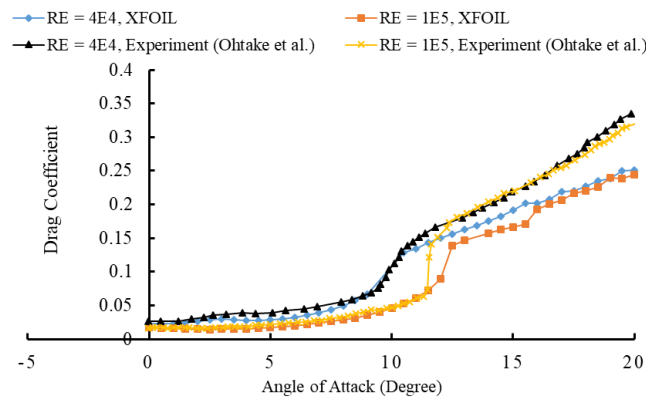


Figure 28 Drag coefficients of NACA0012 [39] at $Re = 4 \times 10^4$ and $Re = 10^5$

The drag coefficients computed by XFOIL and measured in the wind tunnel show similar trend as well. At Reynolds number 4×10^4 , a steep increase starts at nearly 9° and a similar steep increase begins later at around 12° for $Re = 1 \times 10^5$. In general, the result of XFOIL are much closer to those of the experiments with a short range of AoA -8° to 8° .

2) Validation at two Reynolds numbers of 80,000 and 160,000

Two Reynolds numbers are identical with the targeted range. The graph below shows the comparison among the output of Xfoil, result of Javafoil and experimental data in KIOST. Javafoil is a quite simple program due to pretty well organized interface. Its uses two methods: the potential flow analysis and the boundary layer analysis [79]. One merit of Javafoil compare to XFOIL is that it have Stall Corrections function [80]. The experiment was set up in a circular water chanel (CWC) facility of Seoul National University in Korea [81]. The hydrofoil was placed in the midway, $0.5c$ away from the ground and the free surface.

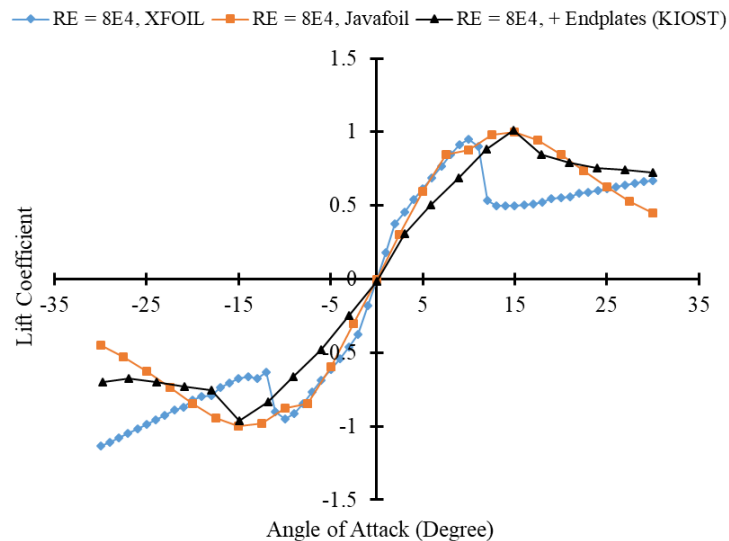


Figure 29 Comparison of the lift coefficients for NACA0012 [39] at $Re = 8 \times 10^4$

For Reynolds number 80,000, in short range of AoA -8° to 8° , the output of two program XFOIL and Javafoil - lift coefficients and drag coefficients in **Figs. 29** and **30** are almost identical.

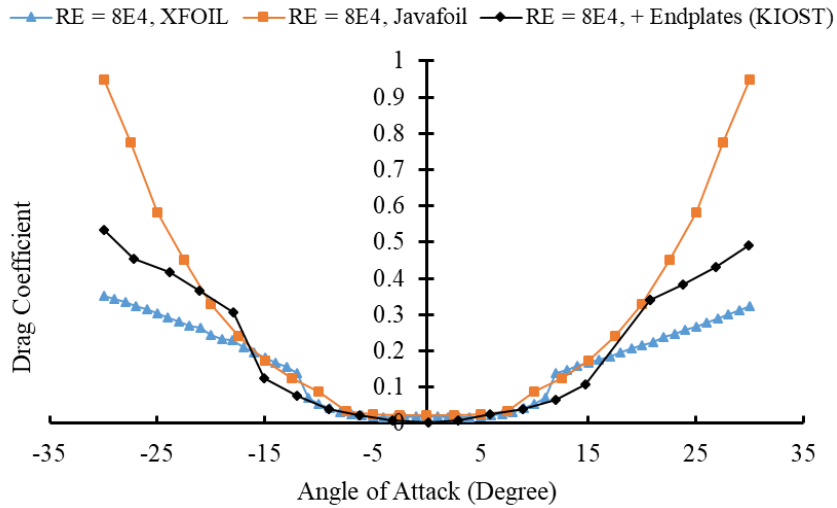


Figure 30 Comparison of the drag coefficients for NACA0012 [39] at $Re = 8 \times 10^4$

When compared to experimental data in this range, XFOIL has a relative difference of 0.41 while Javafoil has a relative difference of 0.48. Meanwhile, XFOIL data does not match experimental data in terms of stall angle outside of this range because XFOIL forecasts the stall angle less correctly [82], whereas Javafoil with experimental stall correction does. We picked XFOIL for this study because it produces results that are somewhat similar to experimental data in the targeted range.

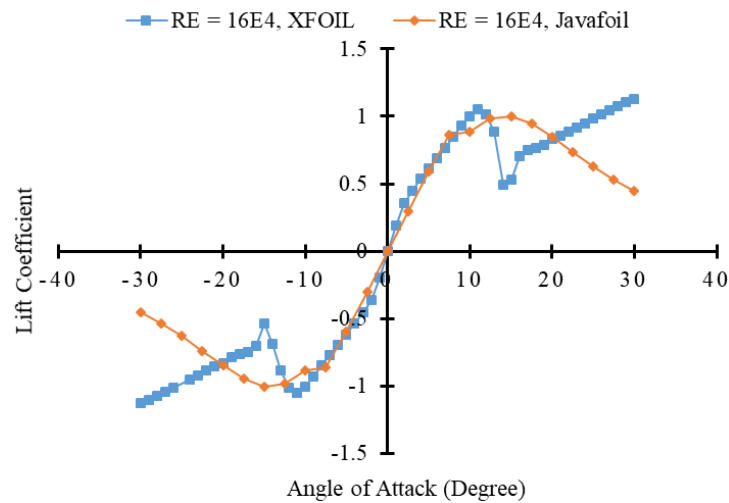


Figure 31 Lift coefficients of NACA0012 [39] at $Re = 16 \times 10^4$

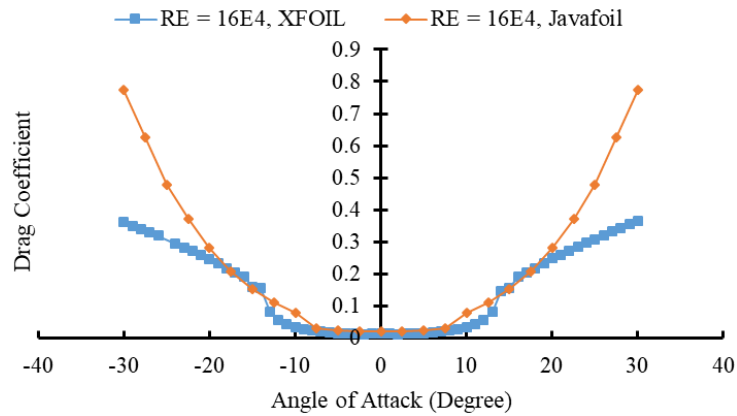


Figure 32 Drag coefficients of NACA0012 [39] at $Re = 16 \times 10^4$

As shown in **Fig. 31** and **32**, at $Re = 160,000$ in a short range of the AoA from -8° to 8° , the lift coefficient and drag coefficients as estimated by XFOIL are similar to those by Javafoil.

From these validations, we found that the XFOIL software provided reliable hydrodynamic characteristics in the short range of the AoA from -8° to 8° .

3.2.2 Hydrodynamics of cambered hydrofoil

The Lift coefficients by XFOIL at $Re = 80,000$ of zero camber to maximum camber along with experimental data by Sandia National Laboratories (SNL) are depicted in **Fig. 33**.

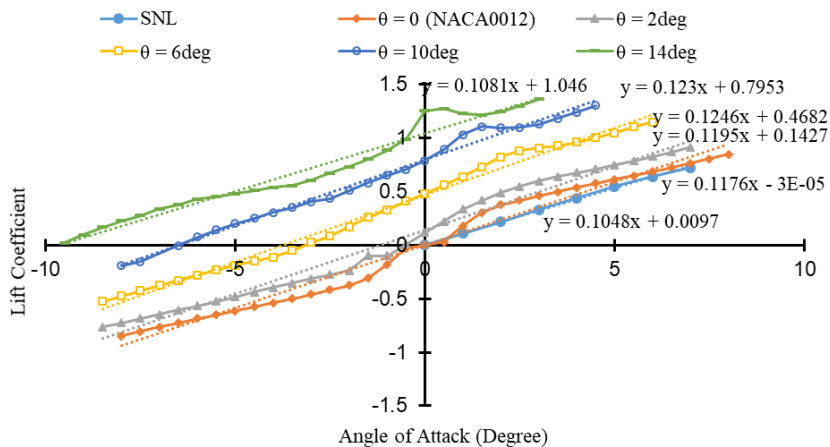


Figure 33 Lift coefficients versus AoA at $Re = 80,000$

The XFOIL results of the zero camber NACA0012 after linear regression are similar to the experimental data. Due to the computation approach utilized by XFOIL, which causes high pressure spikes at the leading edge at tiny lift coefficient, the local peak of XFOIL as contrasted to the regression line or SNL data occurs near 0° AoA. As pitch increases, the peak amplitude increases. At a higher pitch angle, which indicates more camber, the peak amplitude becomes bigger than at a lower pitch angle, which means less camber. This pattern was also reported in a previous study [83]. As a result, for C_L , we employed linear regression. The computed data from XFOIL was used as computed for C_D . **Fig. 34** and 35 show the final C_L and C_D datasets for a variable camber hydrofoil at $Re = 80,000$, respectively.

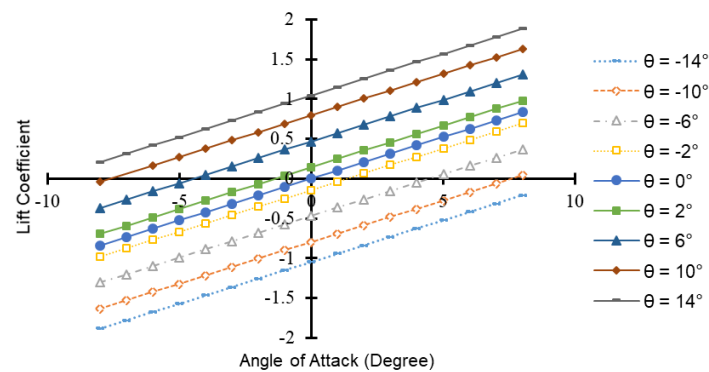


Figure 34 Lift coefficients for a cambered hydrofoil [39] at $Re = 80,000$

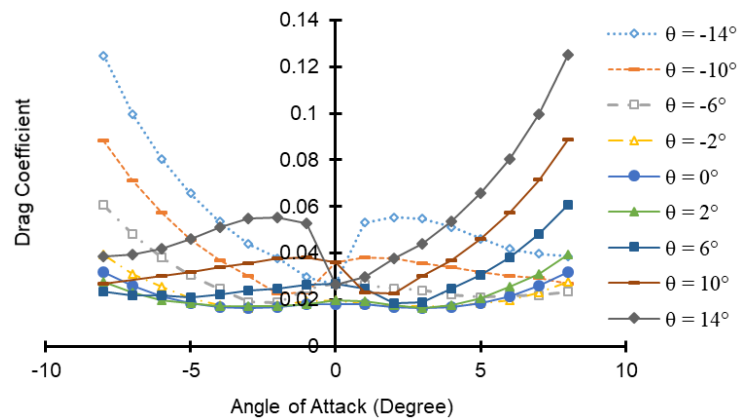


Figure 35 Drag coefficients for a cambered hydrofoil [39] at $Re = 80,000$

The input pitch angle is represented by the symbol θ . The lift coefficient increases as the input pitch angle increases, with the lowest lift coefficient at a pitch angle of -14° and the highest lift coefficient at a pitch angle of 14° .

According to the graph, the tendency of lift proportion to the tendency of pitch. The smallest value of lift when pitch $\theta = -14^\circ$, in the middle when pitch is zero and the lift reach highest value for pitch $\theta = 14^\circ$, respectively. These lines are symmetric about the symmetric NACA0012 or zero camber.

In **Fig. 35**, the drag coefficients drop dramatically near zero AoA for positive pitch angles of 10° and 14° . The drag coefficients for all pitch angles rise as the AoA increases. At a pitch angle of 14° , the greatest drag coefficient is recorded. Negative pitches's drag curves are similar to those of positive pitches.

Likewise, C_L and C_D are calculated using the same method at $Re = 160,000$. In **Fig. 36** and 37, the lift coefficients and drag coefficients are plotted respectively.

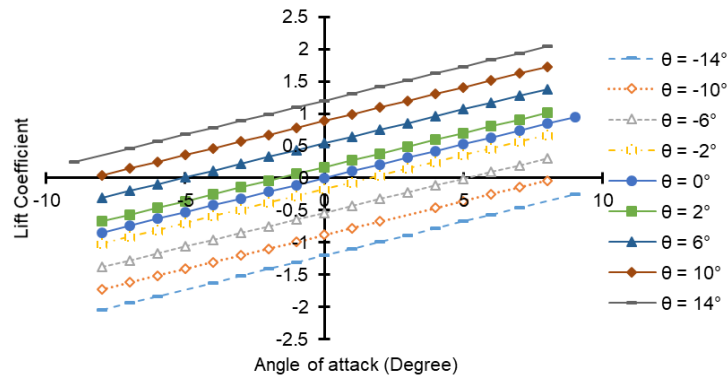


Figure 36 Lift coefficients for a cambered hydrofoil [39] at $Re = 160,000$

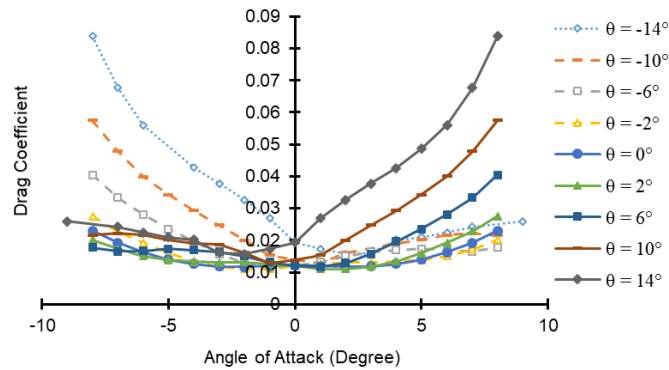


Figure 37 Drag coefficients for a cambered hydrofoil [39] at $Re = 160,000$

When Reynolds number is equal to 160,000, the lift coefficient also rises as the input pitch angle rises. The sharp decline in the drag coefficient near zero AoA vanished. The drag coefficients for positive pitch angles gradually grow as the AoA increases. At the greatest pitch angle, the maximum drag coefficient is observed. Negative pitch angles have drag coefficients that are similar to positive pitch angles.

In the upcoming dynamic response estimation, the hydrodynamic characteristic data provided in the **Fig. 34** to **37** become the inputs. Only the linear region of only C_L data is approximated before a stall. Hence the data only correspond to the state before a stall. As a result, after the stall condition, the dynamic model for the variable camber hydrofoil can not be used in a simulation. In the dynamic model with Matlab, C_L and C_D have the same AoA range.

3.3 Dynamic model as an estimating tool

The dynamic model named in this chapter describes how the system properties vary over time. Normally, the tool for solving the tidal turbine's problem are the experiment with the prototype or numerical computation with CFD. The approach used dynamic model first introduced by Tri et al. [38, 84, 85, 86]. Here, a flapping arm along with a hydrofoil is a representative for a single FTT or one leg of the turtle. A free body diagram consists a flapping arm and hydrofoil is shown in **Fig. 38**. **Eqs. 3.5** to **3.11** are related to dynamic model by Tri et

al. [38]. First, the relative velocity amplitude is the result of incoming flow and the airfoil and is defined in the diagram:

$$W = \sqrt{W_x^2 + W_y^2} = \sqrt{(V_\infty + l\dot{\psi} \sin\psi)^2 + (l\dot{\psi} \cos\psi)^2} . \quad (3.5)$$

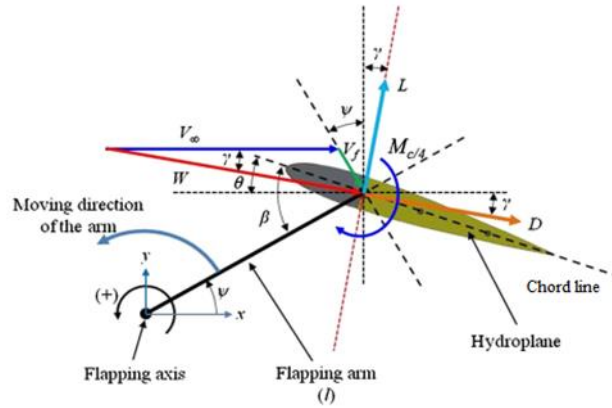


Figure 38 Free - body diagram of turbine [38]

Symbol l , V_∞ , ψ , and $\dot{\psi}$ are the flapping arm length, velocity of the far-field inflow, flapping angle, and flapping speed, respectively. Next, the lift and drag acting on the hydrofoil are determined as follows:

$$L = \frac{1}{2} \rho C_L S [(V_\infty + l\dot{\psi} \sin\psi)^2 + l^2 \dot{\psi}^2 \cos^2\psi], \quad (3.6)$$

$$D = \frac{1}{2} \rho C_D S [(V_\infty + l\dot{\psi} \sin\psi)^2 + l^2 \dot{\psi}^2 \cos^2\psi], \quad (3.7)$$

$$M_{c/4} = \frac{1}{2} \rho C_M S c [(V_\infty + l\dot{\psi} \sin\psi)^2 + l^2 \dot{\psi}^2 \cos^2\psi], \quad (3.8)$$

where ρ , C_L , C_D , and S are density of water, lift, drag coefficients, and the area of the hydrofoil, respectively [38]. The hydrofoil's lift, drag, and moment coefficients, or hydrodynamic properties, are functions of the effective angle of attack (α).

The effective angle of attack is the resulting angle expressed by the pitch angle (θ) and relative flow direction (γ), which is given as follows:

$$\alpha = \theta + \gamma, \quad (3.9)$$

where

$$\gamma = -\tan^{-1}\left(\frac{W_y}{W_x}\right). \quad (3.10)$$

The nonlinear dynamic equation of motion of the hydrofoil can be described as

$$I\ddot{\psi} = (L \cos \gamma + D \sin \gamma)l \cos \psi - (L \sin \gamma - D \cos \gamma)l \sin \psi - I_g \ddot{\psi} - C\dot{\psi} - \frac{M_c}{4} + \tau, \quad (3.11)$$

where I is the mass inertial moment of the hydrofoil-flapping arm around the flapping axis, I_g is the equivalent mass inertial moment of the gear box system around axis of the driving gear, C is the damping coefficient of the transmission system and γ is the deflection angle of the flow.

3.3.1 Dynamic model validation

A series of experiments were carried out to measure the system's response in order to validate the dynamic model [38]. Four different cases of the input signals were tested in the water tunnel. Digital camera captured the pitch angle of the hydrofoil and the flapping angle [38], which are listed in **Table 3**.

Table 3 Measured Responses of the Prototype with Symmetric Hydrofoil [38]

Case	Sum of Pitch angle amplitude, $\theta_1 + \theta_2$ (°)	Holding Torque, T (N·m)	Flapping frequency (Hz)	Flapping angle amplitude, $\theta_1 + \theta_2$ (°)
A1	58	0	0.275	112
A2	53	0.2	0.231	97
B1	73	0	0.4	108
B2	74	0.2	0.4	87

3.4 Response analysis

This semi-passive arm transfer the oscillating motion of the hydrofoil to the principle shaft while input pitch from the stepper motor to the hydrofoil. For the power analysis, two scenarios are defined, referred to here as scenario I and scenario II. In both scenarios, the power values of the symmetric and variable camber hydrofoils with the dynamic model are compared.

In scenario I, the hydrodynamic characteristics (C_L , C_D , and C_M) of the symmetric NACA0012 hydrofoil and the two-flap NACA0012 hydrofoil are numerically computed under the condition of an identical holding torque ($\tau = 0.2 \text{ N}\cdot\text{m}$). In this research, two cases, termed case A2 and B2, with parameters from a previous study were selected [39]. Note that all of the dynamic response estimations have an identical sinusoidal pitch angle with an amplitude of 14 degrees. The primary output of the equation of motion as the response is the flapping angle, which is used to calculate the available, hydrodynamic and extracted power values. With the same holding torque, the flapping angle of the variable camber hydrofoil is much larger than that of the symmetric foil, as reported in the aforementioned study [39].

As the torque increases, the peak value of the flapping response of the variable camber hydrofoil decreases and becomes close to that of the symmetric hydrofoil. This is named as scenario II.

3.4.1 Response of scenario 1

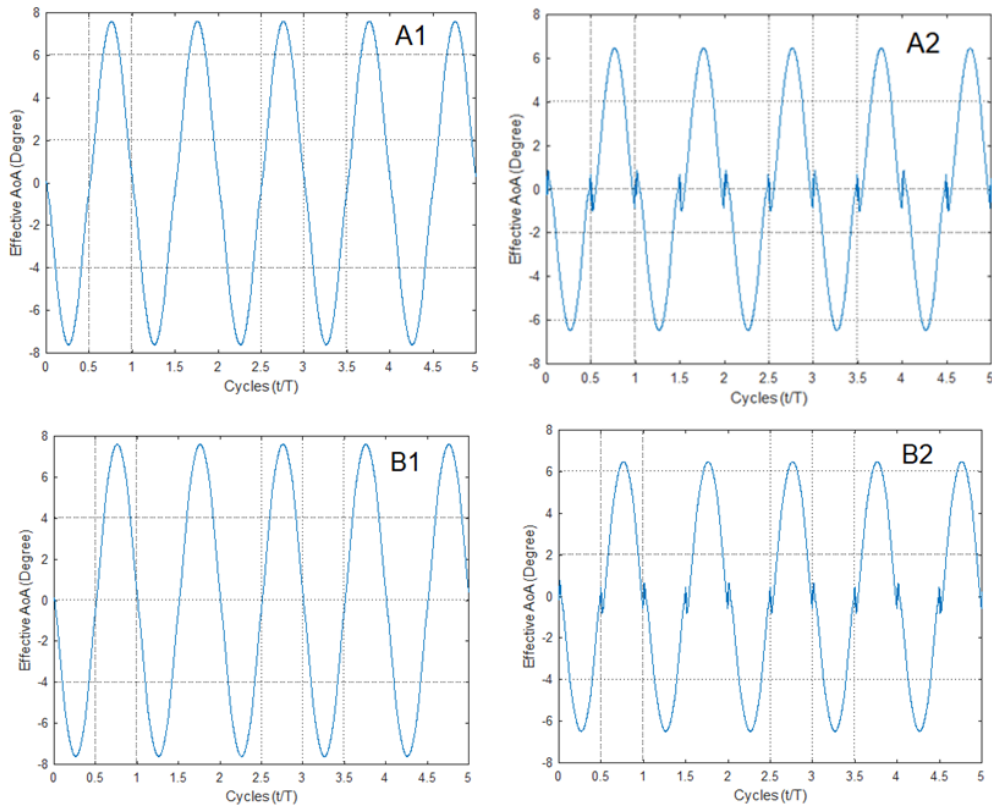


Figure 39 Effective AoA of a variable camber hydrofoil for the A1, A2, B1 and B2 cases

Fig. 39 shows the Effective AoA of full 5 cycles of four cases [39]. According to that Figure the maximum effective AoAs for all cases are smaller than 8 degree. In case A2 and B2, a slight fluctuation near a zero effective AoA and declining amplitudes are consequence of deploying holding torque.

The main output of dynamic model in this research is flapping angle of symmetric and camber hydrofoil which is plotted along with observation data. The orange line looks sinusoidal curve which is the pitch angle of symmetric or cambered hydrofoils of current study while gray dash line represents the pitch curve of experiment. In term of flapping frequency, the low flapping frequency ($f = 0.275$ for A1, $f = 0.231$ for A2) lead to higher flapping angle than high flapping frequency ($f = 0.4$ for B1, B2). All four graphs show that the camber cases produce higher flapping angle than the symmetric cases due to increasing lift coefficient.

Note that the symmetric and cambered cases share the same input angle function. As shown in **Fig. 40**, the variable camber hydrofoil are able to generate a larger flapping angle than the symmetric hydrofoil because of its higher lift. The flapping response amplitudes of the variable camber hydrofoil in case A1 and case A2 are nearly twice the flapping response amplitude of the symmetric hydrofoil for the same pitch angle. With holding torque in the B2 case, the discrepancy of the flapping response amplitude of the variable camber hydrofoil and symmetric hydrofoils becomes much larger than in the B1 case without holding torque. As a result, the suggested variable camber hydrofoil with pitching motion may be preferable to a symmetric hydrofoil with only pitching motion if smaller camber changing power is required relative to pitching power.

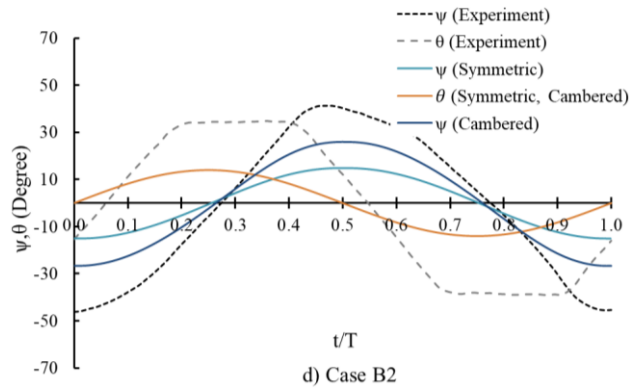
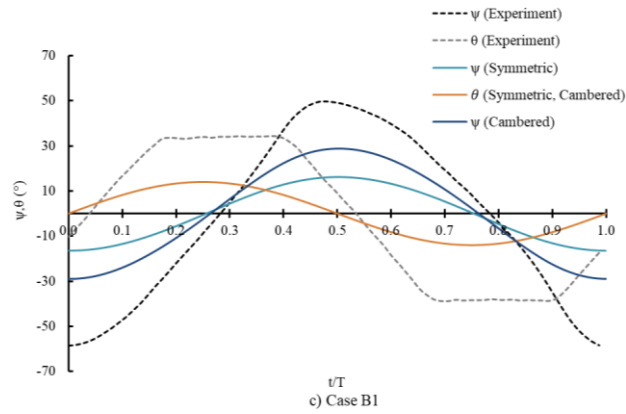
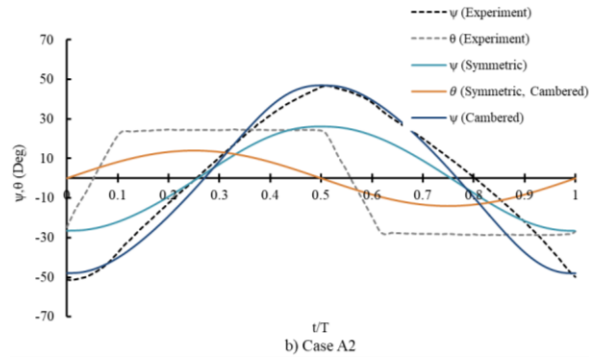
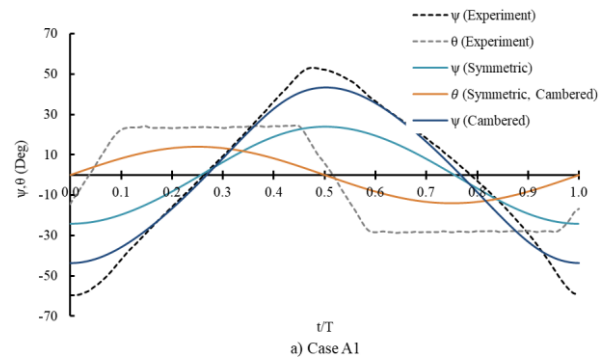
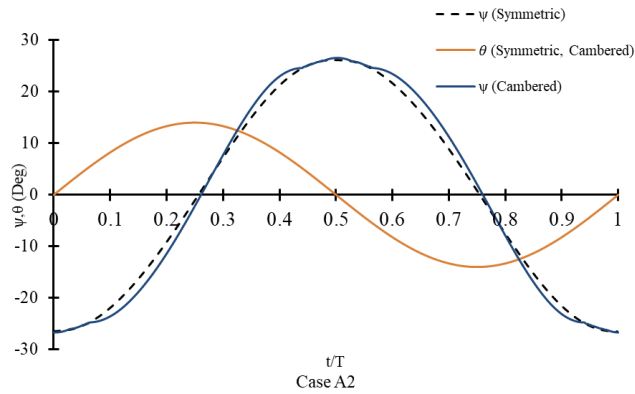
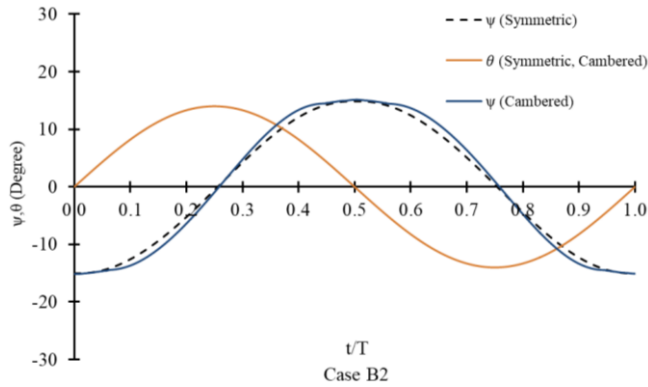


Figure 40 Responses of scenario 1 [39]

3.4.2 Response of scenario 2



a)



b)

Figure 41 Responses of scenario 2

Scenario 2, unlike scenario 1, is composed of different torque – applied cases. Hence, in this scenario, simulations are conducted with case A2 and case B2. In order to have equal response between symmetric and cambered ones, the specific value of torque 1.25 N·m for cambered one is chosen and the responses are depicted in **Fig. 41**. Here the only changed value is the holding torque. That means the phase angle or frequency is identical with Scenario 1.

3.5 Power analysis

3.5.1 Power of scenario 1

1) Available power and Input power

For the flapping hydrofoil turbine, the kinetic energy of the fluid flow can be turned into mechanical energy. Therefore, the equation of the maximum available energy, P_a , which was considered initially, can be calculated using the following formula [87]

$$P_a = \frac{1}{2} \rho V_\infty^3 A = \frac{1}{2} \rho V_\infty^3 b d, \quad (3.12)$$

where A is the swept area of the hydrofoil, b is the hydrofoil span, d and x_p are the height of the hydrofoil during vertical motion and the location of the pitching axis from the leading edge.

The vertical height of the hydrofoil (d), as shown in **Fig. 42**, is defined by

$$d = (l \sin \psi_u + x_p \sin \theta_u) + (l \sin \psi_d + x_p \sin \theta_d), \quad (3.13)$$

where u and d (in subscript) represent the upstroke and downstroke, respectively.

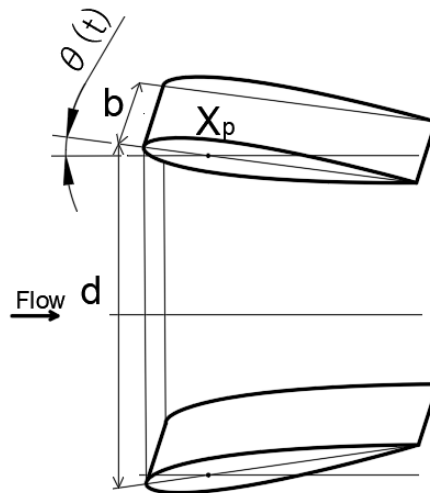


Figure 42 The wing span b and the vertical height d of the hydrofoil

First, the available power values calculated by **Eqs. 3.12 - 3.13** are listed in **Table 4**, in which *s* represents the symmetric foil, *c* stands for the variable camber hydrofoil, the subscript *u* denotes the upstroke and the subscript *d* represents the down stroke.

Table 4 Available Power Values for the Symmetric and Cambered Hydrofoils

Case	A2s	A2c	B2s	B2c
ψ_u (°)	26.1	47.775	15.06	26.5
ψ_d (°)	26.5	47.235	14.89	26.14
d (m)	0.164	0.273	0.096	0.164
P_a (watt)	4.625	7.696 (66.41%)	2.697	4.628 (71.59%)

The discrepancies in the flapping amplitudes between the symmetric and variable camber hydrofoils in the second row and third rows of **Table 4** are considerable. Consequently, the available power values for A2c and B2c in the last rows are much higher than those for A2s and B2s, respectively. The rates of the increases are 66.41% and 71.59% for A2c and B2c, respectively. Specifically, the variable camber hydrofoil extracts more power by least 66 percent than the symmetric hydrofoil due to the relatively large response.

The input power, the second factor considered, is the supplied power for the stepper motor to create a particular pitching motion to generate flapping motion. In this research, the mass moment of inertia of the hydrofoil about the pitch axis is assumed to be negligible and the center of mass of the hydrofoil is collocated with the pitch axis. Thus, the power required to change the pitch angle in a symmetric hydrofoil turbine is described by the equation below

$$P_{in}(t) = M_{c/4}(t)\dot{\theta}(t). \quad (3.14)$$

Here, $M_{c/4}$ is the pitch moment at the quarter-chord point according to the hydrodynamics, and $\dot{\theta}$ is the input pitch rate.

Meanwhile, the equation used to calculate the input power of the variable camber hydrofoil, for which camber changing energy is required, is modified to

$$P_{in}(t) = M_{c/4}(t)\dot{\theta}(t) + Mf_1\dot{\theta}_1(t) + Mf_2\dot{\theta}_B(t), \quad (3.15)$$

where Mf_1 and Mf_2 are the moments at flap pivot axes 1 and 2 in **Fig. 43**, respectively, and

$$\dot{\theta}_1 = \frac{\dot{\theta}}{2}, \quad \dot{\theta}_B = \frac{\dot{\theta}}{2}.$$

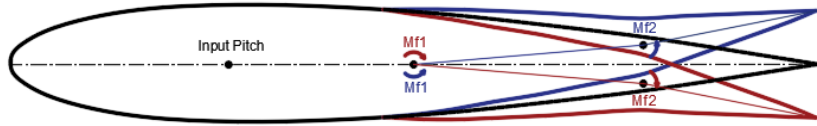


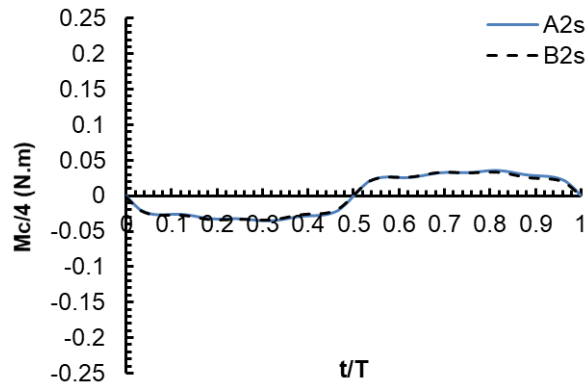
Figure 43 Moment at the flap 1 and flap 2

Fig. 43 shows three states of the time-changing camber. First, Mf_1 and Mf_2 have value of zero, there is no existence of camber and hydrofoil in black line. Second, Mf_1 and Mf_2 have clockwise rotation, hydrofoil bends downward (red color) form a positive camber. In contrast, Mf_1 and Mf_2 have counter-clockwise rotation, hydrofoil bends upward (blue color) form a negative camber.

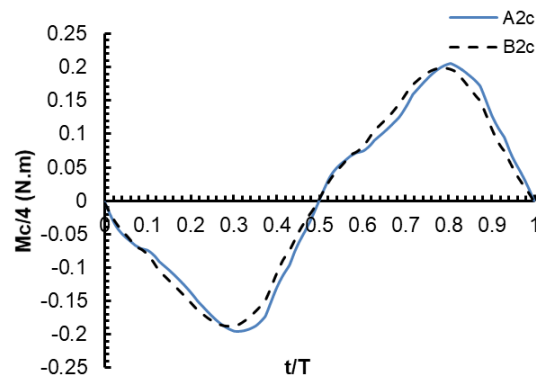
The original XFOIL software did not have a function for calculating flap moments 1 and 2; thus, the XFOIL code in Matlab [88, 89], was modified to compute flap moments 1 and 2 of the variable camber hydrofoil. Subsequently, the Matlab program for the dynamic model was modified to read the input and apply the flap moments in this power analysis. The instantaneous input power $P_{in}(t)$ and the time-average power denoted as \bar{P}_{in} can be expressed as follows:

$$\bar{P}_{in} = \frac{1}{T} \int_0^T |P_{in}(t)| dt. \quad (3.16)$$

Meanwhile, the input power for the variable camber hydrofoil is expected to be larger than that of the symmetric one. Graphs of pitching moments of the symmetric and variable-camber hydrofoils are given in **Fig. 44**.



a) Symmetric hydrofoil

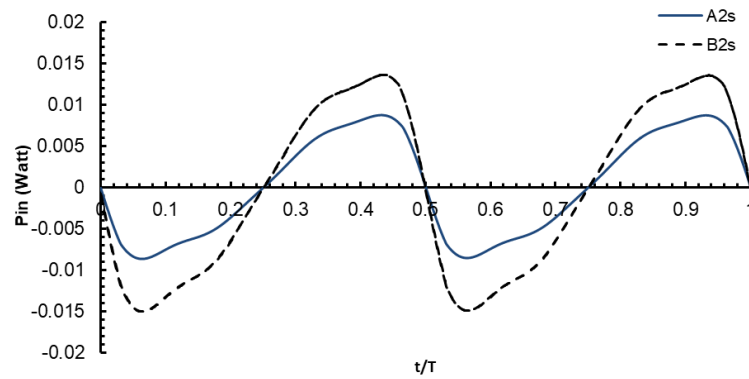


b) Variable camber hydrofoil

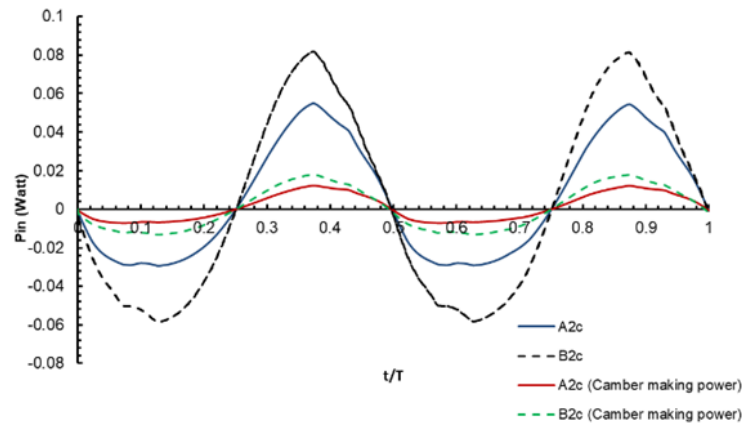
Figure 44 Pitching moment of symmetric and variable camber hydrofoils

The peak in the variable camber case ($0.2 \text{ N}\cdot\text{m}$) is nearly five times larger than the peak in the symmetric case ($0.035 \text{ N}\cdot\text{m}$) because the cambered hydrofoil moves in the higher pressure zone, which causes higher lift compared to that of the symmetric hydrofoil. Meanwhile, the variable camber hydrofoil has a pitching speed, which is an input parameter, identical to that of the symmetric case. The input power values calculated from **Eqs. 3.14-3.15** are depicted in **Fig. 45**, where the positive peaks of the variable camber hydrofoil are nearly five times those of the symmetric hydrofoil, whereas the negative peaks of the variable camber hydrofoil are almost four times those of the symmetric hydrofoil due to the different contributions of the camber-making portion in **Eq. 3.15**. In the first and third quarters in **Fig. 25**, the camber is increased from zero to the maximum value and negative power is then

generated, as shown in **Fig. 45(b)**, while in the second and fourth quarters, the camber is decreased from the maximum value to zero and positive power is then extracted. During the camber-making and removal procedures, the different amplitudes of moments Mf_1 and Mf_2 cause the different contributions of the corresponding input power.



a) Input power of symmetric one



b) Input power of variable camber one

Figure 45 Input power of symmetric and variable camber hydrofoils

Practically, in order to generate a particular pitching motion, the step motor supplies input power to the hydrofoil. Variable camber hydrofoils need extra input power to transmit the inside mechanism that generates the cambered shape during the flapping motion. A negative sign of the input power in the first and third quarters in **Fig. 45** means that the stepper motor requires torque to counteract the pitching moment. Thus, the amounts of actual input

power, which are the overall negative areas, and the corresponding average input power values of the two quarters are listed in **Table 5**. The negative areas of the variable camber hydrofoils are four times larger as compared to those of the symmetric hydrofoils. Meanwhile, the camber-making power contributes nearly 25 percent to the total negative area.

Table 5 Total Negative Areas and the Corresponding Average Input Power Values (Actual time in the period is used in computing the area; T of A2 is 4.329 sec. and T of B2 is 2.5 sec.)

Case	Total minus area (Camber making power)	Average input power calculated by Eq. 3.16
A2s	-0.0116	0.00536
A2c	-0.0469 (-0.011213)	0.0217
B2s	-0.01187	0.00950
B2c	-0.0498 (-0.0115429)	0.0399

2) Hydrodynamic power and extracted power

The hydrodynamic power, which is considered at third here, is the power due to the hydrodynamic force and moment acting on the hydrofoil during the given flapping motion at the flapping axis. The hydrodynamic power can be mathematically estimated by calculating all of the hydrodynamic moments at the flapping axis. The hydrodynamic power for a particular flapping motion was acquired before it was reduced by damping, the system mass moment of inertia, and the applied holding torque. The moment at the flapping axis (M_a) due to the lift and drag is determined by the following equation

$$M_a = \frac{1}{2} \rho S l [(V_\infty + l\dot{\psi} \sin \psi)^2 + (l\dot{\psi} \cos \psi)^2] [(C_l \cos \gamma + C_d \sin \gamma) \cos \psi - (C_l \sin \gamma - C_d \cos \gamma) \sin \psi]. \quad (3.17)$$

Then, the total hydrodynamic moment (M_h) at the flapping axis is expressed as follows:

$$M_h(t) = M_a(t) - M_{\frac{c}{4}}(t). \quad (3.18)$$

for the rigid hydrofoil and

$$M_h(t) = M_a(t) - M_{\frac{c}{4}}(t) - Mf_1 - Mf_2. \quad (3.19)$$

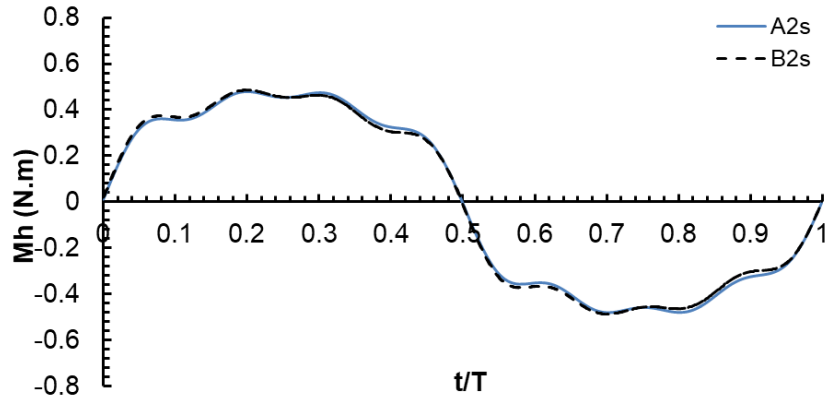
for the variable camber hydrofoil and then

$$P_h(t) = M_h(t)\dot{\psi}(t). \quad (3.20)$$

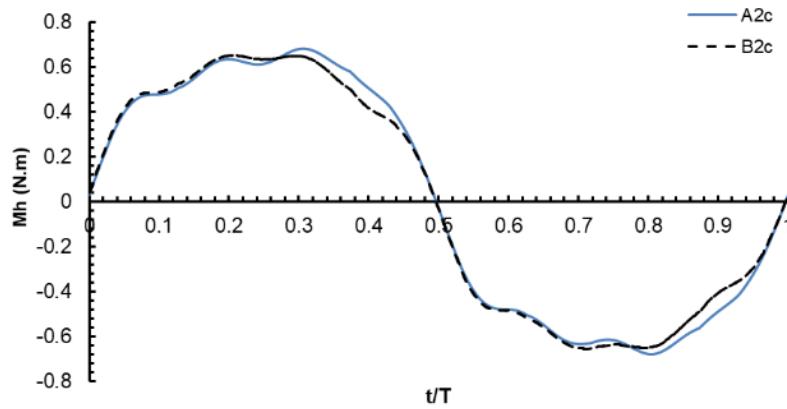
The average hydrodynamic power was obtained using the same method used to determine the average input power:

$$\bar{P}_h = \frac{1}{T} \int_0^T P_h(t) dt. \quad (3.21)$$

First, the hydrodynamic moments and flapping speeds required for calculating the hydrodynamic power values by **Eq. 3.20** are depicted correspondingly in **Figs. 46** and **47**.

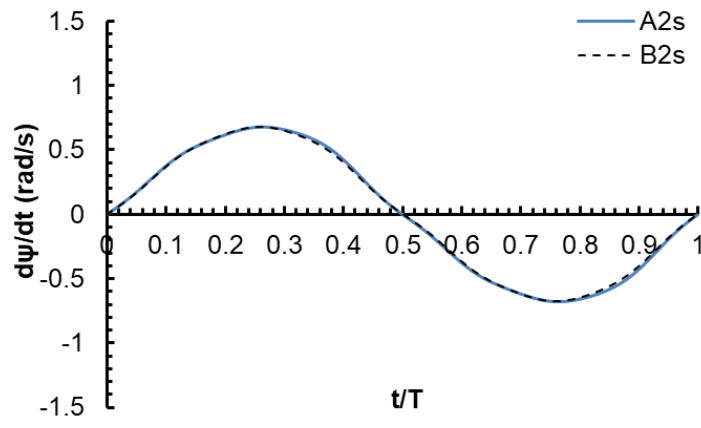


a) Symmetric one

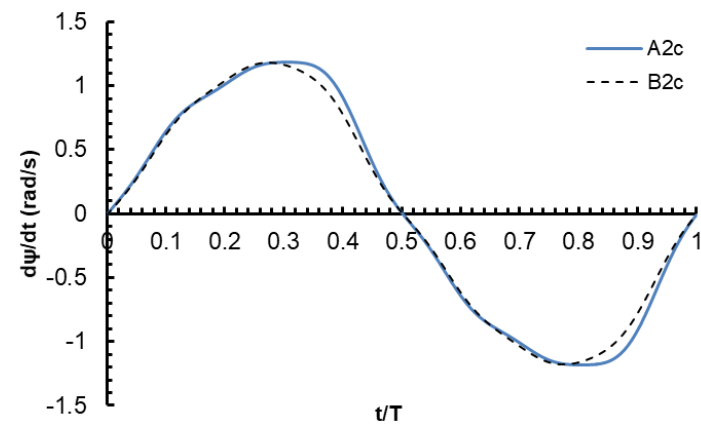


b) Variable camber one

Figure 46 Hydrodynamic moment of symmetric and variable camber ones



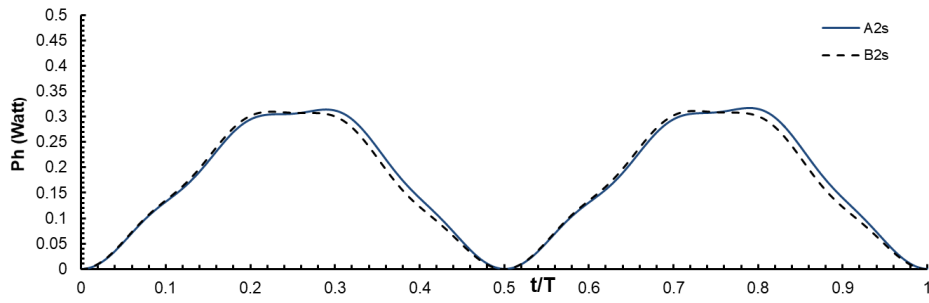
a) Symmetric one



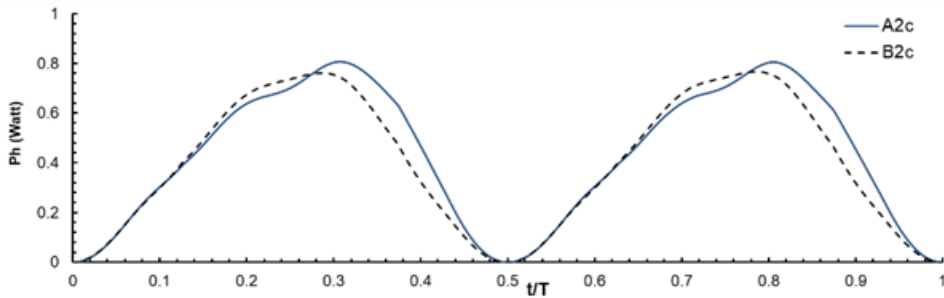
b) Variable camber one

Figure 47 Flapping speed of symmetric and variable camber hydrofoils.

The maximum value in **Fig. 46a** is approximately 0.44 N·m, while the largest value in **Fig. 46b** is approximate 0.7 N·m due to the higher lift of the cambered hydrofoil than that of the symmetric hydrofoil. As shown in **Fig. 47**, the flapping speed graphs are sine-shaped curves with a peak of 0.7 for the symmetric hydrofoil and twice that value for the variable camber hydrofoil because the cambered shape has a smaller frontal area and a higher lift in the identical holding torque during flapping motion than the symmetric shape.



a)



b)

Case	A2s	A2c	B2s	B2c
\bar{P}_h	0.1745	0.4352	0.1709	0.4095

c)

Figure 48 Hydrodynamic power values of (a) symmetric and (b) variable camber hydrofoils.

The table (c) contains the average hydrodynamic power values.

It can be shown from **Fig. 48** that hydrodynamic power values of the variable camber hydrofoil are larger than those of the symmetric hydrofoil, although the shapes of these curves are similar. Subsequently, the average hydrodynamic powers of the variable camber hydrofoils are higher than those of the symmetric hydrofoils, as listed in **Fig. 48(c)**.

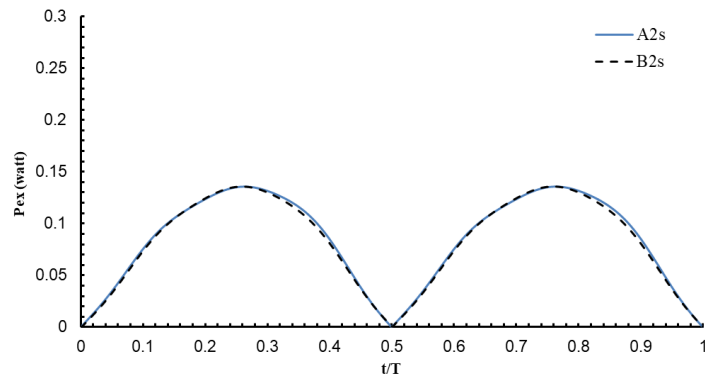
The extracted power, which is considered finally and which is also most important in the power estimation, is determined from the applied holding torque (τ), of which the direction is opposite to that of the angular velocity of the output shaft (Ω). The extracted power is calculated as follows:

$$P_{ex}(t) = |\tau(t)|\Omega(t) = |\tau(t)||\dot{\psi}(t)|. \quad (3.22)$$

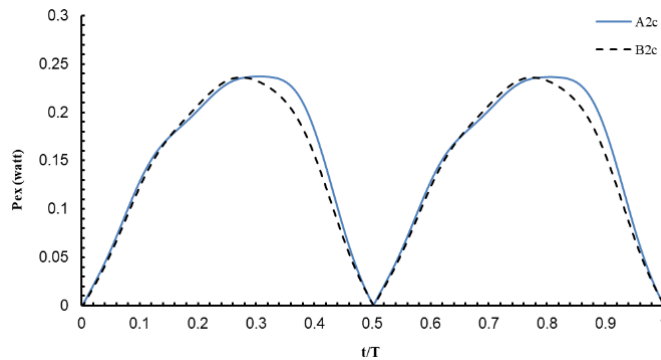
The angular velocity of the output shaft (Ω) can be assumed as the absolute value of the flapping rate ($\dot{\psi}$) of the flapping arm. The average extracted power was obtained using the same method used to determine the average input power;

$$\bar{P}_{ex} = \frac{1}{T} \int_0^T P_{ex}(t) dt. \quad (3.23)$$

The graph in **Fig. 49** depicts the time history of the extracted power as calculated by **Eq. 3.22**.



a)



b)

Case	A2s	A2c	B2s	B2c
\bar{P}_{ex}	0.08456	0.1502	0.0831	0.143

c)

Figure 49 Extracted power values of the (a) symmetric and (b) variable camber ones; the table (c) contains the corresponding average values

3) Mechanical power Efficiency

The efficiency is one of the factors required to quantify the performance of the system. The efficiency is the ratio of the difference of the extracted power and the input power relative to the available power:

$$\eta = \frac{\bar{P}_{ex} - \bar{P}_{in}}{P_a} \quad (3.24)$$

Table 6 System efficiency rates

Case	A2s	A2c	B2s	B2c
η	1.83%	1.9%	3.07%	3.02%

Meanwhile, as listed in **Table 6**, the system efficiency of the variable camber hydrofoil is similar to that of the symmetric hydrofoil when the same holding torque is imposed. This occurs because the extracted power values of the variable camber hydrofoil are approximately double that of the symmetric hydrofoil, whereas the available power values in the cambered case are nearly double those in the symmetric case, while the input power values are fairly small.

3.5.2 Power of scenario 2

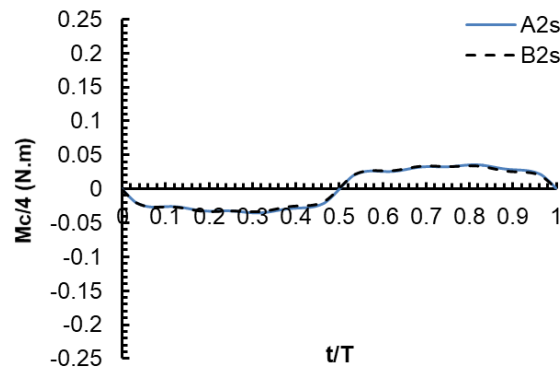
In scenario 2, torque value of 1.25 N·m for variable camber one is used to have response close to the symmetric hydrofoil's response.

1) Available power and Input power

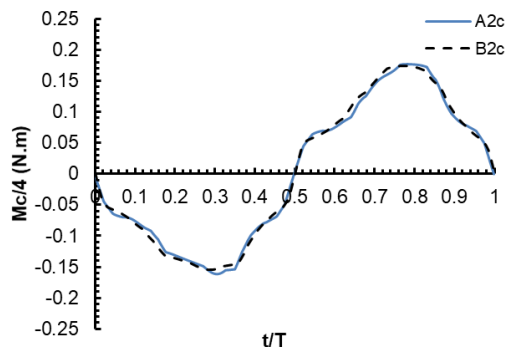
Table 7 Available Power Values for the Symmetric and Cambered Hydrofoils

Case	A2s	A2c	B2s	B2c
ψ_u ($^\circ$)	26.1	26.9	15.06	15.7
ψ_d ($^\circ$)	26.5	25.5	14.89	14.15
d (m)	0.164	0.163	0.096	0.095
P_a (watt)	4.625	4.608 (-0.36%)	2.697	2.688 (-0.34%)

First, the available power values of the variable camber hydrofoils are nearly identical to the available power of the symmetric case as listed in **Table 7** because the flapping responses of the symmetric and variable camber hydrofoils are almost identical. Here, the discrepancies are listed as percentages.



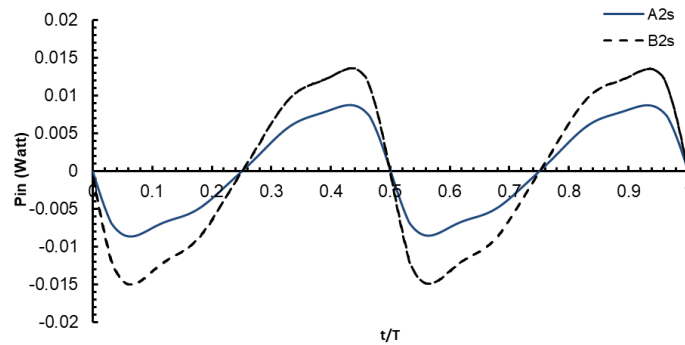
a) Symmetric one



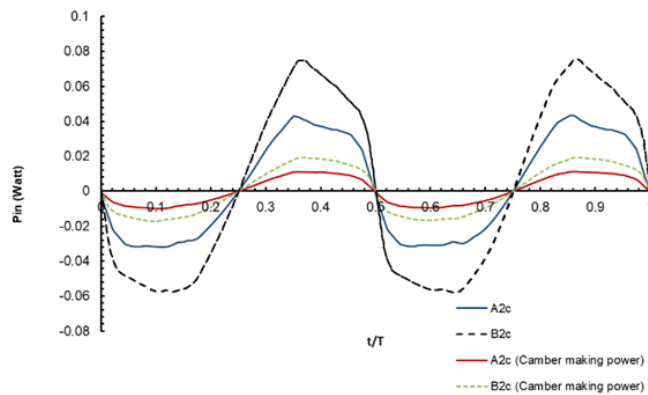
b) Variable camber one.

Figure 50 Pitching moment of symmetric and variable camber hydrofoil

Graphs of pitching moment of one cycle are shown in **Fig. 50**. The peak of variable camber hydrofoil (0.18 N·m) is nearly five times larger than the peak of the symmetric hydrofoil (0.035 N·m), similar to scenario I. Meanwhile, the variable camber hydrofoils have the same pitching speed with the symmetric hydrofoils, similar to scenario I. Subsequently, the input power, a product of the pitching speed and the moment, is depicted in **Fig. 51**, where the positive peaks of the variable camber hydrofoil are nearly five times that of the symmetric hydrofoil, whereas the negative peaks of the variable camber hydrofoil are almost four times those of the symmetric hydrofoil, similar to scenario I. In the input power curves of the variable camber hydrofoil, the camber-making power outcomes are included.



a) Symmetric one



b) Variable camber one

Figure 51 Input power values of the (a) symmetric and (b) variable camber hydrofoils

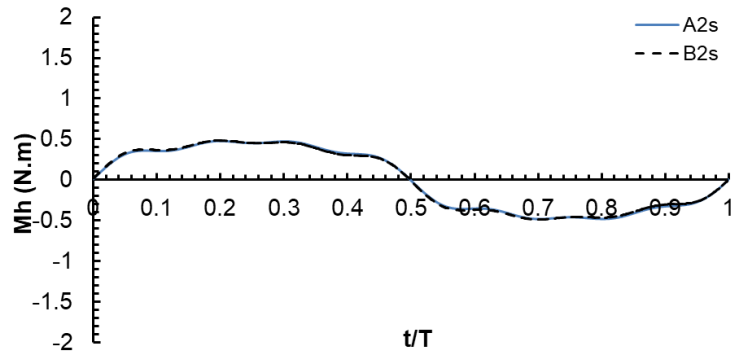
The total negative areas are listed in **Table 8**. The areas of the variable camber hydrofoils are five to six times larger as compared to those of the symmetric hydrofoils, but the values are fairly small as compared to the available power values. The camber-making power is less than 29% as compared to the total negative area, similar to scenario I.

Table 8 Total Negative Areas and the Corresponding Average Input Power Values

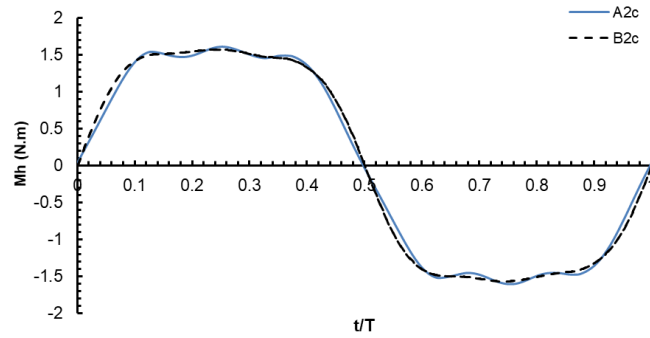
Case	Total negative area (Camber-making power)	Average input power calculated by Eq. 3.16
A2s	-0.0116	0.00536
A2c	-0.0517 (-0.014631)	0.0239
B2s	-0.01187	0.00950
B2c	-0.06147 (-0.01504)	0.0492

2) Hydrodynamic power and extracted power

The hydrodynamic moments and flapping speeds required for calculating the hydrodynamic power values by **Eq. 3.20** are depicted correspondingly in **Figs. 52** and **53**.

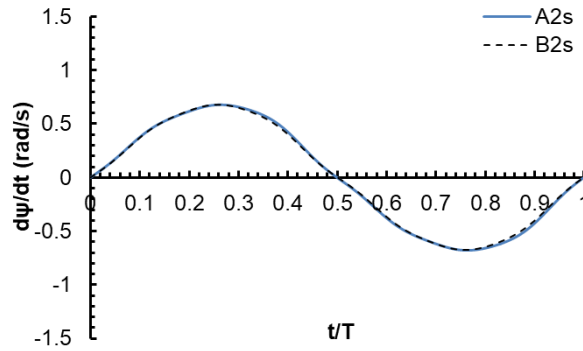


a)

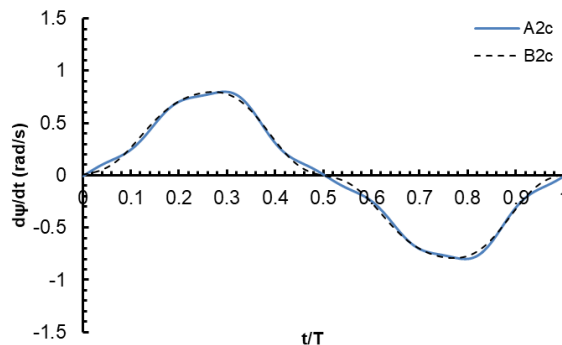


b)

Figure 52 Hydrodynamic moment of the (a) symmetric and (b) variable camber hydrofoils



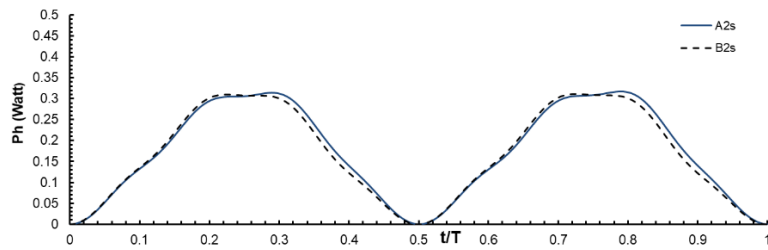
a)



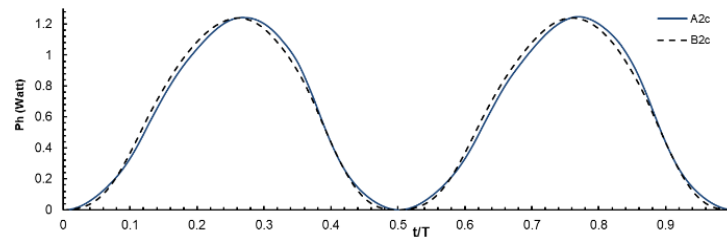
b)

Figure 53 Flapping speed of the (a) symmetric and (b) variable camber hydrofoils

The maximum value in **Fig. 52a** is close to 0.5 N·m, while the largest value in **Fig. 52b** is approximately 1.6 N·m. The flapping speed graphs of **Fig. 53** are sine-shaped curves with a peak of 0.7 rad/s for the symmetric hydrofoil and a peak of 0.8 rad/s for the variable camber hydrofoil. The hydrodynamic power values, in each case a product of the flapping moment and the speed, are depicted in **Fig. 54**.



a)



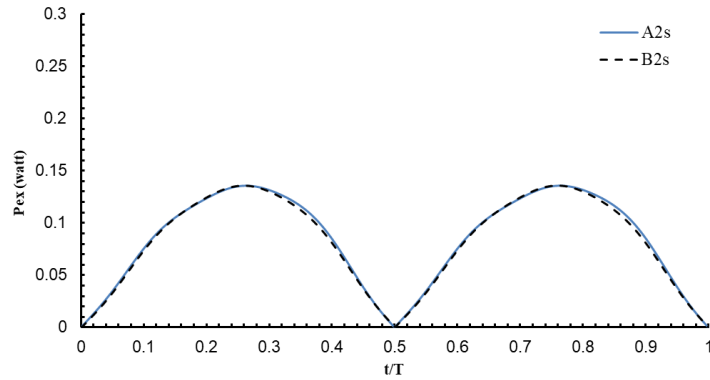
b)

Case	A2s	A2c	B2s	B2c
\bar{P}_h	0.1745	0.611	0.1709	0.6115

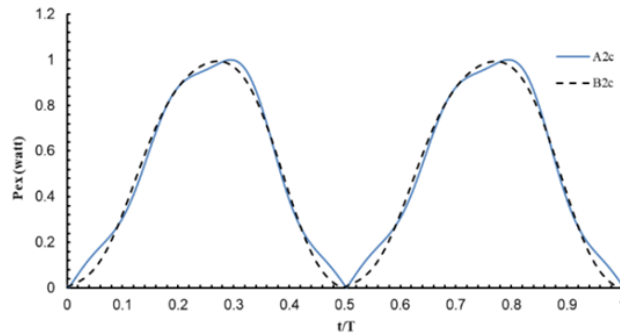
c)

Figure 54 Hydrodynamic power values of the (a) symmetric and (b) variable camber hydrofoils; the table (c) contains the corresponding average values.

The graph in **Fig. 55** depicts the time history of the extracted power as calculated by **Eq. 3.22**.



a)



b)

Case	A2s	A2c	B2s	B2c
\bar{P}_{ex}	0.08456	0.505	0.0831	0.506

c)

Figure 55 Extracted power values of the symmetric and variable camber hydrofoils; the table (c) contains the corresponding average values.

As shown in **Fig. 55**, the extracted power values of the symmetric hydrofoil are approximately 1/5 to 1/6 those of the variable camber hydrofoil mainly due to the smaller holding torque.

3) Mechanical power efficiency

Table 9 presents the mechanical power efficiency rates of the symmetric and variable camber hydrofoils in percentage term.

Table 9 System efficiency rates

Case	A2s	A2c	B2s	B2c
η	1.83%	10.96%	3.07%	18.82%

As shown in **Fig. 55**, the variable camber hydrofoil, which uses 1.25 N·m instead of 0.2 N·m, obtains greater power extraction. The average input power is quite small, which results in an efficiency increase by the variable camber hydrofoil by more than five times as compared to that of the symmetric hydrofoil.

3.6 Sub conclusion

In this section, the power outputs of variable camber and symmetric hydrofoils are compared using a mathematical dynamic model assuming their use in flapping hydrofoil turbines (FHT). With the same holding torque, the efficiency rates between the symmetric and variable camber hydrofoils are similar despite the fact that the hydrodynamic power of the variable camber hydrofoil is more than twice that of the symmetric hydrofoil. This occurs because the extracted power values in the variable camber case are nearly two times those of the symmetric case, whereas the available power of the variable camber hydrofoil also is nearly two times greater than that of the symmetric hydrofoil and the input powers of both hydrofoils are quite low as compared to the extracted power.

As a different approach, when the response of the variable camber hydrofoil becomes close to that of the symmetric hydrofoil through an increase in the holding torque, the efficiency of the variable camber hydrofoil is found to be much higher than that of the symmetric hydrofoil. The similar response values lead to similar available power outcomes,

but the extracted power of the variable camber hydrofoil is six times greater than that of the symmetric hydrofoil, while the input power values of both hydrofoils are also low as compared to the extracted power. Subsequently, increasing the extracted power of the variable camber hydrofoil by six times led to more than five times higher system efficiency compared to that by the symmetric hydrofoil.

Eventually, through this power analysis, it was found that the camber-making mechanism can be utilized as an effective scheme with which to improve the power extraction performance of the FHT despite the increased complexity. Due to that the developed dynamic model have limitation for maximum pitch angle to 14 degrees, in order to analyze the performance of FHT in actual pitch angle over 60 degrees, the model is needed to be modified later.

Chapter 4 Parametric study on power performance

4.1 Computational Fluid Dynamics tool

The Matlab code for the dynamic model has limitation of the maximum pitch angle to 14 degree while the actual pitch angle utilized for power extraction is over 60 degree. Hence, computation fluid dynamics (CFD) tool is adopted instead. A commercial CFD tool such as Fluent is reliable but pricey. Instead of it, in this work, the in-house code, which is a parallelized multi- block-structural Navier-Stroke solver named Kflow [90] is adopted; it was validated and utilized in several FHT related researches [14, 91]. In order to deal with the relative motion between airfoil mesh and domain mesh for flapping hydrofoil turbine, the multigrid method named Chimera [92] is used.

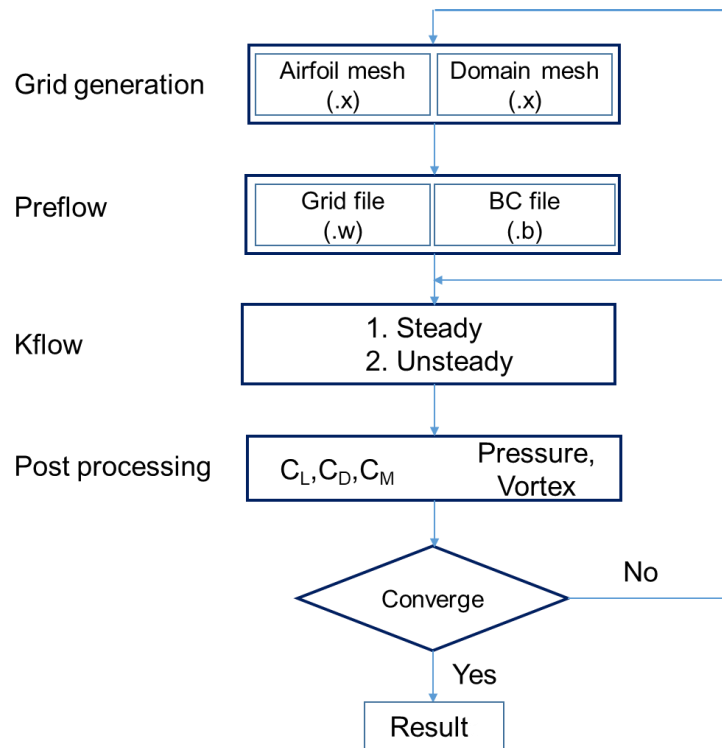


Figure 56 CFD process

In grid generation step in Fig. 56, chimera meshes are generated. Detail of the chimera grid system for symmetric hydrofoil is shown in Fig. 57. The square background domain

subfigure (1) has size 48c in x direction and 48c in y direction, stands for the fluid. The core mesh at the center is finer than that at the boundary. Subfigure (2) shows the location of the body-fitted mesh in the grid system. This mesh stands for the hydrofoil. That composition comprises of body fitted C type mesh cover the boundary of the hydrofoil and the background mesh with H-type. The body-fitted mesh has the first layer 1E-4 and orthogonal-ensure along the chord wise direction of the hydrofoil. Subfigures (3) and (4) are the zoom-in views of the leading edge and the trailing edge. In order to capture the vortex, the body fitted mesh are clustered near the leading edges and trailing edges. The output file of this process must have extension .x(formatted PLOT3D). PLOT3D format is a standardized format for storing grid and results data, was created by Pieter Buning at NASA Ames Research Center in 1982 [93]. It is capable of storing the structured grid. In Preflow [94], the no "slip" boundary and Riemann invariant are applied for the profile of investigated airfoil and far field boundary condition [95]. Outputs are the grid file (.w) and Boundary condition files (.b). The boundary condition can be divided into real boundary, block boundary and parallel boundary.

In terms of turbulent model, the $k-\omega$ WD+ mode [95] adopted in this study, which is less sensitive to normal wall length, performs better agreement compare to observation data when used in cases of weakly nonlinear eddy viscosity, and converges more swiftly and therefore lower the computing cost. Steady – state results are treated as initial condition for an unsteady analysis [95].

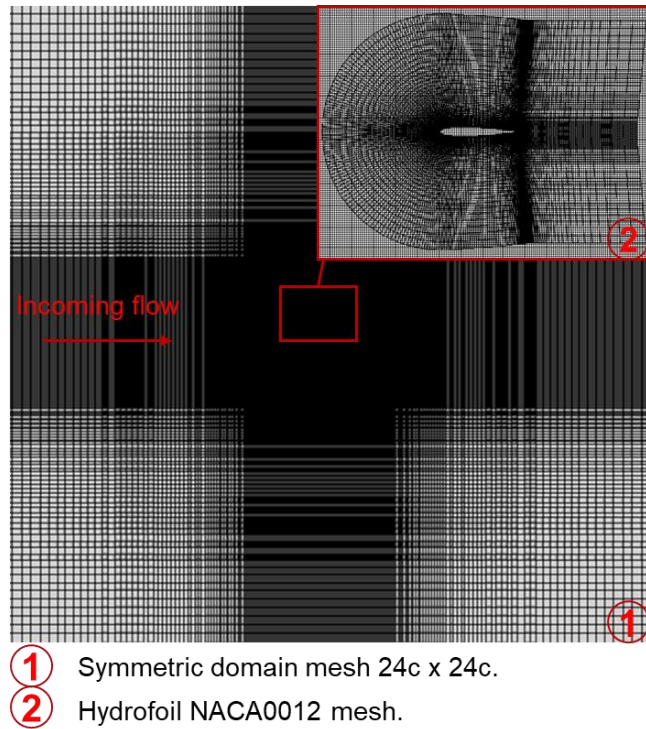


Figure 57 Chimera mesh with symmetric NACA0012 by 463×105

The study of convergence was conducted before moving to the parametric study. The study consider two aspect of convergence: grid density convergence and numerical convergence. At first, three sizes of the body-fitted mesh (463×105 , 515×105 , 677×105) considering first distance from the wall $1E-4$ and increase of grid number in x direction are used in simulation with the iteration of 500 and number of time step of 400. The results are almost identical despite that the density of body-fitted mesh are increased (maximum relative error of C_L and C_D peaks between 463×105 and 677×105 are less than 0.2%). Next, coarse mesh 463×105 picked to simulation with 300, 400 and 500 time step in one cycle are used with 400, 500 and 600 iterations, the results are almost similar each other.

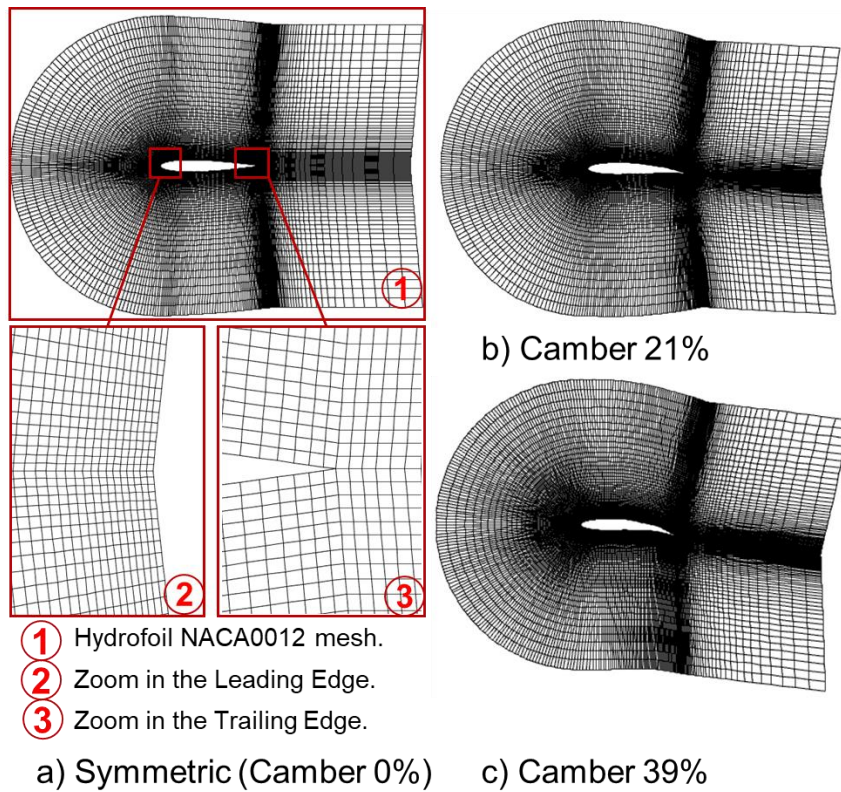


Figure 58 Profiles of symmetric (camber 0%), camber 21% (Top right) and camber 39% (Bottom right)

Three sectioned shape hydrofoils, which were implemented in a variable camber related research [81], are chosen by varying the camber amplitude as depicted as **Fig. 58**; The camber amplitude for NACA0012, NACA0012_21, and NACA0012_39 are 0 percent, 21 percent (smaller by 9 than 30) and 39 percent (larger by 9 than 30), respectively. The symmetric and cambered NACA0012 hydrofoil has pitch pivot at 25% chord location.

The grid systems of the two cambered hydrofoils in **Fig. 58b)** and **Fig. 58c)** are generated with similar mesh quality such as orthogonality, size etc. with that of the symmetric hydrofoil.

4.1.1 Validation of the in-house code

1) Benchmarking problem 1

a) Problem definition including Kinematics

As the first benchmark, the result of the simulation is compared with that of Kinsey [96]. The location of pitch axis sets at one-third of the chord length of NACA0015 as depicted in **Fig. 59**. Pitch motion of the hydrofoil has maximum angle value of 75° , the phase between heaving motion and pitching motion is 90° . The arm length are twice the length of the hydrofoil. The Reynolds number is 500,000, heaving amplitude h_0 is same with chord length (thus $h_0/c = 1$), and reduced frequency f^* is 0.14.

Kinematic is described as a sinusoidal function of time:

$$h(t) = h_0 \sin(\omega t + \varphi) \text{ and } \theta(t) = \theta_0 \sin(\omega t). \quad (4.1)$$

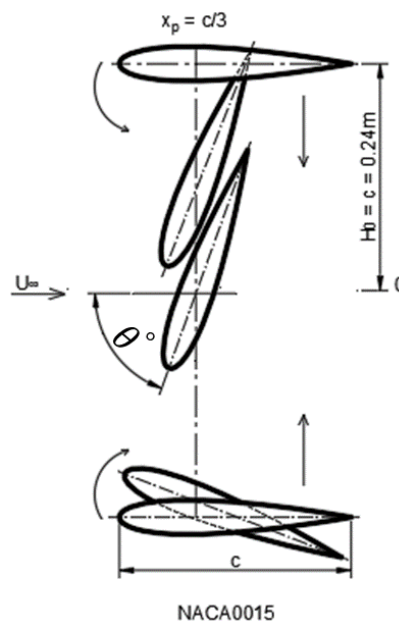


Figure 59 Heave motion amplitude $H_0 = c = 0.24\text{ m}$, Pitch amplitude $\theta = 75^\circ$ of NACA0015, $f^* = 0.15$ at Reynolds number 500,000.

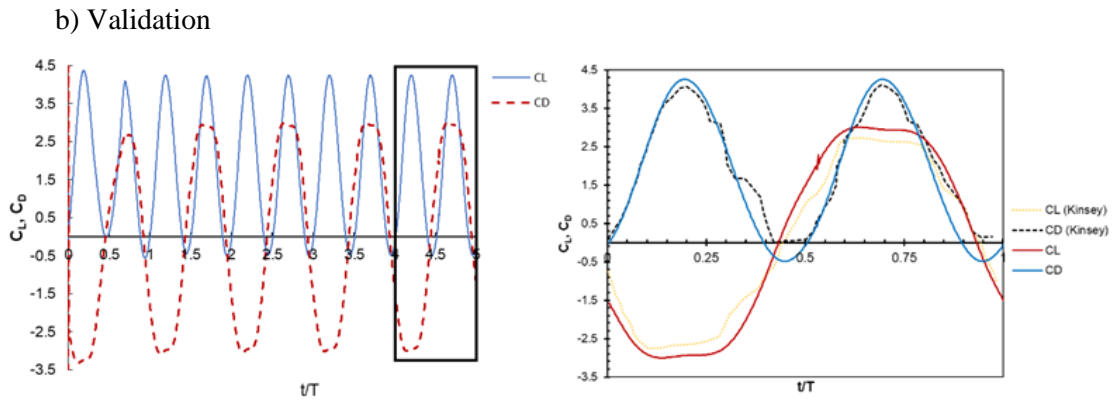


Figure 60 Graph of Lift, Drag force for full 5 cycles reduced frequency $f^* = 0.14$, pitch angle $\theta = 75^\circ$ (Left) Comparison Lift, drag 5th cycle with Kinsey data (Right)

The simulation is conducted by increasing the density of the body-fitted mesh while keeping the domain mesh 396 grid point in X direction and 396 grid point in Y direction totally 156,816 quadrilateral cells. The left graph of **Fig. 60** shows the full outcome of benchmark after 5 cycles. It can be shown that the hydrodynamics become convergence well from 3rd cycle. The peak drags of third, fourth, and fifth cycle are 2.98, 2.99, and 3.00 respectively. Force curves on the right are the 5th cycle compared with those of Kinsey research [96]. The comparison shows that current results with the body-fitted mesh 520×74 are close to those of Kinsey. The shape of drag curve in two half cycles is almost identical while the lift force curve also repeats but in difference sign.

2) Benchmarking problem 2

a) Problem definition including Kinematics

The second benchmark is also with Kinsey et al. [27]. Compare to the first benchmark, this benchmark has the same Reynolds number 500,000, pitch–heave configuration. However, the heaving amplitude is one and half time bigger with $1.5c$ ($h_0/c = 1.5$), the bigger pitch angle with $\theta_0 = 85^\circ$. Therefore, this benchmark is taken to check the stability of the in-house solver when varying the reduced frequency and pitch angle. Hydrofoil profile NACA0015 is used in

this validation. 90° is the phase angle between heaving motion and pitching motion. Reduced frequency $f^* = 0.16$.

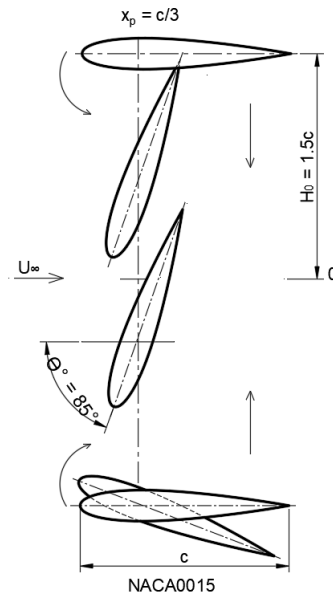


Figure 61 NACA0015 with $H_0/c = 1.5$, maximum pitch angle $\theta = 85^\circ$, $f^* = 0.16$ at Reynolds number 500,000.

b) Validation

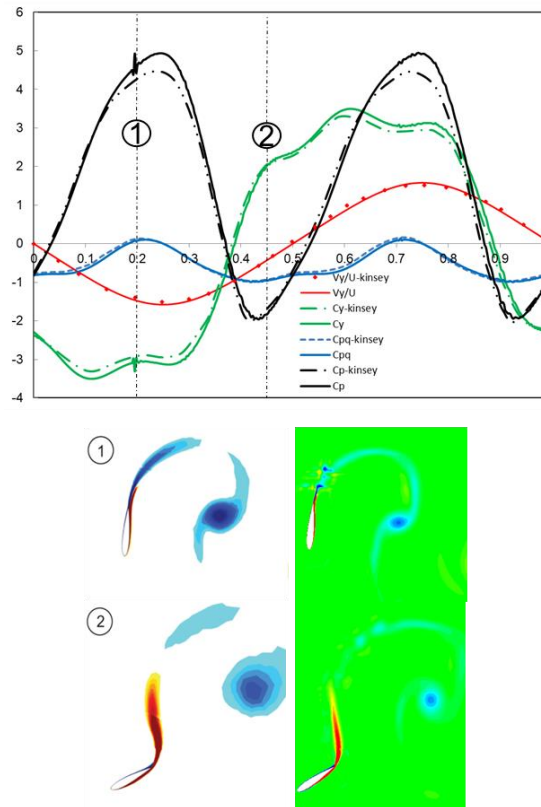


Figure 62 Benchmark Kinsey (Top) Coefficient comparison: Instantaneous vertical force C_y , normalized heaving velocity V_y , pitching contribution to the power C_{pq} , and total power coefficient C_p (Bottom) flow pattern comparison (vorticity fields at $t/T \frac{1}{4} 0.25$ and 0.45 (blue: CW vorticity, red: CCW vorticity)

The result from the in-house code show the similar the force coefficient as well as the power coefficient as comparing each pair of curves in **Fig. 62**. Another comparison about flow characteristics, the vortex contour of Fluent and the in-house code is similar in trailing edge vortices and the shedding.

4.2 Performance analysis

4.2.1 Kinematics of right-swing configuration

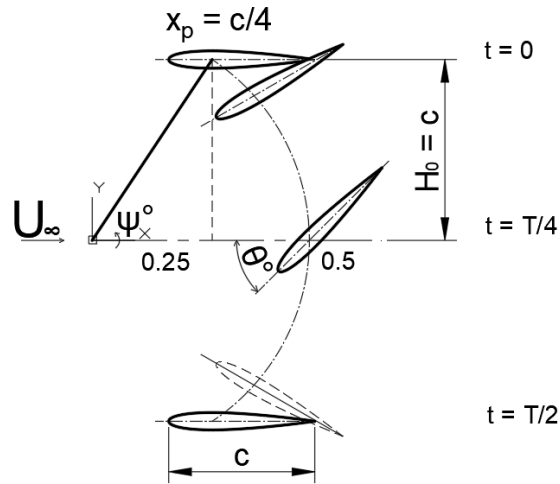


Figure 63 NACA0012 Trajectory x_p (centerline) of right swing configuration.

In a swing configuration, kinematics of hydrofoil constrained by the flapping arm due to that the pitch axis of hydrofoil attached with one end of the arm. As the arm flaps up and down, the hydrofoil moves up and down. In right swing configuration, hydrofoil turns around the pitch axis and it flaps at the arm axis located upstream as depicted in **Fig. 63**.

Typically, the flapping of a hydrofoil for harnessing the energy comprising of two simultaneous motions which include the flapping motion of the arm $\psi(t)$ and the pitching motion $\theta(t)$.

The pitch motion of the hydrofoil is described as:

$$\theta(t) = \theta_0 \sin(\omega t). \quad (4.2)$$

And flapping motion function is

$$\psi(t) = \psi_0 \sin(\omega t + \varphi). \quad (4.3)$$

The phase difference φ between the pitching and flapping motion is a constant value 90 degrees.

The instantaneous positions of the pitch axis are then given as follow:

$$x(t) = x_p + [L\cos\{\psi(t)\} - L\cos(\psi_0)] \text{ and}$$

$$y(t) = L\sin\{\psi(t)\}. \quad (4.4)$$

Velocity in X and Y direction are

$$\dot{x}(t) = -L\dot{\psi}(t)\sin\{\psi(t)\} \text{ and}$$

$$\dot{y}(t) = L\dot{\psi}(t)\cos\{\psi(t)\}. \quad (4.5)$$

Effective angle of attack is

$$\alpha(t) = \tan^{-1} \left[\frac{-\dot{y}(t)}{U_\infty + \dot{x}(t)} \right] + \theta(t). \quad (4.6)$$

In our configuration, the flapping arm length is two times compare to hydrofoil length. Flapping amplitude is $1 \times c$. Maximum angle of flapping arm is about 30 degrees. The pitching amplitude for the following parametric study vary from 50 degree to 80 degree. The phase between flapping motion and pitching motion is 90 degree. The range of reduced frequency for parametric study is from 0.08 to 0.14. The free stream velocity is 2.6 m/s. The turbulent Reynolds number (RE) based on free stream velocity and 600 mm chord length $\left(\frac{U_\infty c}{\nu}\right)$ is 1,745,817, which is used in a previous study about parametric analysis of the commercially viable RE range [95].

4.2.2 Forces and flow characteristics

Here, the role of the camber for the hydrodynamic forces of the right swing flapping turbine will be explored with the camber from zero percent (symmetric shape) to maximum thirty nine percent varied. Reduced frequency $f^* = 0.1$ and pitch angle $\theta_0 = 60^\circ$ are chosen for this analysis.

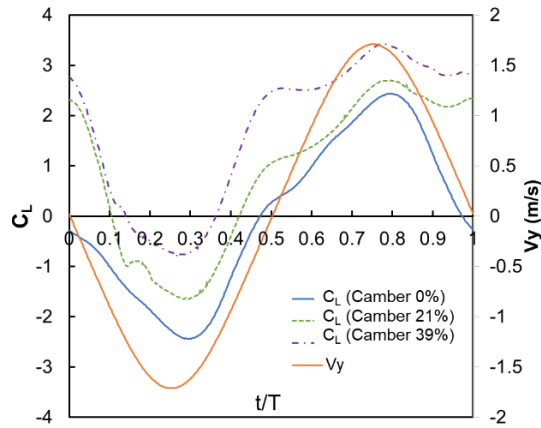


Figure 64 C_L curves and Velocity of camber 0%, camber 21% and camber 39%.

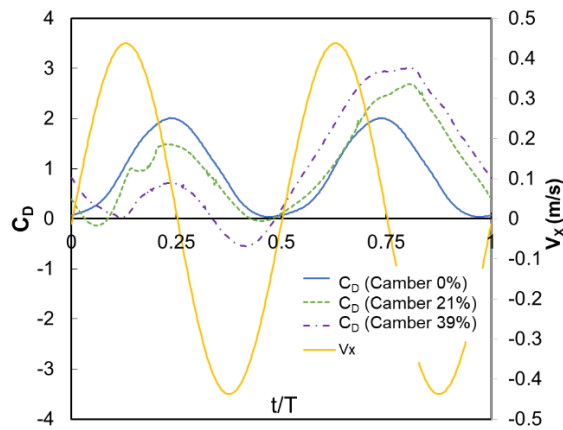


Figure 65 C_D curves and velocity of camber 0%, camber 21% and camber 39%

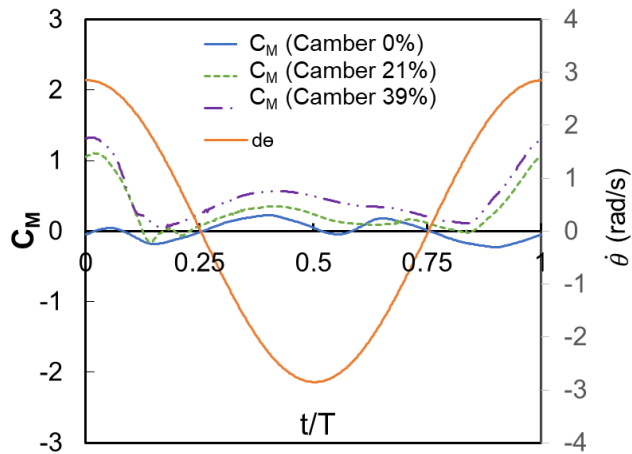


Figure 66 C_M curves and velocity of camber 0%, camber 21% and camber 39%

The C_L , C_D , C_M and velocity versus t/T of the symmetric hydrofoil and various camber hydrofoils are depicted in **Fig. 64** to **66** above.

For the symmetric hydrofoil, C_L and C_M are identical in amplitude (2.44 for C_L) and but with opposite sign between the downstroke and the upstroke. C_D of the upstroke repeats in the downstroke with the peak of around 2.

For the camber 21% hydrofoil in trajectory of **Fig. 64** and **65**, the C_L and C_D amplitudes during downstroke are smaller than those of symmetric hydrofoil. In contrast, C_L and C_D amplitudes during upstroke become bigger than those of symmetric case. In addition, C_M also increase in magnitude over the period and becomes considerably larger at top position due to the cambered shape, which will be explained later.

For the camber 39% hydrofoil, the same phenomenon repeats in C_L , C_D and C_M curves with their amplitudes amplified.

Next, pressure and vorticity contours at series of typical time steps of $t/T = 0.0, 0.2, 0.4, 0.6$ and 0.8 are provided in **Fig. 67** and **68** to show the change in flow characteristic while the hydrofoils are moving in the cycle. These figures are arranged in order of time (top to bottom), and in order of increasing camber (left to right).

At $t/T = 0.0$, at the initial position of flapping cycle, negative pressure zone is observed on upper surface of symmetric, camber 21% and camber 39%. The blue zone moves closer to the trailing edge as camber amplitude increases. The size of the blue zone is getting bigger as well.

At $t/T = 0.2$ and 0.4 during downstroke, sizes of blue and yellow zones decrease, subsequently the pressure difference becomes smaller due to negative camber as the camber amplitude increases.

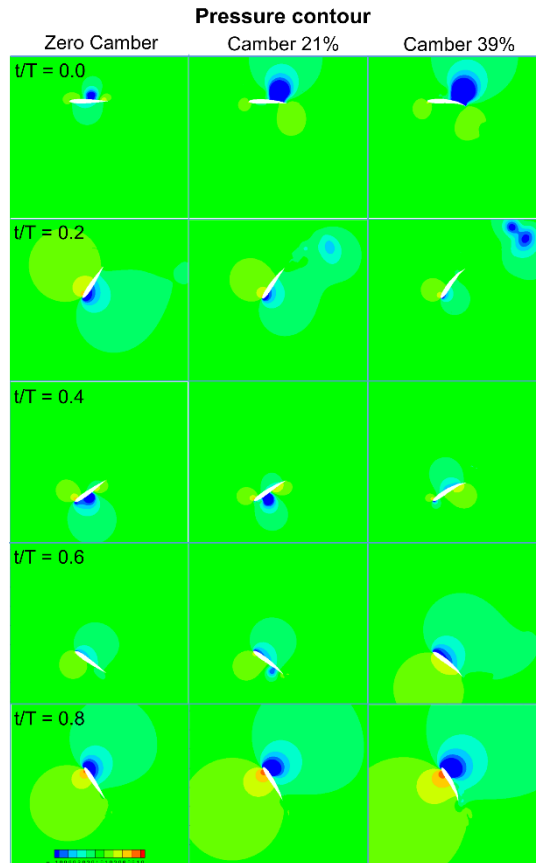


Figure 67 Pressure contour of ($f^* = 0.1$, $\theta = 60^\circ$) at $t/T = 0.0, 0.2, 0.4, 0.6$ and 0.8 .

At $t/T = 0.6$ and 0.8 during upstroke, yellow and blue pressure zones become larger subsequently make high pressure difference zone bigger due to the positive camber as the camber amplitude increases.

The discrepancies in vortex of flow pattern owing to the cambered shapes can lead to the difference in pressure pattern and then instantaneous C_L , C_D and C_M previously presented.

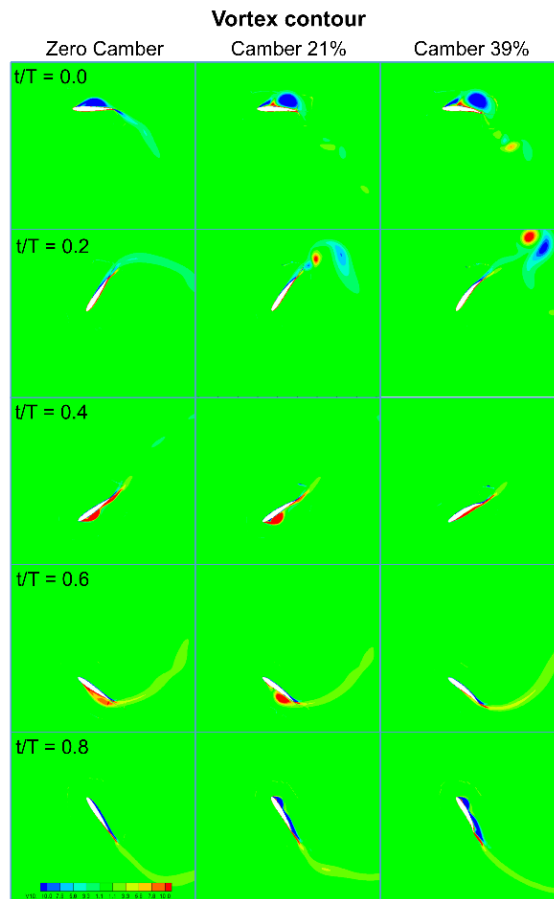


Figure 68 Vortex contour of ($f^* = 0.1$, $\theta = 60^\circ$) at $t/T = 0.0, 0.2, 0.4, 0.6$ and 0.8 (blue: clockwise vortex; red: counterclockwise vortex).

As shown **Fig. 68**, during down stroke, vorticities at larger negative camber develop, and shed faster, then cause smaller lift at $t/T = 0.2$ and 0.4 . The larger C_M at $t/T = 0$ at larger camber in **Fig. 66** is caused due to that vortex is located nearer to trailing edge.

At $t/T = 0.6$ and 0.8 during upstroke, vorticity in blue color over upper surface become stronger subsequently causes larger blue zone in **Fig. 67** as camber amplitude increases. Consequently, different vortex activities caused by positive and negative cambers during one cycle make the forces of **Fig. 64-66** different as expected.

4.3 Parametric analysis

As significant parameters related to the power performance of the flapping foil, there are Reynolds number, reduced frequency, pitch angle and the flapping angle. Meanwhile, as

conducted in the previous research [95], the Reynold number and flapping angle are fixed and the others are chosen as the parameters. It is also reported that the amount of energy that the flapping foil can take from the free stream is determined mainly by the reduced frequency [96].

In previous research [95], the range of the reduced frequency $f^*(0.02 - 0.2)$ with interval 0.02 and the range of pitch angle ($10^\circ - 90^\circ$) are quite large. This could provide the full view about their effect. However, the result show that reduced frequency from (0.02 - 0.2) and pitch angle ($10^\circ - 50^\circ$) represents propulsion area. Thus, the interesting operating zones here were narrow-downed to a range of values for reduced frequency (0.08 - 0.14), pitching angle ($50^\circ - 80^\circ$) with flapping amplitude h_0 fixed by $1c$ and RE fixed by $1E7$. Namely, 16 sets in **Table 10** are used for the following parametric analysis.

Table 10 Parameter for 16 cases of parametric study

Case	Reduce frequency f^*	Pitch angle Amplitude θ_0 (deg)
1	0.08	50°
2	0.08	60°
3	0.08	70°
4	0.08	80°
5	0.1	50°
6	0.1	60°
7	0.1	70°
8	0.1	80°
9	0.12	50°
10	0.12	60°
11	0.12	70°
12	0.12	80°
13	0.14	50°
14	0.14	60°
15	0.14	70°
16	0.14	80°

For the Right - Swing type configuration, the total power is the sum of three power component vertical power, horizontal power and pitching power.

The lift force or vertical force as the product of C_y is

$$F_y(t) = \frac{1}{2} C_y \rho b c U_\infty^3. \text{ (kN)} \quad (4.7)$$

The drag force or the horizontal force as the product of C_x is

$$F_x(t) = \frac{1}{2} C_x \rho b c U_\infty^3. \text{ (kN)} \quad (4.8)$$

The moment calculate at the pitch axis is

$$M(t) = \frac{1}{2} C_m \rho b c^2 U_\infty^3. \text{ (Nm)} \quad (4.9)$$

Total power of three components is then

$$P(t) = F_x(t) + F_y(t) + M(t). \quad (4.10)$$

The time-averaged valued of the total power is

$$\bar{P} = \frac{1}{T} \int_0^T [(F_x(t)\dot{x}(t)) + (F_y(t)\dot{y}(t)) + (M_z(t)\dot{\theta}(t))] dt. \quad (4.11)$$

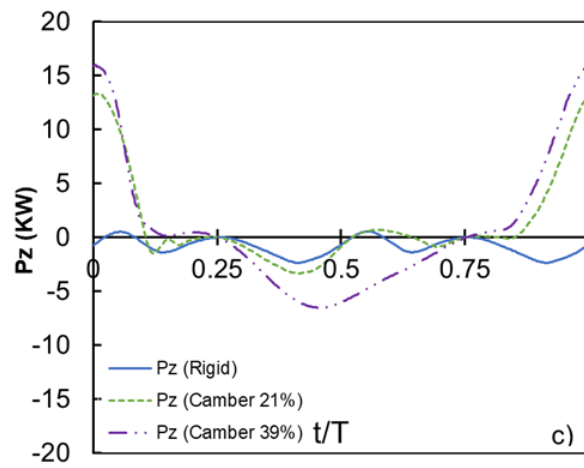
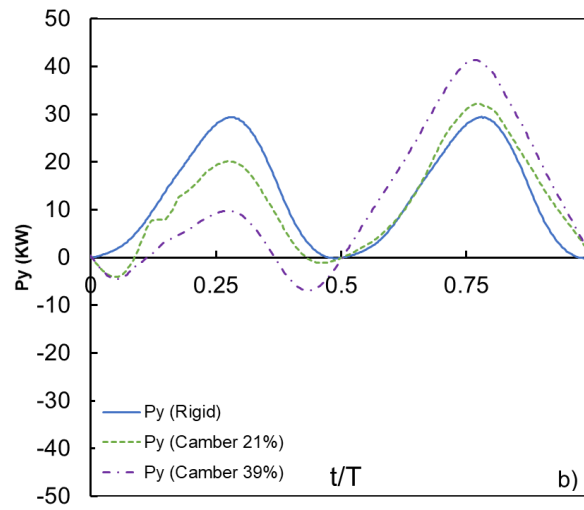
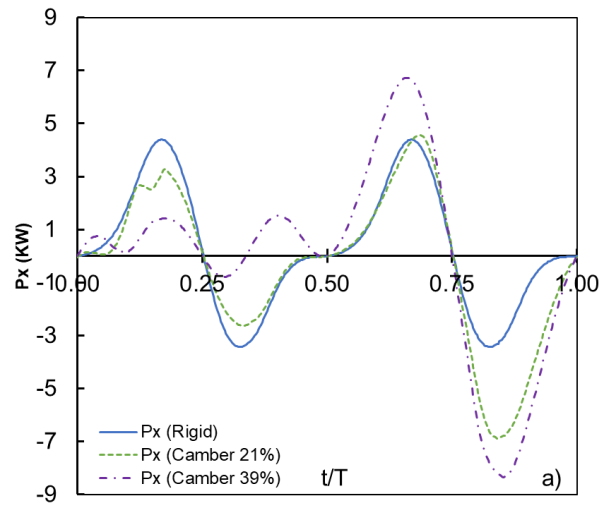
Efficient of half cycle is defined as average power divide the available power as follows:

$$\eta = \frac{\bar{P}}{P_a}. \quad (4.12)$$

Available power from the flow passing through the frontal area swept by the foil:

$$P_a = 0.5 \rho U_\infty^3 b d. \quad (4.13)$$

Fig. 69 depicted the power graphs of case 6 in **Table 10** for symmetric, camber 21% and camber 39% amplitude. Here, P_x , P_y , P_z and P_M represent the power in x axis, y axis, pitching axis and total power, respectively. P_x is the product of drag of **Fig. 65** and V_x , P_y is the product of lift of **Fig. 64** and V_y and P_z is the product of moment of **Fig. 66** and $\dot{\theta}$.



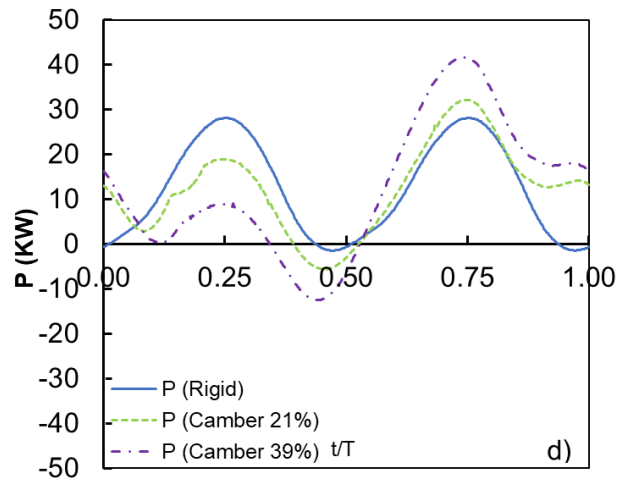
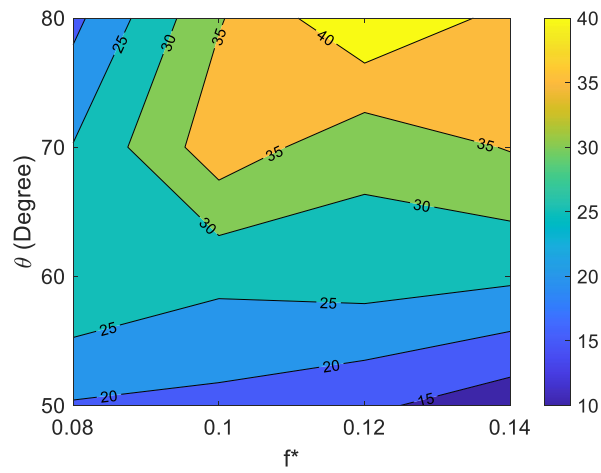


Figure 69 Power graphs of ($f^* = 0.1, \theta = 60^\circ$)

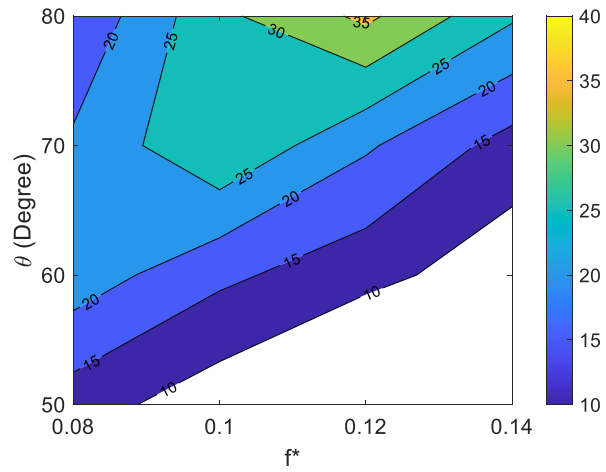
For the symmetric hydrofoil, the P_x peak value and trend of upstroke and downstroke are almost identical. For the camber 21% and 39% amplitudes, the P_x peak of downstroke becomes smaller and becomes bigger in upstroke due to negative and positive camber, respectively. P_y shows similar trend to P_x . Interestingly, P_z around at $t/T = 0$ contributes considerably to total power in case of cambered hydrofoils. The P_y graph and P graph are congruent except near $t/T = 0$ because the lift is main factor for the contribution.

The further analysis of camber effect on the energy extraction performance will be conducted to obtain parametric maps for the chosen sets.

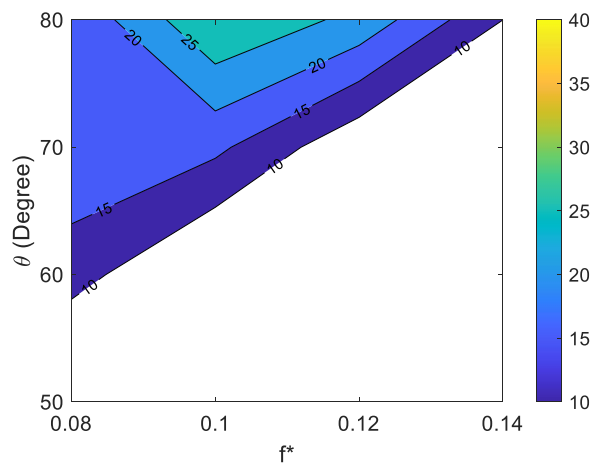
4.3.1 Isocontour map of camber variation for first half of a cycle, $t/T = 0 \sim 0.5$



a)



b)



c)

Figure 70 Power efficiency maps of camber 0%, camber 21% and camber 39% for first half of cycle

In the symmetric NACA0012 case of **Fig. 70a**, the highest efficiency is up to 40% and high efficiency zone of (35% - 40%) are achieved at $f^*(0.1-0.14)$ and θ° (70 - 80). Meanwhile, with negative camber 21%, even propulsion regime (white region) is appeared. The highest efficiency zone (30 - 35%) is located with reduced frequency (0.1 - 0.14) and pitch angle (70 - 80). With negative camber 39%, the propulsion regime becomes bigger than the power extraction regime. Maximum power efficiency is only 25%.

Consequently, in downstroke with negative camber, the peak efficiency is reduced from symmetric to camber 21% and camber 39% amplitudes opposite to in upstroke with positive camber.

4.3.2 Isocontour map of camber variation for second half of a cycle, $t/T = 0.5 \sim 1$

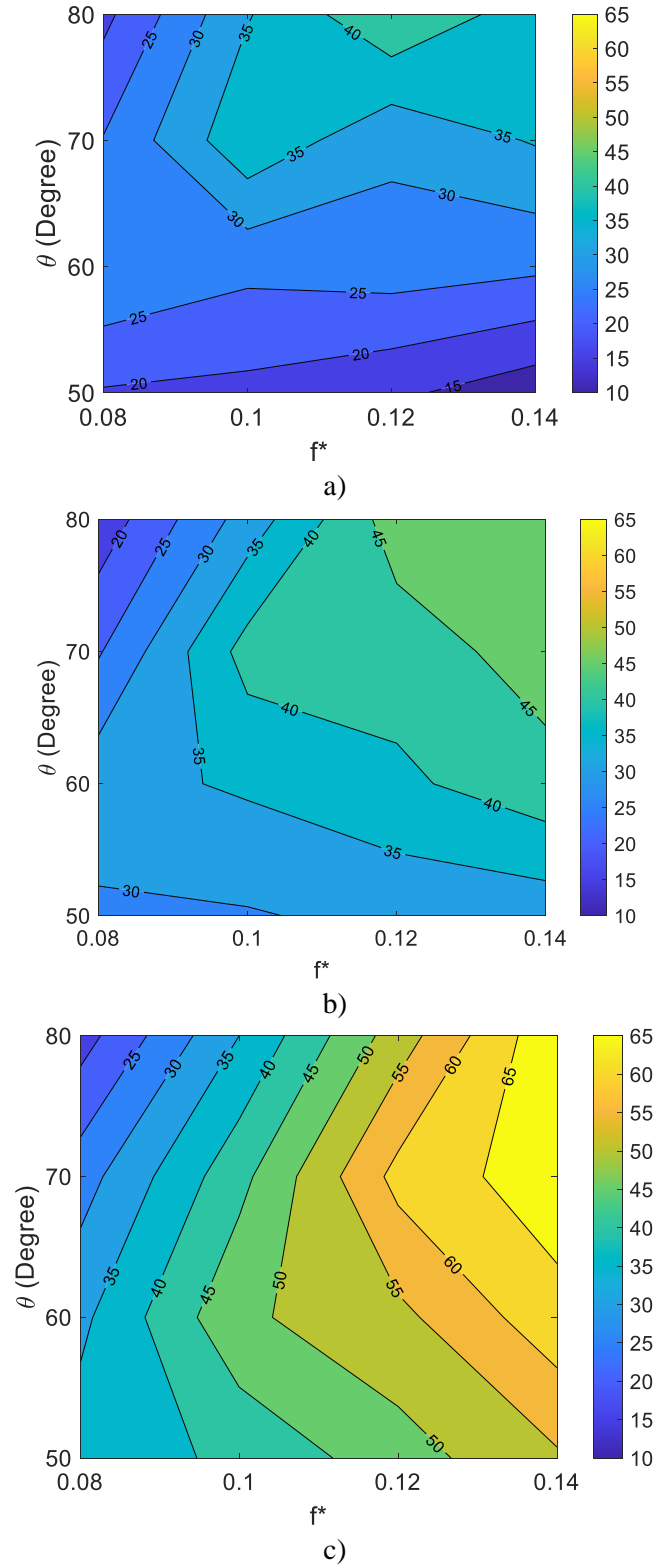
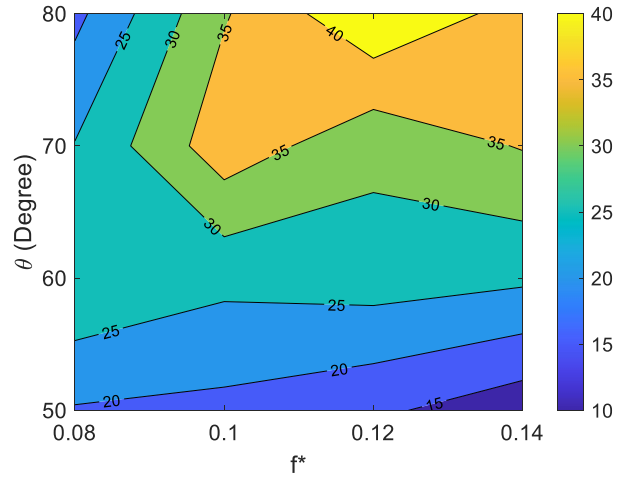


Figure 71 Power efficiency maps of camber 0%, camber 21%, and camber 39% for second half of a cycle.

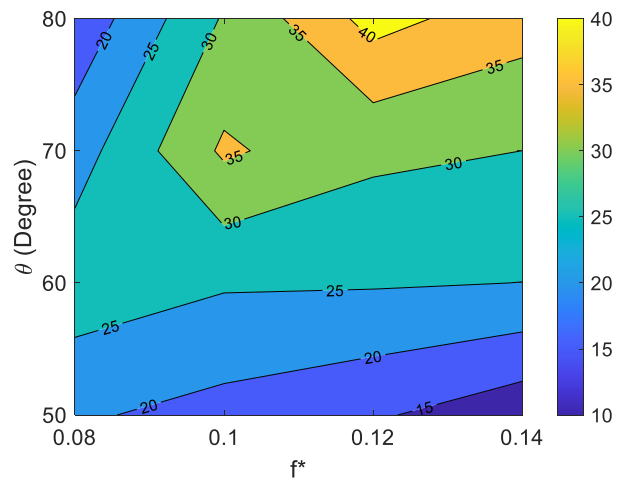
In the symmetric NACA0012 case of **Fig. 71a**, the power efficiency map of first half of a cycle is almost same as that of the second half of the cycle. In the camber 21% case of **Fig. 71b**, the high efficiency zone (40% - 45%) is at $f^*(0.1 - 0.14)$ and $\theta^\circ(60 - 80)$. In the camber 39% of **Fig. 71c**, high efficiency zone (40% - 65%) is at $f^*(0.1 - 0.14)$ and $\theta^\circ(60 - 80)$ and also the highest efficiency over 65% is achieved.

It have been reported in previous studies that the increase of reduced frequency and pitch amplitude lead to the increase of the power efficiency. As expected, from symmetric (camber 0 percent) to positive camber 21% and 39% amplitudes; the peak efficiency increases up to 45%, and 65%, respectively.

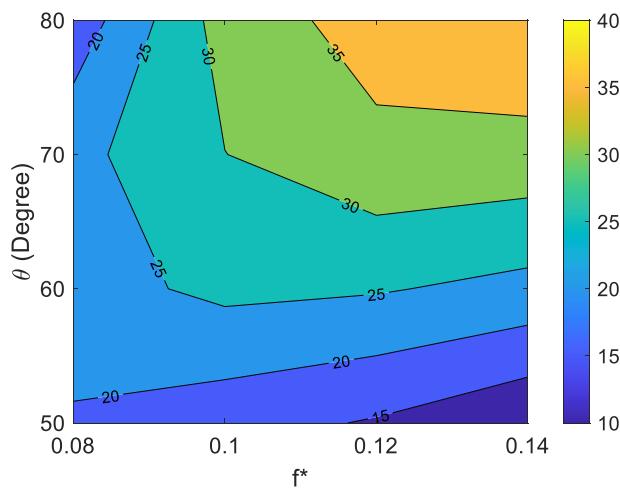
4.3.3 Isocontour map of camber variation for full cycle, $t/T = 0 \sim 1$



a)



b)



c)

Figure 72 Power efficiency maps of camber 0%, camber 21% and camber 39% for full cycle

The efficiency of full cycle is also almost identical to the first half of cycle as well as the second half of cycle as shown in **Fig. 72**. Interestingly, it is observed that the efficiency tends not to increase with an increase of the camber of the hydrofoil in full cycle. Only at high camber 39%, the high efficiency zone over 35% is slightly smaller than those of the zero camber and the camber 21%. In camber 21%, the local maximum is 35. This phenomenon (local maximum) also was reported in previous study [97].

It is known that right swing configuration is not superior to left swing configuration in terms of power efficiency [95]. To complement loss of power efficiency, a camber can play role but fixed shape of the camber shows unbalanced performance in down stroke and upstroke moreover it did not obtain higher power efficiency than the symmetric shape. Thus, a position-adjustable camber mechanism that forms the positive camber in both strokes introduced in section 3.1 is required.

Table 11 Key point in a cycle

Cycle	First half of cycle	Second half of cycle
Stroke	Downstroke (Negative camber)	Upstroke (Positive camber)
C_L and P_y C_D and P_x	Decrease with the camber amplitude increased	Increase along with the camber amplitude increased

4.4 Sub conclusion

In this section, the performance of a right swing turbine with cambered hydrofoil was analyzed by CFD numerical simulations in terms of power efficiency in the ranges of Reynolds number and pitch angle for actual power extraction. It is known that right swing trajectory, which is close to kinematics of flying or swimming creatures, is not superior to left swing trajectory. Cambered shape hydrofoil could be utilized to complement the loss, but it did not show balanced performance in both strokes in a flapping cycle moreover it did not show better

performance than symmetric shape. Consequently, in order to obtain high efficiency of right swing hydrofoil turbine, cambered shape adjustable at positions of a flapping motion, which is an excellent feature of flight and swimming creatures, is mandatory. Eventually, the analysis results of this section will be utilized to develop a high performance flapping hydrofoil turbine.

Chapter 5 Conclusion and further work

5.1 Conclusion

Chapter 2: This dissertation introduced the concept design of a fully passive flapping hydrofoil turbine (FHT) in order to harness the kinetic energy of the water flow. The designed model mimicking turtle could transfer the movement of four single flapping turbines into the rotation of the single main shaft. With fully passive design, timing belts between front and rear hydrofoils served as prescribed pitching for all hydrofoils instead of controlling by servo motors.

Chapter 3: The variable camber hydrofoil was adopted to generate high lift in upstroke as well as down stroke in a flapping cycle. First, the hydrodynamics characteristics (C_L, C_D, C_M) of the introduced airfoil is computed by XFOIL to estimate the flapping response. And then, XFOIL code in Matlab was modified in order to compute the flap moment 1 and flap moment 2 ($C_L, C_D, C_M, Mf_1, Mf_2$).

Throughout the numerical simulations, the results of the concept of variable camber hydrofoil used in flapping tidal turbine for harvesting energy are came out as follows:

1. With the identical counter-loads, the efficiency of the variable camber hydrofoil becomes slightly higher than that of the symmetric hydrofoil due to the lift increase induced by the cambered shape during the upstroke and down stroke, the hydrofoil can create a response with a greater flapping angle amplitude for the same pitch angle than the symmetric hydrofoil. Similarly, compared to the experimental results from the symmetric hydrofoil, a variable camber hydrofoil may create a significantly larger flapping amplitude even for relatively tiny input pitches angles with the Reynolds number 90,000 and 160,000.

2. With the similar amplitudes of the responses by imposing high counter-load for the variable camber hydrofoil, the efficiency of the variable camber one is considerably higher

than that of the symmetric one. Despite the modest increase in complexity, our analysis demonstrates that the variable camber hydrofoil would be a good strategy for enhancing the power performance of an FHT.

Chapter 4: Due to the limitation of the dynamic model code, performance analysis by an in-house computational fluid dynamics code was conducted in viable ranges of Reynold number and pitch angle for actual power extraction. The parametric analysis for a fixed camber hydrofoil obtained following results:

1. According to isocontour map of negative camber in downstroke, the peak efficiency is reduced from symmetric hydrofoil (camber 0%) to the hydrofoils of camber 21% and camber 39% amplitudes.

2. According to isocontour map of positive camber in upstroke, increase of reduced frequency and pitch amplitude leads to the increase of the power efficiency, from symmetric hydrofoil (camber 0%) to the hydrofoils of positive camber 21% and 39% amplitudes; the peak efficiency increases up to 45%, and 65%, respectively.

3. Unfortunately, it is recognized that the efficiency tends not to increase with an increase of the camber of the hydrofoil in full cycle. Consequently, in order to obtain high efficiency of right swing hydrofoil turbine, cambered shape adjustable at positions of a flapping motion, which is an excellent feature of flight and swimming creatures, is mandatory.

5.2 Further work

The concept of energy harvesting device mimicking turtle is novel. Following research could be followed:

- Extension of the dynamic model code to the ranges of Reynolds number and pitch angle range for actual power extraction.
- Extension of CFD code for flapping simulation of variable camber hydrofoil turbine.

- CFD simulation with dual symmetric hydrofoil that could reveal the effect of wake of the front hydrofoil on the rear hydrofoil.

References

- [1] L. Shinn , "Renewable Energy: The Clean Facts," [Online]. Available: <https://www.nrdc.org/stories/renewable-energy-clean-facts>. [Accessed 21 07 2021].
- [2] "Wikipedia: Mandatory renewable energy target," [Online]. Available: https://en.wikipedia.org/wiki/Mandatory_renewable_energy_target. [Accessed 21 07 2021].
- [3] V. Lyatkher, in *Tidal Power Harnessing Energy From Water Currents*, Wiley, 2014, p. ix.
- [4] S. P. Neill and M. R. Hashemi, *Fundamentals of Ocean Renewable Energy*, Elsevier, 2018, pp. 69-70.
- [5] "https://aquaret.com/indexea3d.html?option=com_content&view=article&id=203&Itemid=344&lang=en," [Online]. [Accessed 27 09 2021].
- [6] Q. Xiao and Q. Zhu, "A review on flow energy harvesters based on flapping foils," *Journal of Fluids and Structures*, vol. 46, pp. 174-191, 2014.
- [7] W. McKinney and J. DeLaurier, "Wingmill: An Oscillating-Wing Windmill," *Journal of Energy*, pp. 109-115., 1981.
- [8] K. D. Jones, S. Davids and M. F. Platzer, "Oscillating-wing power generation," in *Joint Fluids Engineering Conference*, San Francisco, 1999.
- [9] C. O. Usoh, "NUMERICAL STUDY OF A FLAPPING FLAT PLATE FOR POWER GENERATION," Ph.D Thesis The University of New South Wales, 2015.
- [10] X. Wu, X. Zhang, X. Tian, X. Li and W. Lu, "A review on fluid dynamics of flapping foils," *Ocean Engineering*, vol. 195, 2020.
- [11] T. Kinsey, G. Dumas, G. Lalande, J. Ruel, A. Mehut, P. Viarouge, J. Lemay and Y. Jean, "Prototype testing of a hydrokinetic turbine based on oscillating hydrofoils," *Renewable Energy*, vol. 36, no. 36, pp. 1710 - 1718, 2011.
- [12] W. Xu, G. Xu, W. Duan, Z. Song and J. Lei, "Experimental and numerical study of a hydrokinetic turbine based on tandem flapping hydrofoils," *Energy*, vol. 174, pp. 375-385, 2019.
- [13] P. E. Sitorus, T. Quang Le and J. H. Ko, "Design, implementation, and power estimation of a lab-scale flapping-type turbine," *Journal of Marine Science and Technology*, vol. 21, p. 115–128, 2016.
- [14] J. Kim, T. Q. Le, J. H. Ko, P. E. Sitorus, . I. H. Tambunan and T. Kang, "Experimental and numerical study of a dual configuration for a flapping tidal current generator," *Bioinspiration & biomimetics*, 2015.
- [15] "www.engb.com," The Engineering Business. [Online]. [Accessed 09 10 2020].

- [16] S. Mandre, "SELF-OPTIMIZING RIVER AND TIDAL POWER CONVERSION DEVICES," 2017.
- [17] M. Boudreau, K. Gunther and G. Dumas, "Investigation of the energy-extraction regime of a novel semi-passive flapping-foil turbine concept with a prescribed heave motion and a passive pitch motion," *Journal of Fluids and Structures*, vol. 84, pp. 368-390, 2019.
- [18] L. Duarte, N. Dellinger, G. Dellinger, A. Ghenaïm and A. Terfous, "Experimental optimisation of the pitching structural parameters of a fully passive flapping foil turbine," *Renewable Energy, Elsevier*, vol. 171, pp. 1436-1444, 2021.
- [19] M. A. Ashraf, J. Young and J. C. S. Lai, "Effect of Airfoil Thickness, Camber and Reynolds Number on Plunging Airfoil Propulsion," in *47th Aerospace Sciences Meeting*, Orlando, Florida, 2009.
- [20] Q. ZHU, "Optimal frequency for flow energy harvesting of a flapping foil," *Journal of Fluid Mechanics*, vol. 675, pp. 495 - 517, 2011.
- [21] M. Ashraf, J. Young and J. Lai, "Oscillation Frequency and Amplitude Effects on Plunging Airfoil Propulsion and Flow Periodicity," *AIAA*, vol. 50, 2012.
- [22] J. Esfahani, E. Barati and H. Karbasian, "Fluid structures of flapping airfoil with elliptical motion trajectory," *Computers & Fluids*, vol. 108, pp. 142-155, 2015.
- [23] J. Wu, Y. L. Qiu, C. Shu and N. Zhao, "Pitching-motion-activated flapping foil near solid walls for power extraction: A numerical investigation," *Physics of Fluids*, vol. 26, 2014.
- [24] R. Godoy-Diana, J.-L. Aider and J. E. Wesfreid, "Transitions in the wake of a flapping foil," *PHYSICAL REVIEW E*, vol. 77.
- [25] K. Jones and M. Platzer, "Numerical computation of flapping-wing propulsion and power extraction," in *35th Aerospace Sciences Meeting and Exhibit*, NV, USA, 1997.
- [26] T. Kinsey and G. Dumas, "Testing and Analysis of an Oscillating Hydrofoils turbine concepts," *Proceedings of ASME*, 2010.
- [27] T. Kinsey and G. Dumas, "Optimal Operating Parameters for an Oscillating Foil Turbine at Reynolds Number 500,000," *AIAA JOURNAL*, 2013.
- [28] R. Zaman, J. Lai, J. Young and M. Ashraf, "Comparison Study of Non Sinusoidal Pitch over Sinusoidal Pitch at Higher Angle of Attack," in *32nd AIAA Applied Aerodynamics Conference*, Atlanta, GA, 2014.
- [29] E. M. Elarbi, "Plunging Frequency-Amplitude Effects on Propulsion Performance of Flapping NACA 0012 Wing," in *51st AIAA Aerospace Sciences Meeting including the New Horizons Forum and Aerospace Exposition*, Dallas, Texas, 2013.
- [30] S. R. Hutchinson, P. Brandner, J. Binns, A. Henderson and G. J. Walker, "Development of a CFD model for an oscillating hydrofoil," in *17th Australasian Fluid Mechanics Conference*, Auckland, New Zealand, 2010.

- [31] J.-C. Veilleux and G. Dumas, "Numerical Simulations of Experimentally Observed High-Amplitudes, Self-Sustained Pitch-Heave Oscillations of a NACA0012 Airfoil," in *21st Annual Conference of the CFD Society of Canada*, Sherbrooke, 2013.
- [32] L. Teng, J. Deng, D. Pan and S. Xueming, "Effects of non-sinusoidal pitching motion on energy extraction performance of a semi-active flapping foil," *Renewable Energy*, vol. 85, pp. 810-818, 2016.
- [33] T. Q. Le, J. H. Ko and D. Byun, "Morphological effect of a scallop shell on a flapping-type tidal stream generator," *Bioinspir. Biomim, IOP Publishing*, vol. 8, 2013.
- [34] T. Q. Le and J. H. Ko, "Effect of hydrofoil flexibility on the power extraction of a flapping tidal generator via two- and three-dimensional flow simulations," *Renewable Energy, Elsevier*, vol. 80, pp. 275-285, 2015.
- [35] P. S H, "Prediction methods of dynamic stability derivatives using the Navier–Stokes equations," PhD Thesis Korea Advanced Institute of Science and Technology, 2003.
- [36] Z. J. Wang and V. Parthasarathy, "A fully automated Chimera methodology for multiple moving body problems," *INTERNATIONAL JOURNAL FOR NUMERICAL METHODS IN FLUIDS*, vol. 33, p. 919–938, 2000.
- [37] G. Houzeaux, B. Eguzkitza, R. Aubry, H. Owen and M. V´azquez, "A Chimera Method for the Incompressible Navier-Stokes Equations," *INTERNATIONAL JOURNAL FOR NUMERICAL METHODS IN FLUIDS*, p. 1–45, 2013.
- [38] T. Q. Truong, P. E. Sitorus, H. C. Park, I. H. Tambunan, H. A. P. J. H. Ko and T. S. Kang, "Nonlinear dynamic model for flapping-type tidal energy harvester," *J Mar Sci Technol*, vol. 19, pp. 406-414, 2014.
- [39] N. L. D. Hai, H. C. Park and J. H. Ko, "Dynamic response estimation for a variable camber NACA0012 hydrofoil of a flapping-type tidal stream turbine," *Journal of Marine Science and Technology*, vol. 26, 2021.
- [40] K. Jones, K. Lindsey and M. Platzer, "An Investigation of the FluidStructure Interaction in an Oscillating-Wing Micro-Hydropower Generator," *Fluid-Structure Interaction II, WIT Press*, vol. 71, pp. 73-82, 2003.
- [41] J. H. Ko and J. Kim, "Experimental Study on Power Improvement of a Flapping Tidal Stream Turbine by Mimicking a Manta-Ray," *Ocean and Polar Research*, vol. 39, p. 293–300, 2017.
- [42] J. Young, S. Morris, R. Schutt and C. Williamson, "Effect of hybrid-heave motions on the propulsive performance of an oscillating airfoil," *Journal of Fluids and Structures*, vol. 89, pp. 203-218, 2019.
- [43] S. Heathcote, Z. Wang and I. Gursul, "Effect of spanwise flexibility on flapping wing propulsion," *Journal of Fluids and Structures*, vol. 24, pp. 183-199, 2008.
- [44] K. PARKER, K. D. ELLENRIEDER and J. SORIA, "Morphology of the forced oscillatory flow past a finite-span wing at low Reynolds number," *Journal of Fluid Mechanics*, vol. 571, pp. 327 - 357, 2007.
- [45] K. Lua, T. Lim and K. Yeo, "Wake-Structure Formation of a Heaving Two-Dimensional Elliptic Airfoil," *AIAA*, vol. 45, 2007.

- [46] J. H. J. Buchholz and A. J. Smits, "On the evolution of the wake structure produced by a low-aspect-ratio pitching panel," *Journal of Fluid Mechanics*, vol. 564, pp. 433-443, 2005.
- [47] S. Srigrarom and C. W. S. Vincent, "Effect of Pitching and Heaving Motions of SD8020 Hydrofoil on Thrust and Efficiency for Swimming Propulsion," in *38th Fluid Dynamics Conference and Exhibit*, 2012.
- [48] C. Usoh, J. Young, J. Lai and M. Ashraf, "Numerical Analysis of a Non-Profiled Plate for Flapping Wing Turbines," in *18th Australasian Fluid Mechanics Conference*, Launceston, Australia, 2012.
- [49] T. Kinsey and G. Dumas, "Parametric Study of an Oscillating Airfoil in a Power-Extraction Regime," *AIAA JOURNAL*, vol. 46, 2008.
- [50] S. Watanabe, S. Terada and A. Konno, "Investigation of Analysis Method of Flow Field Around Flapping Wing By OpenFOAM," in *ISOPE*, 2011.
- [51] A. A. D. Paula, "The airfoil thickness effects on wavy leading edge phenomena at low Reynolds number regime," Ph.D Thesis University of Sao Paulo , 2016.
- [52] "<http://airfoiltools.com/airfoil/index>," [Online]. [Accessed 16 09 2019].
- [53] Y. S. Baik and L. P. Bernal, "Experimental study of pitching and plunging airfoils at low Reynolds numbers," *Experiments in Fluids*, vol. 53, 2012.
- [54] L. Keon, "A feasibility study of oscillating-wing power generators.," M.S. thesis. Department of Aeronautics and Astronautics, Naval Postgraduate, 2002.
- [55] B. Monnier and A. M. Naguib, "Influence of structural flexibility on the wake vortex pattern of airfoils undergoing harmonic pitch oscillation," *Experiments in Fluids*, vol. 56, 2015.
- [56] Z. Liu, J. C. Lai, J. Young and F. B. Tian, "Numerical study on the performance of a flapping foil power generator with a passively flapping flat plate," in *20th Australasian Fluid Mechanics Conference*, Perth, 2016.
- [57] R. Kumar and H. Shin, "Thrust estimation of a flapping foil attached to an elastic plate using multiple regression analysis," *International Journal of Naval Architecture and Ocean Engineering*, vol. 11, no. 2, pp. 828-834, 2019.
- [58] W. Yang, B. Song, W. Song and L. Wang, "The effects of span-wise and chord-wise flexibility on the aerodynamic performance of micro flapping-wing," *Chinese Science Bulletin*, vol. 57, no. 22, pp. 2887-2897, 2012.
- [59] W. Liu, Q. Xiao and F. Cheng, "A bio-inspired study on tidal energy extraction with flexible flapping wings," *BIOINSPIRATION & BIOMIMETICS*, vol. 8, 2013.
- [60] T. QuangLe, J. H. Ko, D. Byun, S. H. Park and H. C. Park, "Effect of Chord Flexure on Aerodynamic Performance of a Flapping Wing," *Journal of Bionic Engineering*, vol. 7, no. 1, pp. 87-94, 2010.
- [61] C. M. Hoke, J. Young and J. Lai, "Effects of time-varying camber deformation on flapping foil propulsion and power extraction," 2015.

- [62] M. Ashraf, J. Young and J. Lai, "Reynolds number, thickness and camber effects on flapping airfoil propulsion," *Journal of Fluids and Structures*, vol. 27, no. 2, pp. 145-160, 2011.
- [63] "Rick Negus Specimen Shells," [Online]. Available: https://www.californiashells.com/tradeshells/exchange_pecten.htm. [Accessed 19 10 2021].
- [64] "Manta Rays in Raja Ampat," [Online]. Available: <https://www.papuaexplorers.com/manta-rays-raja-ampat/>. [Accessed 19 10 2021].
- [65] M. Zhang, X. Liu, D. Chu and S. Guo, "The Principle of Turtle Motion and Bio-mechanism of Its Four Limbs Research," in *2008 IEEE Pacific-Asia Workshop on Computational Intelligence and Industrial Application*, 2008.
- [66] G. Gerosa and M. Aureggi, *Sea Turtle Handling Guidebook for Fishermen Teaching Book*.
- [67] D. E. Alexander, "Nature's Machines: An Introduction to Organismal Biomechanics," *Academic Press*, 2017.
- [68] J. Young and J. C. Lai, "EFFECT OF ANGLE OF ATTACK KINEMATICS ON PASSIVE FLAPPING FOIL POWER GENERATION," in *29th Congress of International Council of the Aeronautical Sciences*, St. Petersburg, 2014.
- [69] A. R. V. Rivera, G. Rivera and R. W. Blob, "Forelimb kinematics during swimming in the pig-nosed turtle, *Carettochelys insculpta*, compared with other turtle taxa: rowing versus flapping, convergence versus intermediacy," *The Journal of Experimental Biology*, vol. 216, pp. 668-680, 2013.
- [70] D. Font, M. Tresanchez, C. Siegentahler, T. Pallejà, M. Teixidó, C. Pradalier and J. Palacin, "Design and Implementation of a Biomimetic Turtle Hydrofoil for an Autonomous Underwater Vehicle," *Sensors*.
- [71] F. E. Fish and J. M. Battle, "Hydrodynamic Design of the Humpback Whale Flipper," *Journal of Morphology*, no. 225, pp. 51-60, 1995.
- [72] D. Chu, X. Liu and M. Zhang, "Research on Turtle Hydrofoil Motion Principle and Bionics," in *International Conference on Automation and Logistics*, 2007.
- [73] N. Nielsen, "What it Means to be Bilaterally Symmetrical," 2016. [Online]. Available: <https://jnnielsen.medium.com/what-it-means-to-be-bilaterally-symmetrical-a601eadaa467>.
- [74] J. D. Anderson, *Fundamentals of Aerodynamics*, New York: 6th edition, McGraw-Hill Education, 2017.
- [75] H. A. Putra, T. Q. Truong, H. C. Park, T. S. Kang and J. H. Ko, "Prediction of Dynamic Response of a Flapping-type Tidal Energy Harvester with a Variable Camber Wing," Montreal, Canada, 2014.
- [76] M. Drela and Y. Harold, "XFOIL 6.94 User Guide," 2001.
- [77] C. Lafountain, K. Cohen and S. Abdallah, "Use of XFOIL in Design of Camber-Controlled Morphing UAVs," *Wiley Periodicals*, 2010.

- [78] T. Ohtake, Y. Nakae and T. Motohashi, "Nonlinearity of the Aerodynamic Characteristics of NACA0012 Aerofoil at Low Reynolds Numbers," *JOURNAL OF THE JAPAN SOCIETY FOR AERONAUTICAL AND SPACE SCIENCES*, vol. 55, no. 644, pp. 439-445, 2007.
- [79] "Javafoil Theory Document".
- [80] "<https://www.mh-aerotoools.de/airfoils/javafoil.htm>," [Online].
- [81] P. E. Sitorus, J.-S. Park and J. H. Ko, "Hydrodynamic characteristics of cambered NACA0012 for flexible wing application of a flapping-type tidal stream energy harvesting," *International Journal of Naval Architecture and Ocean Engineering*, 2018.
- [82] A. J and L. D, "Airfoil designs and free-flight tests of a fixed wing MAV design," in *30th AIAA Applied aerodynamics conference*, New Orleans.
- [83] L. C, C. K and A. S , "Use of XFOIL in design of camber—controlled morphing UAVs," *Comput Appl Eng Educ*, vol. 20, p. 673–680, 2012.
- [84] P. E. Sitorus, T. Q. Truong, H. C. Part and J. H. Ko, "Development of Design and Demonstration of a Flapping-Type Tidal Energy Harvester," in *8th International Conference on Intelligent Unmanned Systems*, 2012.
- [85] P. E. Sitorus, T. Quang Le, J. H. Ko, Q. Tri Truong, I. H. Tambunan, T. Kang and H. C. Park, "Progress on Development of a Lab-scale Flapping Type Tidal Energy Harvesting System in KIOST," in *IEEE Conference on Clean Energy and Technology (CEAT)*, Langkawi, Malaysia, 2013.
- [86] T. Q. Truong, P. E. Sitorus, H. C. Park and . J. H. Ko, "Dynamics model of a flapping-type tidal energy harvester," in *ICIUS*, 2013.
- [87] H. MOL, *Aerodynamics of Wind Turbines*, Routledge, 2015.
- [88] L. Virtuani, "Matlab Central File Exchange," [Online]. Available: <https://www.mathworks.com/matlabcentral/fileexchange/50070-xfoil-for-matlab>. [Accessed July 2021].
- [89] D. Jeong, "A study om Load Reduction of Tidal Turbine Blade," M.S Thesis Jeju National University.
- [90] S. H. Park, "KFLOW User Manual".
- [91] P. E. Sitorus, T. Quang Le, J. H. Ko and T. Q. Truong, "Design, implementation, and power estimation of a lab-scale flapping-type turbine".
- [92] K. W. Cho and J. H. Kwon, "Development of a Fully Systemized Chimera Methodology for Steady/Unsteady Problems," *Journal of Aircraft*, vol. 36, 1999.
- [93] "WIKIPEDIA "PLOT3D file format"," [Online]. Available: https://en.wikipedia.org/wiki/PLOT3D_file_format. [Accessed 09 06 2021].
- [94] S. H. Park, "PreFLOW User Manual".

- [95] P. E. Sitorus and J. H. Ko, "Power extraction performance of three types of flapping hydrofoils at a Reynolds number of $1.7E6$," *Renewable Energy, Elsevier*, vol. 132, pp. 106-118, 2019.
- [96] T. Kinsey and G. Dumas, "Computational Fluid Dynamics Analysis of a Hydrokinetic Turbine Based on Oscillating Hydrofoils," *Journal of Fluids Engineering*, vol. 134, 2012.
- [97] M. P. Deland, M. Olivier, G. Dumas and T. Kinsey, "Oscillating-Foil Turbine Operating at Large Heaving Amplitudes," *AIAA JOURNAL*, vol. 57, 2019.
- [98] H. A. Putra, "Prediction of Dynamic Response of a Flapping-Type Tidal Energy Harvester with a Variable Camber Wing," M. S Thesis in Konkuk University, 2014.
- [99] P. S H and K. J H, "Implementation of $k-\omega$ turbulence models in an implicit multigrid method," *AIAA J*, vol. 42, p. 1348-1357, 2004.